Molecular Diffusion, Adsorption, and Reaction on High Area Oxide Surfaces as Studied by FT-IR

by

Sunhee Kim

BS, Seoul National University, Seoul, Republic of Korea, 1994

MS, Seoul National University, Seoul, Republic of Korea, 1996

Submitted to the Graduate Faculty of

Art and Sciences in partial fulfillment

of the requirements for the degree of

Doctor of Philosophy

University of Pittsburgh

2007

UNIVERSITY OF PITTSBURGH

FACULTY OF ARTS AND SCIENCES

This dissertation was presented

by

Sunhee Kim

It was defended on

August 08, 2007

and approved by

David H. Waldeck, Professor, Department of Chemistry

Sunil Saxena, Professor, Department of Chemistry

J. Karl Johnson, Professor, Department of Chemical Engineering

Dissertation Advisor: John T. Yates, Jr., Professor, Department of Chemistry

Molecular Diffusion, Adsorption, and Reaction on High Area Oxide Surfaces as Studied by FT-IR

Sunhee Kim, PhD

University of Pittsburgh, 2007

Molecular diffusion, adsorption, and reaction on high surface area Al_2O_3 were studied by using transmission infrared spectroscopy and temperature programmed desorption techniques.

It was demonstrated that triethylenediamine (TEDA) binds to Al-OH Brønsted acid sites via hydrogen bonding as well as to Al^{3+} Lewis acid sites on a partially dehydroxylated γ-Al_2O_3 powder at 300 K. The adsorption of a series of CWAs (Chemical Warfare Agents) such as carbon monoxide, hydrogen cyanide, and cyanogen chloride on the TEDA-functionalized Al_2O_3 surface was studied to determine the role of TEDA on the enhancement of the adsorption properties of γ-Al_2O_3 adsorbent by a combination of FTIR and density functional theory studies. No direct binding of the gases to the exposed amine group of a TEDA molecule pre-adsorbed on γ-Al_2O_3 is found. Instead the TEDA molecule effectively competes with the gases for binding sites on the γ-Al_2O_3 surface and only site blocking effects by TEDA are observed.

A new method was developed to study the diffusion properties of molecules into compressed powdered samples using transmission IR spectroscopy. The diffusion of 2-CEES (2-chloroethylethyl sulfide) molecules from a condensed film which formed at lower temperature into the interior of two different particle size Al_2O_3 powders was monitored and compared by using the isolated Al-OH species as spectroscopic sensors of the arrival of diffusing 2-CEES molecules. The diffusion of the 2-CEES molecule into the subnano-Al_2O_3 powder particles is

more rapid than in the multinano-Al_2O_3 particles. A surface diffusion mechanism was used to model the diffusion process giving good agreement with the experimental results.

The infrared spectroscopic technique for surface diffusion studies was applied to monitor the transport of CO to the Pt cores of Pt@CoO yolk-shell nanoparticles by probing the development of characteristic IR modes of the adsorbed CO species on the Pt yolk. It was found that the transport of CO occurs by an activated surface diffusion process through the ~ 5 nm thick shell of CoO, surrounding ~ 2 nm diameter Pt cores. In addition the infrared spectrum of the CO molecule diffusing through the CoO shells is detected by high sensitivity measurements.

Table of Contents

List of Tables

List of Figures

Acknowledgements

First of all, I am very grateful to my advisor Dr. John T Yates, Jr. for giving me an opportunity to work in the Surface Science Center. I would also like to thank him for showing such confidence in me and encouraging me to perform to the best of my ability and supporting me with his endless patience.

I also would also like to thank my committee members, Prof. J. Karl Johnson, Prof. David H. Waldeck, and Prof. Sunil Saxena for kindly agreeing to be on my committee despite their busy schedules and for their guidance and comments.

I also owe a lot of thanks to all the members in our group. I really enjoyed the years working with them. Thanks to Marge Augenstein, our secretary for her assistance and encouragement.

I am especially grateful to Dr. Dan C. Sorescu for his invaluable discussions and critical comments, and for his theoretical calculations which form a part of most of my paper.

I would like to acknowledge the generous support of all people in the Department of Chemistry, in the machine shop, and in the glass shop.

Personally, I would like to thank my family, my parents, my husband, my daughter, Sein for their love and support throughout my life.

I would like to dedicate this dissertation to my husband, Junseok, who has been with me at every moment.

Introduction

I. Triethylenediamine (TEDA) in Industrial Applications

Triethylenediamine (TEDA) (also called 1, 4-diazabicyclo [2.2.2]octane, DABCO) has a symmetrical cage-like structure having two tertiary amine moieties at its two vertices.

Figure i-1. The molecular structure of: (a) triethylenediamine; (b) triethylamine.

Figure i-1 shows the molecular structure of TEDA, compared to a triethylamine molecule which has a tertiary amine group with the same length of aliphatic chains. In spite of similar moieties in the two molecular structures, the melting point of TEDA (~ 431 K) is much higher than of triethylamine (~ 158 K). Moreover, even though the TEDA molecule has a lower basicity (pK_a = ~ 8.7) than triethylamine (pK_a = ~ 10.8), TEDA has been regarded as a better basic catalyst and is more commonly used. The high melting point (~ 431 K) of TEDA, its complexing and catalytic activity are derived from the symmetry and compactness of its structure.[1-4] Because the nitrogen-bonded alkyl groups are tied together in the cage, the TEDA molecule exhibits reduced steric hindrance during coordinating with other molecules via the amine groups. For this reason, TEDA shows outstanding homogeneous catalytic activity among amine molecules which have similar or even higher basicity.[4,5] Practically, TEDA has found extensive use as an amine catalyst in the manufacture of urethane. TEDA promotes the polymerization reaction of isocyanate (R_1-N=C=O) with polyol (HO-R_2-OH). It forms an activated complex with the C=N moiety of the isocyanate group, which makes the reaction by the alcohol oxygen atom in polyol easier.[6,7]

In environmental and military applications triethylenediamine (TEDA) has been used as an impregnant in filtration and air-cleaning systems. Originally, TEDA was added to remove radioactive gases such as methyl iodide (or bromide) by the nuclear power industry in 1967 when activated carbon had been applied as an adsorbent material in the air-cleaning system.[8-11] Traces of CH_3I in air react with TEDA on activated carbon by formation of a quaternary ammonium salt, as shown in Figure i-2. Another way to eliminate radioiodine compounds was isotopic exchange with non-radioactive iodine which is supplied by impregnated KI or KI + I_2. It was reported that the retention of organic iodides by TEDA (or TEDA + KI)-impregnated charcoal is more effective than KI-impregnated materials.

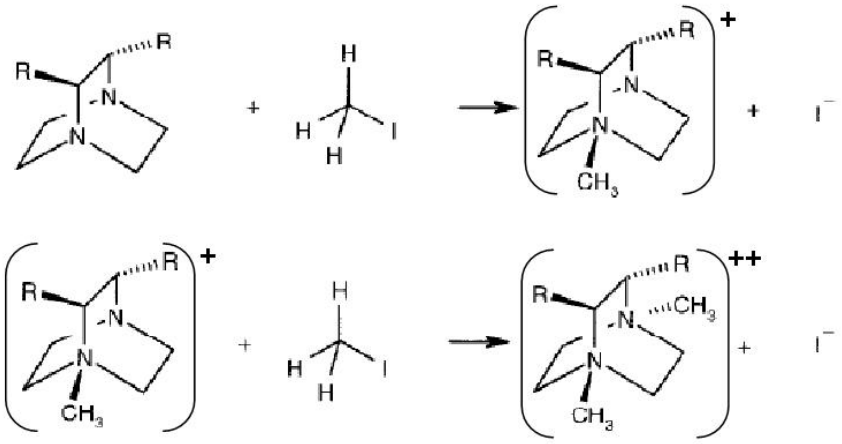

Figure i-2. The reaction mechanism between TEDA and methyl iodide.

However, activated carbon has been used also in military respirator filter systems against nuclear, biological, and chemical (NBC) threats. The main mechanism of activated carbon in filtering is non-selective physical adsorption of vapors on surfaces in its pore structure. But, it is insufficient for the carbon to adsorb volatile, low molecular-weight gases by itself. Therefore, inorganic impregnants such as copper, chromium, silver, zinc, molybdenum, sulfur, manganese, etc. are added to provide additional chemical or catalytic interactions with low boiling toxic

vapors and to promote decomposition of such gases into non-toxic deposits or innocuous gases. In 1943 the development of the first generation NBC filter, called ASC whetlerite carbon, was completed.[12] Copper, silver, and chromium are impregnated in the ASC whetlerite carbon filter to improve the protection against the CWAs (Chemical Warfare Agents) such as phosgene, hydrogen cyanide, arsine, and cyanogen chloride.[13] The ASC whetlerite was the standard filter material until the 1980s when it was determined to be hazardous waste because of the impregnated chromium. There was then an effort to replace chromium maintaining its efficiency at the same level.[12,14]

Meanwhile, after TEDA showed its excellent performance in the removal of radioactive compounds, efforts were made to find an additional capability of TEDA to adsorb other chemical warfare agents as well. It was found that organic amine compounds such as pyridine, picoline, and TEDA are able to reduce the aging effect of carbon filters during use, which is characteristic under humid or high temperature conditions.[15] These amines stabilize inorganic impregnants increasing the shelf life of carbon filters. Because the removal of cyanogen chloride is most severely affected by aging under humid conditions, amine-impregnated materials show a considerably enhanced capacity for cyanogen chloride.[16-18]

The hydrolysis decomposition mechanism of cyanogen chloride on ASC whetlerite is shown below: [19,20]

$$CNCl + H_2O \xrightarrow{Cu(II)/Cr(VI)} HOCN + HCl \qquad (1)$$

$$HOCN + H_2O \xrightarrow{Cu(II)/Cr(VI)} CO_2\uparrow + NH_3\uparrow \qquad (2)$$

Cyanogen chloride undergoes a hydrolysis reaction catalyzed by chromium or/and copper, forming hydrogen chloride and cyanic acid. Cyanic acid is further hydrolyzed to produce carbon dioxide and ammonia.

The chromium-based ASC whetlerite has been replaced since 1993 with ASZM-TEDA whetlerite carbon, which is also a coal-based activated carbon impregnated with copper, zinc, silver, molybdenum compounds, and triethylenediamine.[13] In the chromium-free ASZM-TEDA whetlerite, there is little known about the mechanism of cyanogen chloride removal. It has been reported that zinc possibly takes the place of chromium.[21] But on the other hand, it is also believed that TEDA itself plays its role on the adsorption of cyanogen chloride directly. The reaction mechanism of TEDA with cyanogen chloride is not clear, but it is suggested as being analogous to the reaction with CH_3I, as shown in Figure i-3.[21-23]

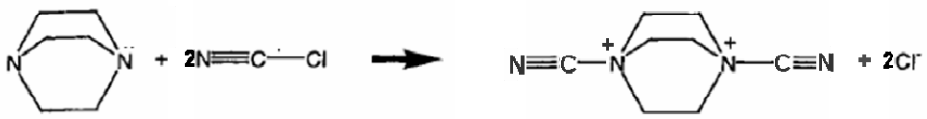

Figure i-3. The proposed reaction between TEDA and cyanogen chloride. [21-23]

Alumina, silica, and zeolites (aluminosilicate) are also commonly used as adsorbents in multi-purpose air filtering systems. The surfaces of these oxide sorbents show some polarity, whereas activated carbon is nonpolar. Metal cations exhibit acidic character, while electron-rich oxygen anions exhibit basic character, which will be described in detail in the next chapter. In the inorganic sorbents, the removal of contaminants is provided by the active sites on the surfaces.

The major objective in PART I and II of the present thesis is to determine the role of TEDA on the enhancement of the adsorption properties of γ-Al_2O_3 adsorbent. Because of the symmetry of the TEDA molecule, the adsorption of TEDA on the γ-Al_2O_3 surfaces would be expected to occur at one end of the molecule with another amine group exposed.

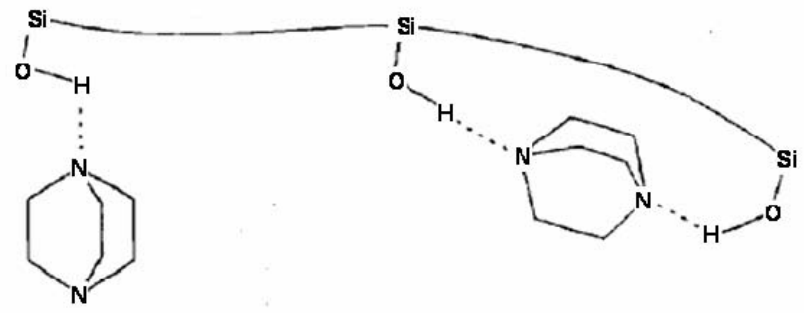

(a) single binding **(b) double binding**

Figure i-4. The two configuration of TEDA Adsorption on a silicate surface forming: (a) single binding; (b) double binding. [24]

It was reported that TEDA adsorbs on a silica surface via one nitrogen atom with the other nitrogen free in the higher coverage region.[24] In addition, two nitrogen atoms may bind with neighboring OH groups on the surface at a lower TEDA coverage, as shown in Figure i-4.[24] Therefore, we have postulated that the two amine groups present on the opposite ends of the TEDA molecule may be able to provide the chemical bonding to the surface as well as bonding sites for subsequently adsorbed species as shown in Figure i-5.

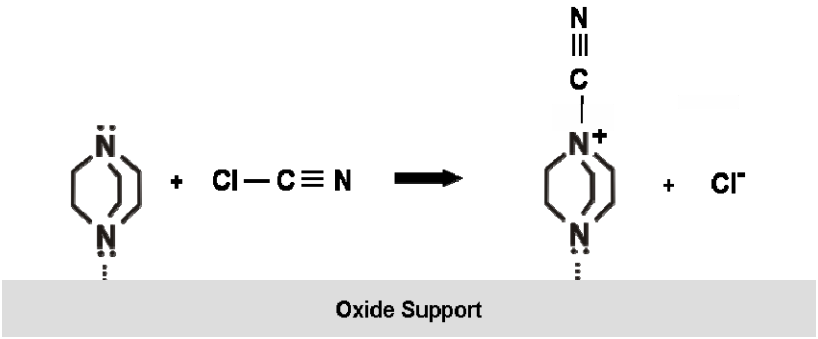

Figure i-5. The proposed mechanism of the reaction between TEDA and cyanogen chloride on oxide surfaces.

In the present work, at first the chemical behavior of TEDA itself on high surface area γ-Al_2O_3 has been investigated in part I. Then the role of the TEDA-functionalized Al_2O_3 surface on the adsorption of a series of blood CWAs such as carbon monoxide, hydrogen cyanide, and cyanogen chloride has been studied in part II. In addition the details of adsorption and dissociation of CO, HCN and ClCN have been investigated on clean γ-Al_2O_3.

II. Surface Properties of γ-Al_2O_3

γ-alumina has been used widely as catalyst, catalytic support, adsorbent, and drying agent in various industrial applications, showing useful properties of high surface area, high pore volume and low pore size.[25-27] Moreover, it can be modified further in various ways to exhibit useful additional applications. Very recently highly-ordered and controlled porous thin films of γ-Al_2O_3 have been used as templates for fabrication of nano-scaled arrays of metals,[28] semiconductors,[29] conducting polymers.[30] Hence γ-Al_2O_3 has been studied for a long time, and there is still a great interest in its fundamental properties.

γ-alumina is obtained from a precursor boehmite (AlO(OH)) by a calcination process. The thermal transformation sequence is given below:[31]

$$\text{Boehmite (AlOOH)} \xrightarrow{500\sim800\ ^\circ C} \mathbf{\gamma\text{-}Al_2O_3} \xrightarrow{800\sim900\ ^\circ C} \mathbf{\delta\text{-}Al_2O_3} \xrightarrow{900\sim1000\ ^\circ C} \mathbf{\theta\text{-}Al_2O_3} \xrightarrow{1100\ ^\circ C} \alpha\text{-}Al_2O_3$$

Transition states

The crystallographic structure of the γ-Al_2O_3 bulk has been considered traditionally as a cubic defect spinel model ($MgAl_2O_4$). Oxygen atoms have a cubic close-packed structure with aluminum atoms in octahedral and tetrahedral interstitial sites. Several empty sites (defect sites) are necessary to satisfy the stoichiometry of γ-Al_2O_3 lattices in a spinel model regime. But recently a more realistic model (a nonspinel model) was proposed which is based on the simulation of the dehydration process of boehmite.[32-34] The main difference between the two models is whether γ-Al_2O_3 contains the defect sites or not in the bulk structure. Though the exact structure remains debatable, the general ideas about the features of γ-Al_2O_3 are as follows: (1). The tetrahedral and octahedral sites take ~ 25 % and ~ 75 % of total Al sites respectively;[35,36] (2). The predominant surface orientations of γ-alumina are the (110) surface (~ 75 %) followed by the (100) surface (~ 15 %) and the (111) surface (~10 %).[37,38] It is known that the detailed morphology of γ-alumina is mainly determined by that of the precursor.[32-34]

As the hydrated precursor is heated up above 1000 K, most of water and hydroxyl groups are removed from the surface. As a consequence of the dehydroxylation process, coordinatively unsaturated aluminum cation sites are created on surfaces, as shown in Figure i-6, which are important to its catalytic properties.[39-42]

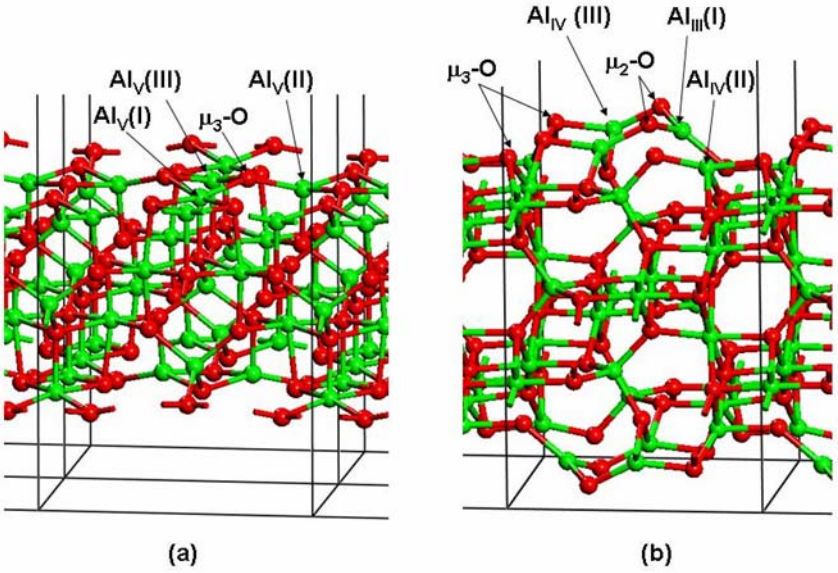

Figure i-6. The pictorial view of the dehydrated γ-Al_2O_3 in a nonspinel model: (a) on (100) surface; (b) on (110) surface.

On (110) surfaces the three-fold coordinated Al_{III} sites (from the tetrahedral coordinated sites with one oxygen atom removed) and the five-fold Al_{IV} atoms (from the octahedral coordinated sites with two oxygen atoms removed) are exposed with two-fold coordinated oxygen atoms (denoted as μ_2-O) and three-fold coordinated oxygen atoms (denoted as μ_3-O). The (100) surface presents five-fold coordinated Al_V sites (from the octahedral coordinated sites with one oxygen atom removed) and three-fold oxygen atoms (μ_3-O).

Upon molecular adsorption on γ-Al_2O_3 surfaces, coordinatively unsaturated Al^{3+} sites act generally as Lewis acid sites, while the oxygen anions act as Lewis base sites.[41,43-45] The electron-deficient metal cations exhibit acidic, electron-acceptor character, while the electron-rich oxygen anions exhibit basic, electron-donor character. On the partially dehydrated surface, the hydroxyl groups (Al-OH) still exist on the surface, and are regarded as Brønsted acid sites. Because of the various sites on the Al_2O_3 surface**,** it displays a complicated behavior upon the

molecular adsorption. Hence the properties of the surface sites are commonly characterized by using probe molecules such as ammonia, pyridine, carbon monoxide and carbon dioxide.

Carbon monoxide is also frequently used to probe Lewis acid sites on the γ-Al_2O_3 surface in infrared spectroscopic investigations. The CO molecule, as a Lewis base, donates electrons from its 5σ molecular orbital to the empty 3p orbital of the Al atom upon complexing with Al^{3+} sites on the surface. Because the 5σ orbital has a slightly antibonding character, the depopulation of the antibonding character strengthens the C–O bond, which results in the blue-shift of CO vibrational stretching frequency.[46,47] Therefore, the acidity of the Al^{3+} sites is determined by the shift of ν(C≡O) frequency in the IR spectrum. It would be expected that CO molecules bound to more unsaturated aluminum sites would show a higher upward frequency shift with higher adsorption energy.[40,47-49] Upon CO exposure on dehydrated γ-Al_2O_3 surfaces several ν(C≡O) bands appear at higher frequency than that of gas phase CO (2143 cm^{-1}). These CO species are assigned to CO adsorbed on Lewis acid sites of different strength. The higher blue-shifted band (> 2200 cm^{-1}), which becomes more evident on the highly dehydrated surface, is attributed to the CO species bonded to Al_{III} sites (coordinatively unsaturated tetrahedral Al^{3+} sites). The sites are regarded as having stronger Lewis acidity with higher adsorption energy. The CO feature at lower wavenumber (~ 2190 cm^{-1}) is assigned to CO bonded to Al_{IV} or Al_V sites (coordinatively unsaturated octahedral Al^{3+} sites) exhibiting less strong Lewis acidity. In addition, CO molecules are also capable of hydrogen bonding to Al-OH groups on the γ-Al_2O_3 surface, and exhibit ν(C≡O) in the range 2150 cm^{-1} to 2160 cm^{-1}.[40,49]

In the part I and II, the CO molecule is used as a marker for Lewis acid and Brønsted acid sites on the γ-Al_2O_3 surface. Adsorption behavior of coadsorbates such as TEDA, triethylenemonoamine (also called 1-azabicyclo[2,2,2]octane, ABCO), trimethylamine, and

ammonia on γ-Al_2O_3 have been studied by competitive adsorption with CO molecules on these active sites.

The adsorption behavior of triethylenediamine (TEDA) on the high area γ-Al_2O_3 surface has been studied. It is demonstrated in part I that TEDA binds to Al-OH Brønsted acid sites via hydrogen bonding as well as to Al^{3+} Lewis acid sites on the Al_2O_3 surface. The effect of TEDA on the capture of chemical agents, such as carbon monoxide, hydrogen cyanide (HCN) and cyanogen chloride (ClCN) on the γ-Al_2O_3 support has been studied, which is shown in part II. Since surface sites are occupied by pre-adsorbed TEDA on the γ-Al_2O_3 surfaces, most of the ν(C≡O) or ν(C≡N) modes formed on clean Al_2O_3 surfaces are absent upon adsorption on the TEDA-functionalized γ-Al_2O_3 surface. No direct chemical interaction between those CWAs and the exposed amine group on TEDA pre-adsorbed on γ-Al_2O_3 is found. Instead the TEDA molecule effectively competes with CWAs for binding sites on the γ-Al_2O_3 surface. In the course of studying the action of the TEDA molecule on the adsorption of HCN and ClCN, it was necessary to investigate the adsorption and decomposition of these two molecules on the clean γ-Al_2O_3 surface and part II also contains our studies of these molecules.

III. Surface Diffusion through Porous Materials

The knowledge of the dynamical properties of molecules in pores is very important and useful in applications of porous adsorbents and catalysts. The diffusivity is determined by the texture properties of porous materials such as the pore volume, pore size distribution and surface area, and the surface chemistry properties as well.[50,51] Molecular transport in the porous solids has been conventionally considered as diffusion through the voids within the pores with a rate which

is modified by the presence of the pore walls.[52-54] There are several mechanisms to describe the diffusion through porous media.

1. **Molecular diffusion (or bulk diffusion)**: The resistance to the flow arises from collisions between diffusing molecules. This mechanism is dominant when the mean free path, which is the average distance traveled between collisions, is small relative to the pore diameter. The diffusion in liquid systems or gas transport in high pressure or in large pores is well described within the molecular diffusion model.
2. **Knudsen diffusion**: In the small pores and at low pressure, the mean free path is large compared with the pore diameter so that collisions with the walls is more frequent than those between gas molecules in this model as shown in Figure i-7.[55] The diffusivity in Kundsen diffusion is defined as;

$$D_k = \frac{4}{3} K_0 \sqrt{\frac{8RT}{\pi M}} \qquad (3)$$

where,

K_0: Knudsen flow parameter (function of geometry of the pore and the gas-surface scattering law), $m^2 g^{1/2} s^{-1} J^{-1/2}$;

M: molar weight of the diffusing molecule, $g\ mol^{-1}$;

R: gas constant, $J\ mol^{-1}\ K^{-1}$;

T: temperature, K.

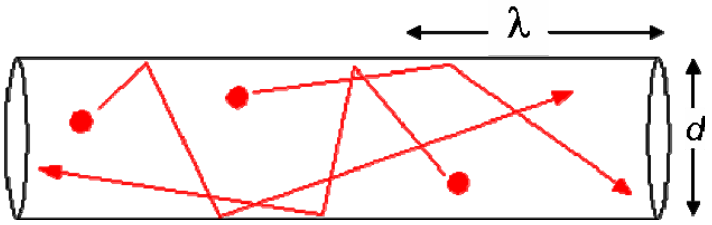

Figure i-7. The schematic picture of Kundsen diffusion. The mean free path (λ) is longer than the pore diameter (d).

3. **Surface diffusion**: The flow of physically adsorbed or chemisorbed molecules along the internal surface of porous solids may be explained by surface diffusion. It is generally accepted that surface diffusion occurs by molecular hopping between adsorption sites, called trapping sites (T-sites), on the surface where the diffusing molecules stay for a brief moment at the energy minima in their potential energy, as shown schematically in Figure i-8.[56] The adsorbed molecule can either desorb with a sufficient energy exceeding the desorption energy or hop to adjacent sites at a rate controlled by the diffusion activation energy. It has been observed experimentally that the energy barrier of diffusion activation energy is generally about 10 – 50 % of the desorption energy for simple molecules on metal surfaces.[57] The temperature dependence of the surface diffusion coefficient, D_s, can be expressed by an equation analogous to the Arrhenius equation as following;

$$D_s = D_0 \exp(\frac{-E_d}{RT}) \qquad (4)$$

E_d: activation energy for surface diffusion, J mol^{-1};

D_0: pre-exponential factor, m^2 s^{-1}.

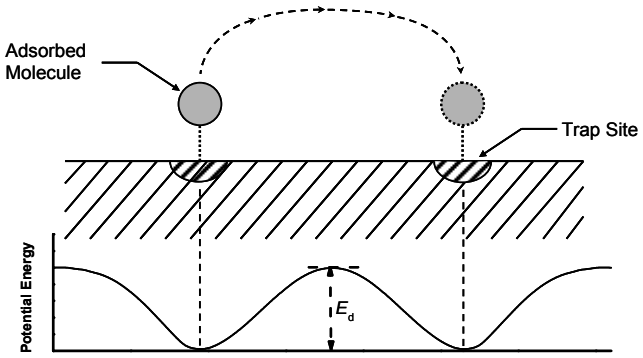

Figure i-8. The schematic illustration for surface diffusion model.

The overall mass transport of gases through the porous structure is the sum of fluxes due to the diffusion processes described above. For many cases of interest, the pores are so small that the bulk diffusion becomes negligible with respect to the other diffusion modes. Surface diffusion and Knudsen flow take place in parallel in such a small pore regions. However, in the systems where adsorbates migrate across high surface area adsorbents such as zeolites, activated carbon, and carbon nanotubes, surface diffusion becomes predominant. It has been observed that the contribution of the surface diffusion to the total mass transport through the porous adsorbents is in a range of 40 ~ 80 %.[58,59] For example, the surface flow of ethylene through activated carbon makes up 70 ~ 80 % of the total mass transport.[60] In the study of CO_2 migration in carbon nanotubes with various diameters (1 ~ 5 nm) it was concluded that diffusion does not occur by the Knudsen mode. These workers also simulate the trajectories of CO_2 molecules in the nanotube, as shown in Figure i-9.[61] Molecules hardly move across the pore, and they are preferentially trapped by sites on the wall.

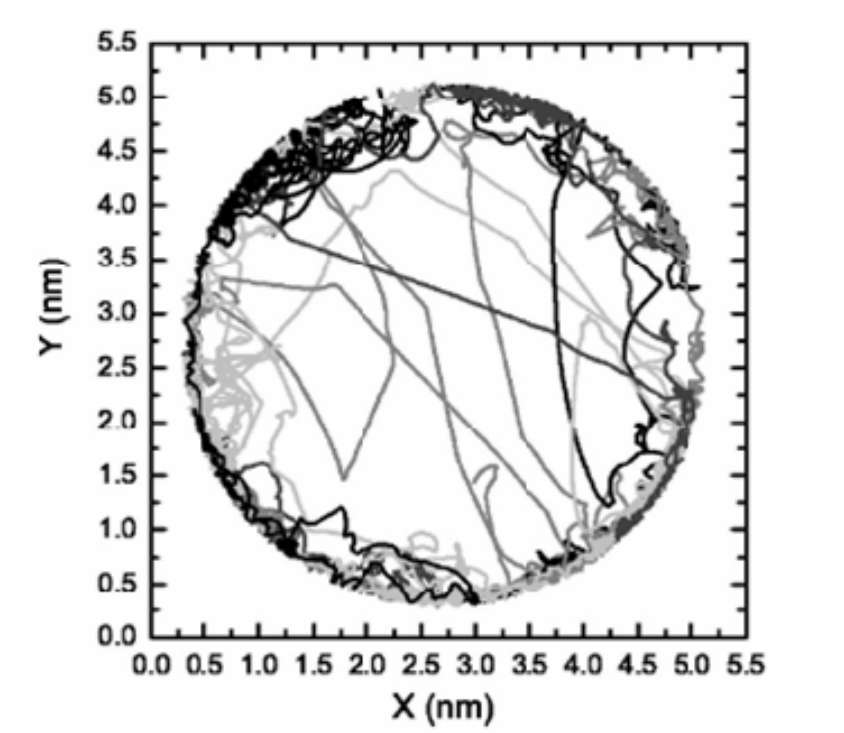

Figure i-9. The simulation of sample trajectories of CO_2 in a (40, 40) single-walled carbon nanotube at 298 K and a pressure of 1 bar. [61]

However, at higher temperature, the adsorbed species tend to desorb from the surface, which results in a decrease in surface flow. The mass flux due to the Knudsen mode is proportional to the square root of temperature as given in equation (3). Hence the contribution of Kundsen flow becomes dominant at higher temperature. But, at 190 K, where the molecules are more easily condensed on surfaces, even for inert nitrogen gas, the surface flow is the dominant diffusion process in micro-scale porous carbon particles.[62]

Chapter VII of the present thesis is about the development of a new method to study the diffusion properties of molecules into powdered γ-Al_2O_3 samples using transmission IR spectroscopy. Partially dehydroxylated γ-Al_2O_3 contains a distribution of isolated hydroxyl groups that are capable of hydrogen bonding to adsorbed molecules. The formation of hydrogen bonds leads to the loss of the characteristic isolated Al-OH vibrational modes and the formation

of associated Al-OH species, which can be investigated by the transmission IR spectroscopy technique. This allows us to monitor the progress of the adsorbate into the interior of compressed powdered γ-Al_2O_3 by using the isolated Al-OH species as spectroscopic sensors of the arrival of diffusing molecules. The kinetic analyses are based on the assumption that the transport of adsorbed molecules through the powdered γ-Al_2O_3, which has a high surface area and nano-scale pores, is governed by the surface diffusion mechanism at low temperature.

IV. Molecular Transport through an Oxide Shell in a Pt@CoO Nanoparicle

There is much interest in controlling shapes, dimensions and components of nano-scaled structures such as nanocrystals, nanorods, nanowires, nanotubes, and so on. Recently a hollow cobalt oxide nanostructure was fabricated through the Kirkendall effect[63] by Yadong Yin *et al*.[64] Cobalt nanocrystals react with oxygen flow to form CoO shells showing multi-crystalline structure as depicted in Figure i-10. Outward transport of metal cations is balanced with inward flow of vacancies, and the supersaturated vacancies condense, resulting a void in each oxide shell.[65] During evolution of the hollow nanoparticle, the transformation of the metallic cobalt to the CoO phase was also proven by X-ray diffraction (XRD), as seen in the XRD panel of Figure i-10. It was observed that all of the metallic cobalt was consumed to form an oxide shell in ~ 3 hours at 455 K.

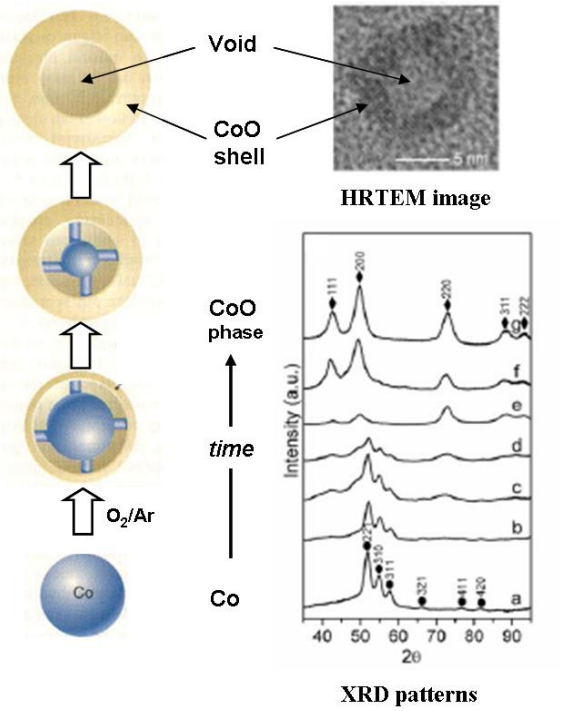

Figure i-10. The schematic diagram of a hollow CoO nanoparticle formation with its HRTEM (High Resolution Transmission Electron Microscopy) image and changes of XRD (X-ray Diffraction) patterns over O_2 flowing time: (a) 0 min.; (b) 2.5 min.; (c) 5.5 min.; (d) 10 min.; (e) 30 min.; (f) 80 min.; (g) 210 min. T = 455 K. Rate O_2/Ar stream = 120 ml/min. [64]

After that, it was possible to synthesize a Pt@CoO yolk-shell nanostructure, where a platinum seed is encapsulated in the hollow oxide shell. In the yolk-shell structure, it would be expected that grain boundaries in the multi-crystalline structure of the oxide shell could provide passageways for small molecules to reach the metal yolk. This implies the possibility for the hollow shell structure to make very useful nano-scale reactors or carriers in many applications. For example, the oxide shell is able to be a good support for catalytic metals. In conventional supported metal catalysts, one of major degradation mechanisms is the sintering effect.[66,67] The effect, because it is generally accelerated at high temperature, is also called the thermal aging effect. At high temperature, the metal particles migrate along the surface of the support followed

by coalescence of the particles, which results in the growth of metal particles, as shown in Figure i-11.[68]

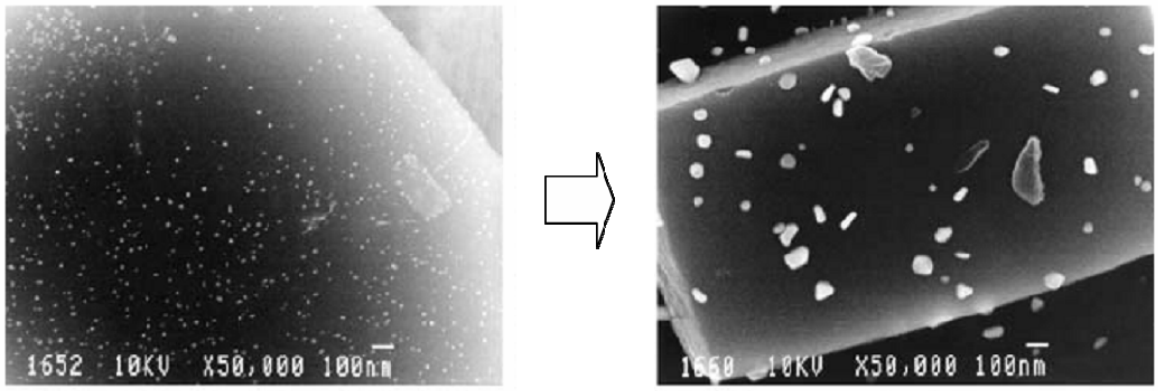

(a) (b)

Figure i-11. STM images of Pt particles supported on zeolite surfaces: (a) before and (b) after aging at 800 K. [68]

Sintering leads to the loss of catalytic activity by reducing the surface area of the catalyst. The core-shell structure, where the catalytic metal is confined inside each oxide carrier shell, would be expected to effectively prevent the particles from aggregating, reducing catalytic surface area.

It was demonstrated that the Pt@CoO yolk-shell exhibits catalytic activity for the ethylene hydrogenation reaction.[64] Since the catalytic activity of platinum is much higher than cobalt or cobalt oxide in this reaction, the reactants and products might diffuse in and out through the CoO shells to reach the platinum core as expected above. The observation of the catalytic reaction is not completely definitive for the diffusion process to the interior of Pt@CoO nanostructures, since traces of surface Pt deposited on the outside of the CoO shell or within pores in the CoO shell could also cause ethylene hydrogenation. Electron microscopy indicated that most of the Pt is encased by the CoO shell, but this measurement is not able to definitively detect atomic-size deposits of Pt deposited elsewhere.

The infrared spectroscopic technique applied to surface diffusion of adsorbates, as described in the previous chapter, has also been applied to monitor the diffusion of CO molecules through the ~ 5 nm thick shell of CoO, observing the arrival of the molecule at the internal Pt surface, as well as detecting the weakly adsorbed CO species present on the CoO surface which feeds CO through the CoO shell. The diffusion length probed in these studies (chapter VIII) is ~ 5 x 10^{-9} m. For the diffusion studies involving γ-Al_2O_3 (chapter VII) the diffusion length probed by essentially the same IR analytic method is ~ 5 x 10^{-5} m. Thus the infrared method devised in this research works over a very wide range of diffusion lengths.

V. Apparatus and Experimental Methods

The system for transmission IR measurements on high surface area solid powders consists of a vacuum IR cell and a FTIR spectrometer. This system which was developed by Basu, Ballinger, and Yates[69] has been proven to be very successful exhibiting following advantages: excellent sample temperature control, high speed of sample temperature change, wide pressure and temperature ranges, low thermal gradients across the sample, small volume of the IR cell, and automated sample positioning.[70] The stainless steel ultrahigh vacuum (UHV) infrared cell and portions of the optic system are shown in Figure i-12.

The cell has two differentially pumped KBr windows for transmission of an IR beam and the cell itself is pumped with a turbo-molecular pump (PFEIFFER Corp., model TMU 071P) to maintain a base pressure $P \leq 1.0 \times 10^{-8}$ Torr after system bakeout at 400 K. A quadrupole mass spectrometer (SRS, model RGA 200) is connected via a high conductance stainless steel tube to the cell for gas phase analysis during temperature programmed desorption.

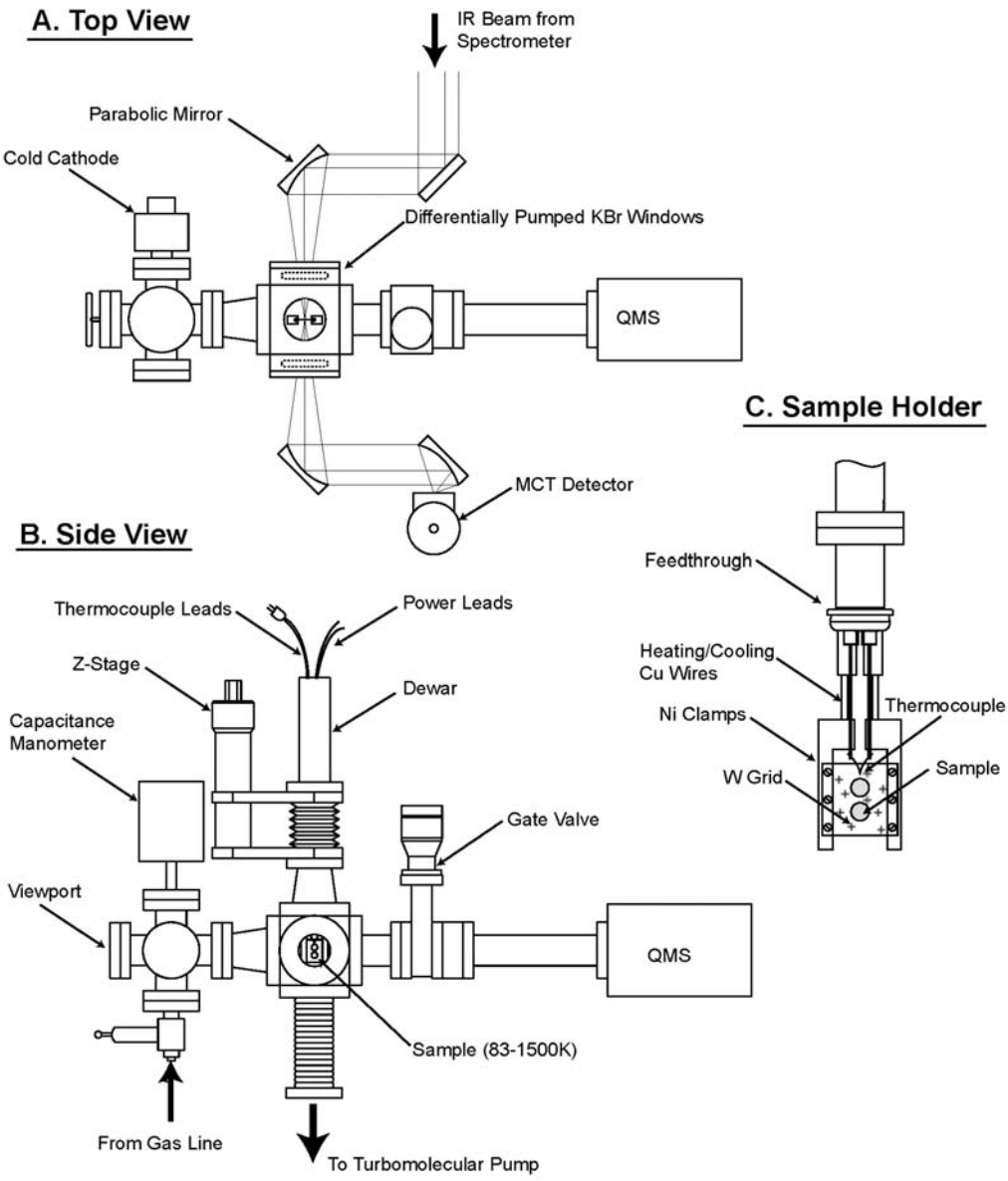

Figure i-12. Schematic diagram of the vacuum system for transmission IR and Temperature Programmed Desorption (TPD) measurement.

A high surface area solid powder is pressed into a tungsten grid (0.002″ thickness) using a hydraulic press.[39,40] The grid is tightly clamped into Ni cooling bars which are bolted onto Cu electrical leads originating from a manipulator's reentrant Dewar. A type-K (alumel-chromel) thermocouple is welded to the top of the tungsten grid. The temperature as measured by the

thermocouple and temperature controller is achieved by resistive heating via the Cu leads using a temperature control program. The sample temperature can be obtained in the range of 83 K – 1500 K when liquid nitrogen used as a refrigerant with a resolution of 0.1 K.

The manipulator which holds the powdered sample on the grid is movable up and down to observe the spectrum of two or more samples supported one above the other together on the grid. This arrangement allows the properties of different powdered samples to be directly compared under exactly the same experimental conditions. Moreover the sample can be azimuthally adjusted by means of the differentially pumped rotatable manipulator. This function greatly facilitates temperature programmed desorption studies as well as direct dosing of compounds of low volatility.

Gases are introduced into the chamber through the gas line. The pressure is measured by a capacitance manometer (MKS Corp., model 627B) in the pressure range of $1 \times 10^{-2} - 1 \times 10^{2}$ Torr. The gas line is evacuated with a turbo-molecular pump between the dosages of different gases.

The infrared spectra are collected with a Bruker TENSOR 27 FT-IR spectrometer by the transmission method. The spectrometer and the optic enclosures are purged continuously with H_2O- and CO_2-free air. The IR detector is a liquid N_2-cooled MCT detector manufactured by Bruker. Each spectrum is obtained by averaging 64 – 512 interferograms at 2 cm^{-1} resolution. The background spectrum taken through the empty grid region is subtracted to eliminate the effect of any gas phase contribution as well as other small effects in the infrared cell.

PART I. FTIR Spectroscopic Study of Triethylenediamine Adsorption on γ-Al_2O_3

I. Vibrational Spectroscopic and Desorption Kinetic Study of Surface Bonding*

I.1 Abstract

The adsorption of triethylenediamine (TEDA) at 300 K is observed to occur via hydrogen bonding to isolated Al-OH groups on the surface of partially dehydroxylated high area γ-Al_2O_3 powder. This form of bonding results in +0.3 − +0.4% blue shifts in the CH_2 scissor modes at 1455 cm^{-1} and a -0.4 % red shift in the CN skeletal mode at 1060 cm^{-1}, compared to the gas phase frequencies. Other modes are red shifted less than 0.1 %. The isolated OH modes are red shifted by -200 − -1000 cm^{-1} due to the strong hydrogen bonding association of Al-OH groups with an N atom in TEDA.

Thermal desorption of adsorbed TEDA from the surface occurs in the range 300 − 700 K. Mass spectral and infrared studies indicate that the decomposition of TEDA occurs on Al_2O_3 above 725 K, and that C-H bonds are broken, forming adsorbed species with N-H bonds which are stable to 1000 K or above. In contrast to adsorption at 300 K, adsorption of TEDA at 85 K results in the formation of a condensed ice of TEDA which covers the outer surface of the porous Al_2O_3, and which does not interact with Al-OH groups inside the porous powder due to immobility.

---

* Reproduced with permission from S. Kim, O. Byl, J. T. Yates, Jr. "Adsorption of Triethylendiamine on Al_2O_3 – I: a Vibrational Spectroscopic and Desorption Kinetic Study of Surface Bonding", Journal of Physical Chemistry B 109, 3499 (2005). Copyright 2005 American Chemical Society.

I.2 Introduction

The adsorption of triethylenediamine (TEDA) [systematic name: 1,4–diazabicyclo[2.2.2]octane (DABCO)] has not been studied using infrared spectroscopy. Because of its highly symmetrical structure, exposing two tertiary amine moieties at its two vertices, adsorption would be expected to occur at one end of the molecule, leaving exposed the other reactive amine group. Surface functionalization by adsorbed TEDA could therefore result in the production of strong electron donor surface properties. It is reported that TEDA is adsorbed on a silica surface via one nitrogen atom with the other nitrogen free at high coverage of TEDA.[24] In addition two nitrogen atoms may bind with neighboring OH groups on silica surfaces. TEDA binds to the nitrile group or to chlorine in methyl chloride via its nitrogen atom. In environmental and military applications TEDA has been impregnated on various supports in order to adsorb toxic gases (HCN, CNCl, SO_2, CH_3I, etc.) or as a sensor to detect these gases.[8,22,71,72] In spite of many applications, there is a dearth of basic information about TEDA adsorption on surfaces. In the present paper the chemical behavior of TEDA adsorbed on high surface area Al_2O_3 is investigated by transmission infrared spectroscopy and temperature programmed desorption techniques.

I.3 Experimental Methods

The stainless steel ultrahigh vacuum (UHV) infrared cell and portions of the vacuum system are shown in Figure I-1. The system was designed to provide temperature control of a porous solid adsorbent from 83 K to above 1400 K. The cell may be rapidly pumped and has provision for gas phase analysis with a quadrupole mass spectrometer (QMS) during temperature programmed desorption (TPD). Compared to a similar previous design,[69] this cell features excellent conductance between the sample and the QMS, and also has higher pumping speed.

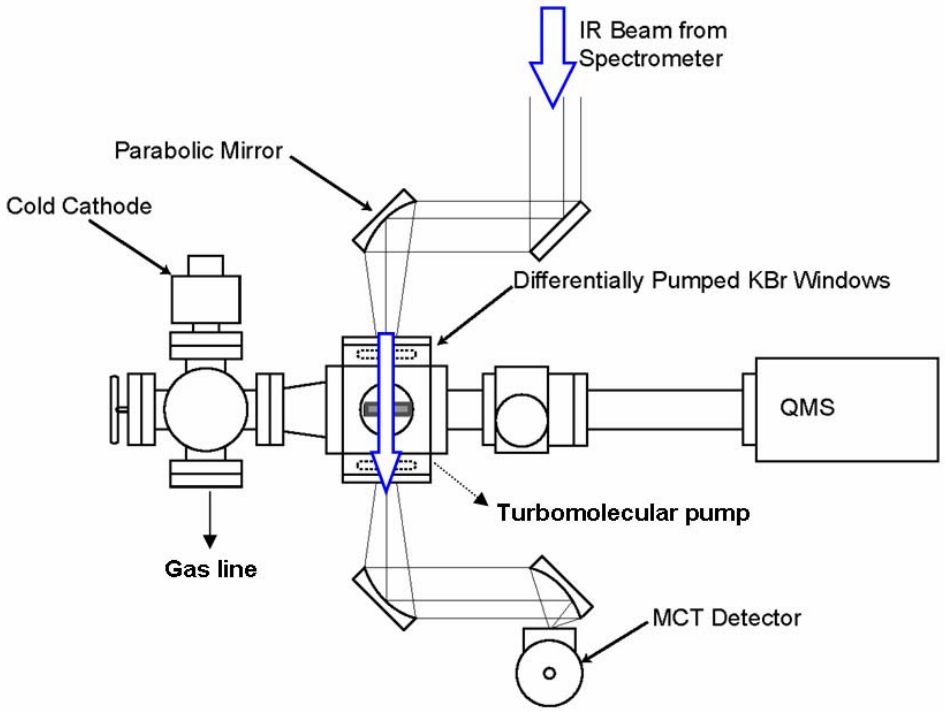

Figure I-1. Top view of the IR vacuum cell and optical settings.

The cell has two differentially pumped KBr windows for the IR beam to pass and the cell itself is pumped with a turbo-molecular pump (PFEIFFER Corp., model TMU 071P) to maintain at a base pressure $P \leq 1.0 \times 10^{-8}$ Torr after system bakeout at 400 K. The QMS (SRS, model RGA 200) is connected to the cell by a high conductance connection. The temperature of the sample can be varied with resistive heating and is controlled and linearly programmed by temperature control software. The lowest temperature obtained with liquid N_2 cooling of the reentrant Dewar is 83 K.

The γ-aluminum oxide powder was obtained from Guild Associates. The N_2 BET surface area is 250 m^2/g. The powder is pressed into a tungsten grid (0.002″ thickness) using a hydraulic press.[39,40] The applied pressure is about 70,000 $lb/inch^2$. A type K thermocouple is welded on the upper edge of the tungsten grid. The grid is tightly clamped into Ni cooling bars which are bolted

onto Cu electrical leads which also conduct heat from the grid + clamps into the reentrant Dewar. The Al_2O_3 is annealed in vacuum at 1200 K for 1 min to produce a highly dehydroxylated surface.[39,41,73,74] The treatment also removes traces of organic contaminants.

The triethylenediamine (TEDA) was obtained from Aldrich (98 % purity) and was used without further purification. TEDA is dosed into the chamber through the gas line by sublimation at room temperature. The vapor pressure of TEDA at 297 K is 0.59 Torr. The pressure of the TEDA is measured by a Bayard-Alpert type ionization gauge (BAG) (Kurt J. Lesker Corp., model IG 2200) in the pressure range of $1.0 \times 10^{-3} - 2.0 \times 10^{-9}$ Torr and by a capacitance manometer (MKS Corp., model 627B) which has range of $1 \times 10^{-2} - 1 \times 10^{2}$ Torr. Care was taken not to use the BAG during actual TEDA dosing experiments in order to avoid decomposition by electron impact or by the hot filament.

The infrared spectra are collected with a Bruker TENSOR 27 FT-IR spectrometer by the transmission method. The spectrometer and the custom cell enclosure are purged continuously with gaseous N_2. The IR detector is a liquid N_2-cooled MCT detector manufactured by Bruker. Each spectrum is obtained by averaging 500 interferograms at 2 cm^{-1} resolution. The background spectra are taken through the empty grid region just before taking each spectrum of the Al_2O_3 sample. Spectral subtraction is used to eliminate the effect of any gas phase contribution as well as other effects in the infrared cell.

TEDA coverages at 300 K are adjusted by controlling the equilibrium pressure of TEDA admitted to the cell. Coverages at 85 K are controlled by the admission of a known number of molecules to the cell. When the Dewar is at 77 K, an unknown fraction of the admitted TEDA condensed on the outer surface of the Dewar.

The mass spectrum of gas phase TEDA was measured at an electron energy of 70 eV. Three prominent mass spectral peaks are characteristic of TEDA at m/e = 112 (parent), m/e = 55, and m/e = 42. A bar graph of the mass spectral cracking pattern is shown in Figure I-2, where corrections for small quantities of residual gases present in the vacuum system have been made.

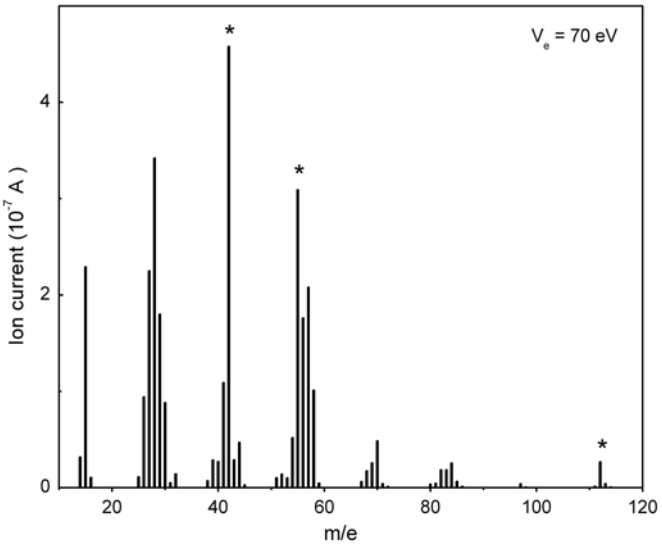

Figure I-2. Mass spectrum of Triethylenediamine (TEDA) gas phase. * = ion fragments used in temperature programmed desorption experiment.

I.4 Experimental Results

I.4.A Transmission IR Studies of TEDA Adsorption on Hydroxylated Al_2O_3

In order to interpret the spectra of adsorbed TEDA, the spectrum of TEDA in the gas phase was measured at 300 K. Figure I-3 shows the infrared spectrum of: (a) gas phase TEDA; (b) condensed TEDA at 85 K on the outer surface of an Al_2O_3 sample; and (c) adsorbed TEDA at 300 K on Al_2O_3. The vibrational modes have been assigned into general categories as shown.

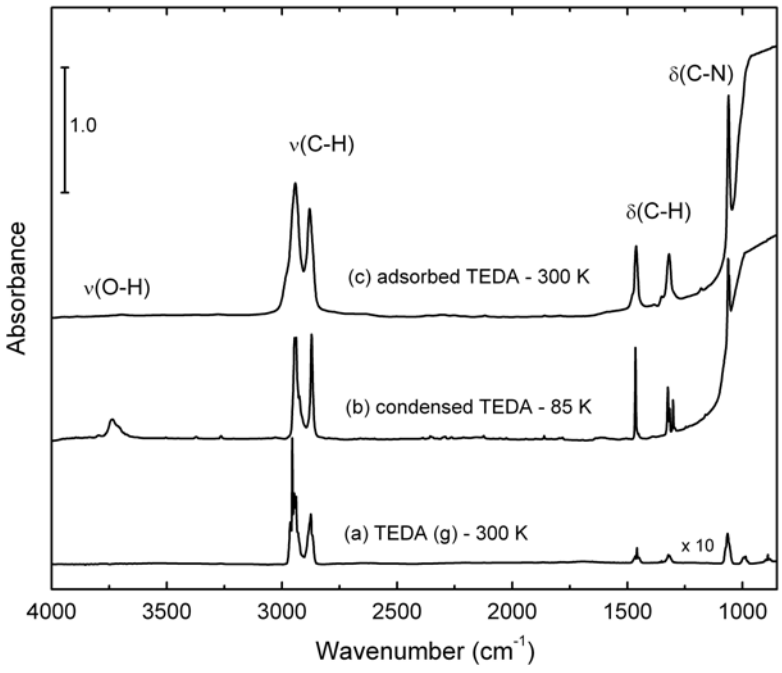

Figure I-3. FT-IR spectra of TEDA: (a) in gas phase at 300 K; (b) in condensed phase on Al_2O_3 at 85 K; (c) in adsorbed phase on Al_2O_3 at 300 K.

The frequency and assignments of the vibrational modes for the gas phase TEDA molecule, and for the adsorbed and condensed phases of TEDA from our studies are given in Table I.[3,75] In subsequent work, we will use the fractional shifts of the infrared frequencies of the adsorbed TEDA (compared to TEDA (g)) as a means of qualitatively understanding the surface bonding. Table II lists the red and blue shifts for the various vibrational modes of adsorbed the TEDA molecules.

Table 1. FT-IR spectral data and vibrational assignment for TEDA

Gas Phase 300 K [260 mTorr] (cm^{-1})	**Adsorbed Phase on Al_2O_3**			**Assignment**
	300 K [260 mTorr] (cm^{-1})	300 K [5 mTorr] (cm^{-1})	85 K [a] (cm^{-1})	
2964 (s)				CH_2 sym.str. [b, c]
2954 (s)	2954	2955		
2946 (s)	2942	2943	2945 (2945)	
2938 (s)			2938 (2937)	
2929 (sh)	2930	2930	2924 (2923)	
2880 (sh)	2880	2882		CH_2 asym.str. [b, c]
2874 (s)	2875		2871(2870)	
2866 (s)	2867	2868		
1465 (m)	1465	1466	1465 (1464)	CH_2 sci. [b c]
1458 (m)	1461	1461		
1450 (w)	1455	1456	1450 (1451)	CH_2 sci. [b, c]
1352 (w)	1352	1351		CH_2 wag. [c]
1323 (m)	1322	1324	1324 (1323)	CH_2 twist .[b]
1317 (m)	1316	1316	1316 (1315)	CH_2 twist. [b]
1295 (w)	1294	1294	1302 (1302)	CH_2 wag. [c]
1072 (s)				
1064 (s)	1060	1060	1062 (1062)	CN skel. [b, c]
1056 (s)			1057 (1052)	
995 (m)				
988 (m)	987		990 (991)	CC skel. [b, c]

[a] Frequency in parentheses is from ref.[3], where IR spectrum is obtained from TEDA polycrystalline film deposited on KBr window at 83 K. [b] This assignment is based on ref. [75]. [c] This assignment is based on ref. [3].

Table 2. Mode shifts of adsorbed TEDA /Al_2O_3 vs. TEDA in gas phase

Frequency [a] (cm^{-1})	Red Shift		Blue Shift		% shift [b]	Mode
	260 mTorr	5 mTorr	260 mTorr	5 mTorr		
2964 (s)						CH_2 sym.str. [c, d]
2954 (s)			-	-	- -	
2946 (s)	-4	-3			-0.14 -0.12	
2938 (s)						
2929 (sh)			-	-	- -	
2880 (sh)			-	+2	- +0.07	CH_2 asym.str. [c, d]
2874 (s)			-		-	
2866 (s)			-	+2	- +0.07	
1465 (m)			-	-	- -	CH_2 sci. [c, d]
1458 (m)			+3	+3	+0.21 +0.21	
1450 (w)			+5	+6	+0.34 +0.41	CH_2 sci. [c, d]
1352 (w)	-	-			- -	CH_2 wag. [d]
1323 (m)	-			-	- -	CH_2 twist. [c]
1317 (m)	-1	-1			-0.08 -0.08	CH_2 twist. [c]
1295 (w)	-1	-1			-0.08 -0.08	CH_2 wag. [d]
1064 (m)	-4	-4			-0.38 -0.38	CN skel. [c, d]
988 (m)	-1				-0.10	CC skel. [c, d]

[a] Frequency of TEDA vibrational mode in gas phase. [b] percentage of the mode shifts vs. frequency in gas phase of TEDA (see 1st column in Table I). [c] This assignment is based on ref. [75]. [d] This assignment is based on ref. [3].

Several general features of the three phases of TEDA may be seen qualitatively from the spectral comparison: (1) The spectral lineshapes for the vibrational modes of the gas phase TEDA differ from that of both condensed and adsorbed TEDA. This is due to vibration - rotation structure in the gas phase spectrum which does not exist for the condensed or adsorbed molecules; (2) The absorption bands are both broad and overlapped in the adsorbed TEDA phase. On the contrary, in the condensed TEDA phase the absorption bands are sharper and some

of the bands present in gas phase are absent. Compared to the previous results,[75] which are given in parentheses in Table I, there is little difference in the observed frequencies of vibrational modes for the condensed TEDA ice film; (3) Even through the modes below 1000 cm^{-1} are not seen for TEDA on Al_2O_3 as a result of the cutoff band due to lattice modes in the Al_2O_3, the informative CN skeletal deformation mode at 1060 cm^{-1} can be accurately observed in the presence of the oxide cutoff band; (4) The isolated Al-OH modes near 3700 cm^{-1} are observed in the condensed TEDA spectrum at 85 K, but disappear for TEDA adsorbed at 300 K. This means that diffusion of TEDA into the internal pore structure of the Al_2O_3 does not occur at 85 K. TEDA is expected to adsorb on Al_2O_3 with hydrogen bonding via the N atom by interaction with isolated Al-OH groups at 300 K.

At sufficiently low temperature TEDA is frozen as an ice on the outer surface of the Al_2O_3. The development of the condensed TEDA layer on the Al_2O_3 surface as a function of increasing dosage at 85 K is shown in Figure I-4. It may be seen that condensation occurs monotonously without any change of the pattern of the vibrational modes of TEDA as dosage increases, and that the isolated Al-OH stretching modes are not influenced at any coverage of condensed TEDA.

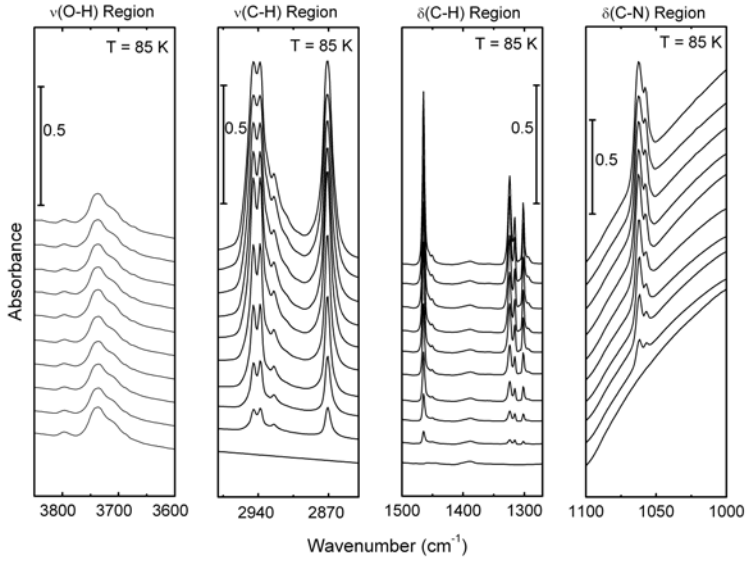

Figure I-4. FT-IR spectra of Al-OH modes and condensed TEDA ice on Al_2O_3 at 85 K with increasing dose of TEDA.

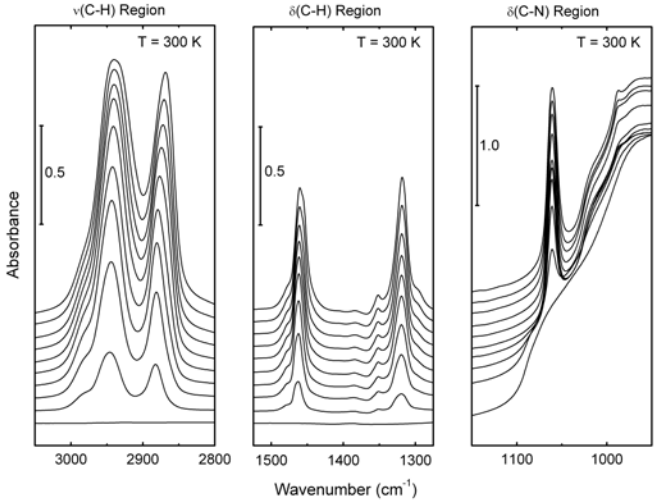

Figure I-5. FT-IR spectra of adsorbed TEDA on Al_2O_3 at 300 K with increasing equilibrium pressure of TEDA. P = 0, 1, 2, 3, 5, 18, 44, 82, 135, 246 mTorr.

In contrast to the experiment at 85 K, Figure I-5 shows the spectral developments for the vibrational modes of TEDA during adsorption at 300 K. Each spectrum is taken when the pressure of TEDA has reached equilibrium at 300 K. As will be shown below, TEDA bonds to

Al-OH groups by hydrogen bonding. TEDA would be also expected to adsorb at Lewis acid (Al^{3+}) sites on Al_2O_3.

The behavior of the isolated Al-OH surface species as a function of the pressure of TEDA in a sequence of adsorption experiments at 300 K is shown in Figure I-6.

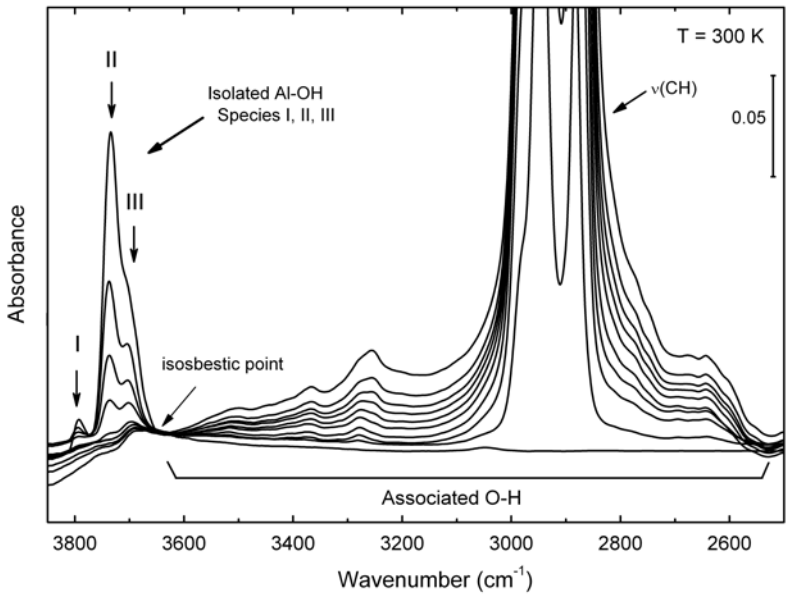

Figure I-6. FT-IR spectra of adsorbed TEDA on Al_2O_3 at 300 K with increasing pressure of TEDA. P = 0, 1, 2, 3, 5, 18, 44, 82, 135, 246 mTorr. An isosbestic point is observed at 3640 cm^{-1}. The ν(CH) modes due to adsorbed TEDA are seen in the 3000 cm^{-1} region.

The isolated Al-OH species exhibit different OH vibrational frequencies in accordance with previous assignments and are due to different degrees of coordination of Al^{3+} ions to O^{2-} ions in the solid.[41] As TEDA is adsorbed, both of the basic (~ 3800 cm^{-1}) and acidic (~ 3740 and ~ 3700 cm^{-1}) isolated Al-OH species are simultaneously converted to associated Al-OH···TEDA modes with red-shifted frequencies spread over a wide frequency range below 3640 cm^{-1}. Superimposed on the broad associated Al-OH bonds is the ν(CH) region due to adsorbed TEDA. An isosbestic point near 3640 cm^{-1} indicates a stoichiometric conversion of isolated Al-OH species to Al-OH···TEDA species. The extreme peak broadness of the band due to associated Al-

OH···TEDA species as well as the enhancement of the integrated absorbance of the associated OH stretching modes is characteristic of hydrogen bonding. In normal cases of hydrogen bonding the integrated absorption due to hydrogen bonding may increase by as much as an order of magnitude.[76] In the case shown here, a factor of ~ 4 increase in integrated absorbance is observed in the wavenumber range shown in Figure I- 6.

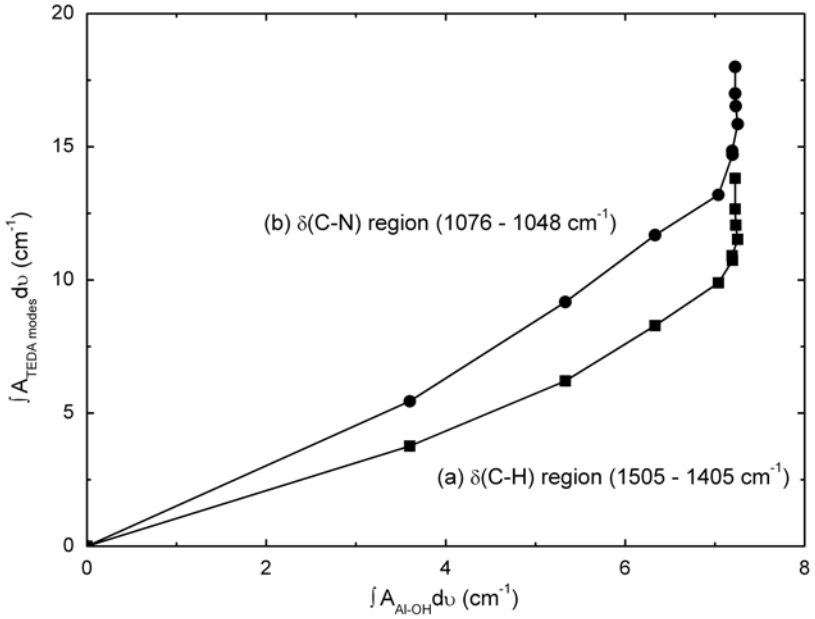

Figure I-7. Relationship between the integrated absorbance of the several TEDA modes and the decreased isolated Al-OH integrated intensity with increasing dose of TEDA at 300 K: (a) in δ(C-H) region (1505 −1405 cm^{-1}); (b) in δ(C-N) region (1076 −1048 cm^{-1}).

Figure I-7 shows the relationship between the integrated absorption of two TEDA modes and the decrease of isolated Al-OH integrated intensity as TEDA is adsorbed to full coverage at 300 K. Figure I-7 clearly shows that a highly non-linear relationship exists between the consumption of isolated Al-OH species as hydrogen bonding occurs and the increase in TEDA coverage as the equilibrium pressure increases at 300 K. In particular, after the isolated Al-OH species have been completely complexed with TEDA, a large increase in TEDA coverage

continues to occur. This means that TEDA adsorbs in two or more stages on the hydroxylated Al_2O_3 surface. It is likely that TEDA adsorption occurs on Al^{3+} Lewis acid sites together with hydrogen bonding to Brønsted Al-OH sites.

The ***specific*** interaction of TEDA molecules with isolated Al-OH sites may be monitored by observing the integrated absorbance of the isolated Al-OH species as a function of the equilibrium pressure of TEDA. This procedure clearly separates the Al-OH bonded TEDA from adsorbed TEDA species at other sites. We assume that the decrease in integrated absorbance of the isolated Al-OH species is proportional to the coverage of Al-OH···TEDA complexes.

The Langmuir adsorption kinetic model can be applied to TEDA adsorption on Al-OH sites as follows:

$$d\theta / dt = k_a \cdot P \cdot (1 - \theta) - k_d \cdot \theta \qquad \text{(I-1)}$$

where θ is the fractional surface coverage of the adsorbate on the Al-OH sites, P is the equilibrium pressure of TEDA and k_a and k_d are the adsorption and desorption rate constants respectively. This equation reduces to the Langmuir adsorption isotherm at equilibrium;

$$P / \theta = P + 1 / K_{eq} \quad (K_{eq} = k_a / k_d) \qquad \text{(I-2)}$$

The isotherm at 300 K is plotted as shown in Figure I-8. The lower equilibrium pressure region below 44 mTorr is mainly characteristic of the first stage of TEDA adsorption on Al_2O_3 at 300 K. The fractional coverage of TEDA hydrogen bonded to Al-OH groups is obtained by subtracting the integrated intensity of the isolated Al-OH modes before and after TEDA dosing at each equilibrium pressure. The insert to Figure I-8 shows the initial part of the adsorption data replotted according to equation (I-2). The linearity of the plot in Figure I-8 shows that complexing Al-OH groups with TEDA is an equilibrium process strictly following Langmurian kinetics, up to ~ 44 mTorr at 300 K.

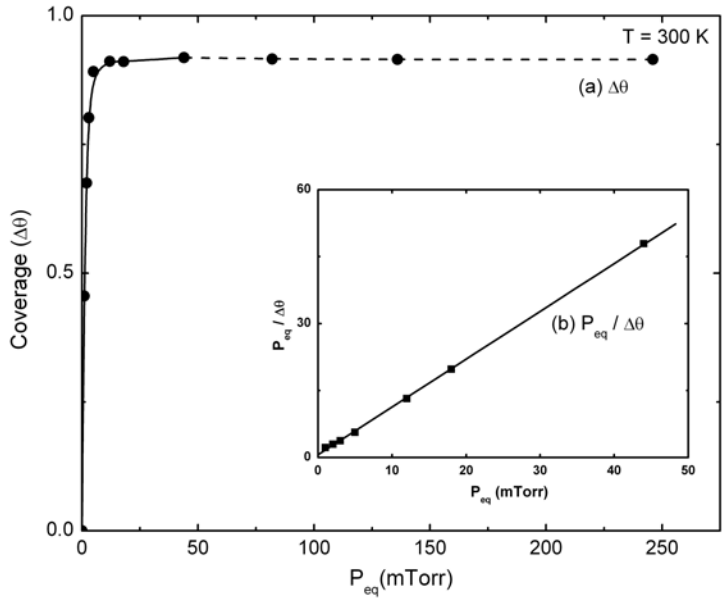

Figure I-8. Langmuir isotherm plot of TEDA adsorption on Al-OH groups at 300 K: (a) Coverage of adsorbed TEDA on Al-OH species (Δθ) vs. equilibrium pressure (P_{eq}). (b) P_{eq} /Δθ vs. P_{eq}, where Δθ is obtained from $-\int A_{OH}\, d\upsilon$ for isolated Al-OH species. The dashed line in the isotherm above 44 mTorr indicates that the fit to Langmuir behavior is not to be expected.

I.4.B Thermal Desorption of TEDA from Hydroxylated Al_2O_3

The temperature programmed desorption spectra from the Al_2O_3 surface following condensation of a thick layer of TEDA at 85 K is shown in Figure I-9. Thermal desorption at m/e = 42, m/e = 55, and m/e = 112 (parent) are recorded. The main desorption feature at 238 K is due to free sublimation of TEDA into the gas phase. A leading edge analysis of the temperature dependence of desorption rate for the condensed TEDA layer was performed. A plot of ln *P* vs. 1/T is shown in the left insert to Figure I-9, monitoring m/e = 42 and m/e = 55. A linear regression analysis yields ΔH_{sub} (TEDA) = 65.4 ± 0.6 kJ/mol as an average of the two measurement. This agrees favorably with ΔH_{sub} for TEDA (61.9 ± 3.3 kJ/mol) which was measured by Wada et al.[77] Thus near 200 K a condensed layer of TEDA sublimes from the outer geometrical surface of the powdered and compressed disk of Al_2O_3.

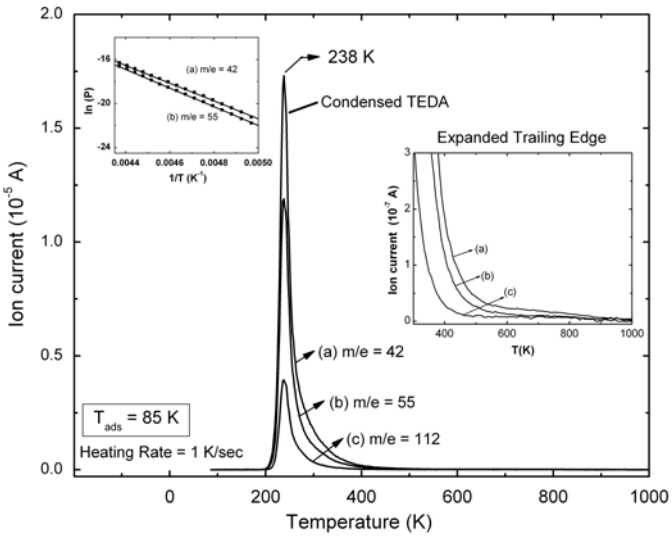

Figure I-9. Temperature programmed desorption of condensed TEDA on Al_2O_3 for: (a) m/e = 42; (b) m/e = 55; (c) m/e = 112. The adsorption temperature was 85 K. The kinetic plot in the left insert yields ΔH_{sub} for condensed TEDA ice on the outer surface of the Al_2O_3. The right insert shows the trailing edge region above 300 K with a magnified vertical scale.

The right hand insert to Figure I-9 showing the trailing edge of the TEDA sublimation process is informative. If substantial amounts of the chemisorbed condensed outer film of TEDA had diffused into the inner pore structure of the compressed Al_2O_3 sample, where stronger chemisorption could occur, then a thermal desorption peak in the 400 − 500 K temperature range would have been observed, as will be shown later (See Figure I-11). The absence of a discernable desorption process in this temperature range indicates that the condensed TEDA layer mainly vaporizes and does not deliver TEDA adsorbate by migration to the powdered Al_2O_3 interior when the heating rate is 1 K/s.

During the temperature programmed desorption experiment when free sublimation of the condensed TEDA is being observed, IR spectra were also taken at every 25 K temperature increment as sublimation takes place, and selected examples of the spectra are shown in Figure I-10. Each spectrum was obtained by averaging only 16 interferograms taking only 7 − 8 seconds.

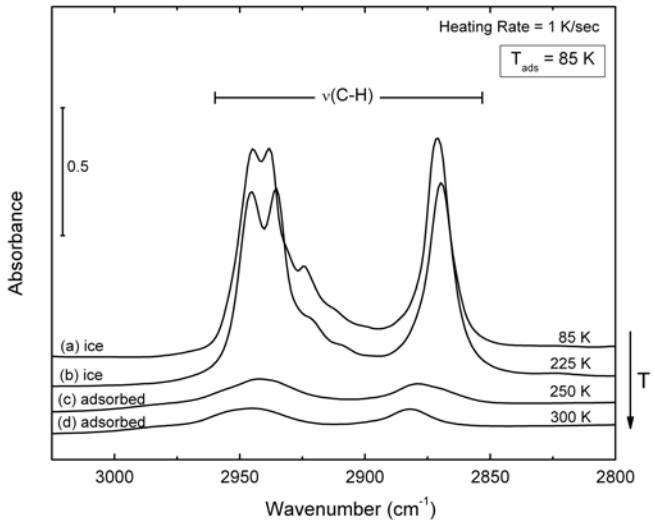

Figure I-10. FT-IR spectra of condensed TEDA on Al_2O_3 during TPD experiment (Heating rate = 1 K/sec). Each spectrum is obtained by averaging 16 scans.

The IR absorbance from condensed TEDA on Al_2O_3 is observed to decrease up to 238 K as sublimation occurs. After that point (238 K) a relatively small amount of adsorbed TEDA is produced on the Al_2O_3. Two broad spectral features in the ν(CH) region are shown. These features in the ν(CH) region are very similar to the spectral feature shown for TEDA adsorbed from gas phase at 300 K in Figure I-5, except their integrated absorbance is below 10 % of the integrated absorbance which can be achieved by adsorption of gaseous TEDA at 300 K. This observation combined with the thermal desorption results (right insert, Figure I-9) indicate that free sublimation of TEDA is the primary process being observed with only a small fractional filling of interior sites in the Al_2O_3 powder.

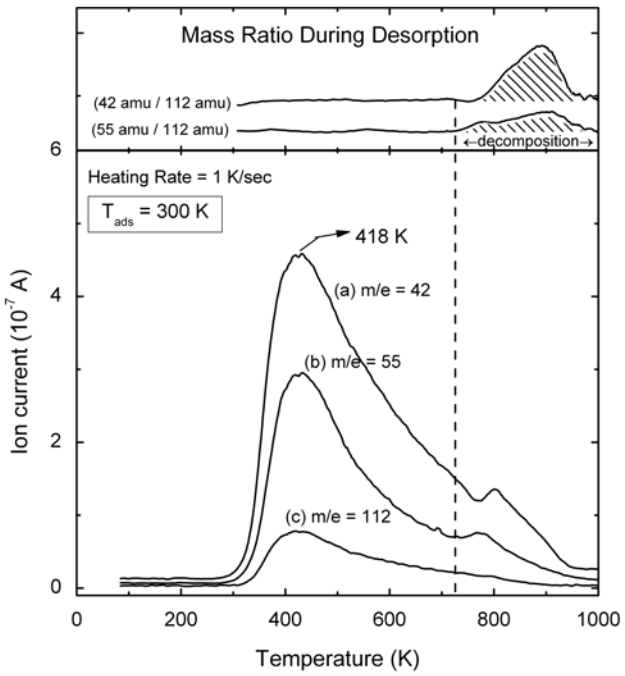

Figure I-11. TPD spectra of adsorbed TEDA on Al_2O_3 for: (a) m/e = 42; (b) m/e = 55; (c) m/e = 112. The adsorption temperature was 300 K. The plots of the mass ratio of m/e = 42 and m/e = 55 to m/e = 112 are shown at top and indicate TEDA decomposition on Al_2O_3 above ~ 725 K.

Figure I-11 shows the TEDA desorption experiment carried out after TEDA adsorption from the gas phase at 300 K. Here, a larger quantity of TEDA desorbs above 300 K than was observed in Figure I-9. This is a result of adsorption at 300 K, where the temperature and time at this temperature favor diffusion of TEDA into the interior of the powder. Up to ~ 725 K, desorption of TEDA occurs without the evolution of observable decomposition products and the mass ratio 42/112 and 55/112 remains almost constant as shown at the top of Figure I-11. However, above 725 K, the three mass spectral features at m/e = 42, 55, and 112 do not behave in the same manner and the 42/112 and 55/112 ratios increase substantially. This suggests that TEDA begins to dissociate on Al_2O_3 at 725 K, yielding other thermal desorption products which also have mass spectrometer cracking products at m/e = 42 and m/e = 55.

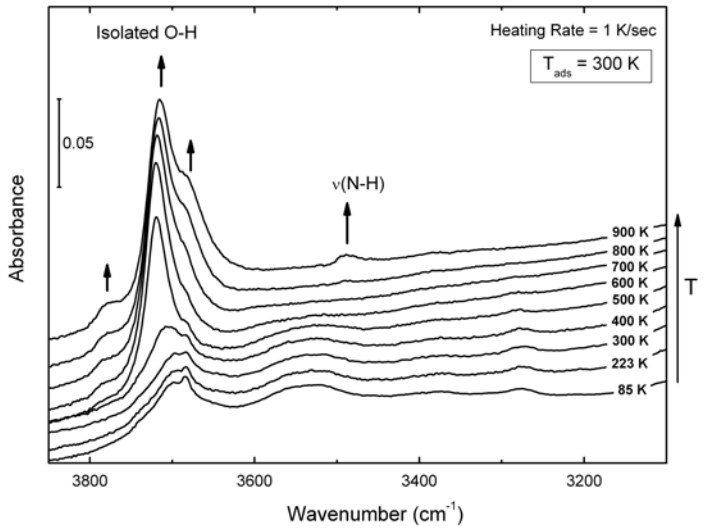

Figure I-12. FT-IR spectra of adsorbed TEDA on Al_2O_3 during the TPD experiment (Heating rate = 1 K/sec). Each spectrum is obtained by averaging 16 scans, and is measured at the temperature shown.

In Figure I-12, studies of the infrared spectrum of the Al_2O_3 containing adsorbed TEDA reveal that a new spectral feature at 3485 cm^{-1} begins to develop near 800 K. This feature is due to an N-H stretching mode which develops as C-H bonds dissociate, likely resulting in self-hydrogenation of N-containing cracking products of TEDA decomposition on the Al_2O_3 surface. This N-H containing surface species is observable to temperatures > 1000 K. It is also seen that the desorption of TEDA is accompanied by the regeneration of isolated Al-OH modes

I.5 Discussion

The major finding from this work is that TEDA binds via hydrogen bonding to isolated Al-OH groups on the surface of γ-alumina. It is observed that -OH groups with various frequencies, corresponding to different acidities, are all able to hydrogen bond to the nitrogen lone pair in the TEDA molecule. A wide range of associated Al-OH···TEDA species, having a wide range of -OH frequencies shifted up to -1000 cm^{-1} or more from the isolated Al-OH mode frequencies, are produced. The observation of an isosbestic point at 3640 cm^{-1} indicates that a

stoichiometric conversion process occurs, i.e. that all types of Al-OH groups are complexed by hydrogen bonding to TEDA. Similar observations of an isosbestic point have been made in IR studies of the physical adsorption of both CO and N_2 on isolated Si-OH groups on SiO_2,[78,79] where hydrogen bonding also occurs at low temperatures. The adsorption of TEDA by hydrogen bonding to Al-OH groups occurs reversibly at 300 K, and accurately follows the Langmuir isotherm.

The electronic and geometrical nature of the Al-OH···TEDA hydrogen bond dictates the ratio of the integrated ν(OH) absorbance of the Al-OH···TEDA species to that of the isolated species. Issues such as the static dipole moment and the polarizability of the complexing species participating in hydrogen bonding are involved.[76] Ultimately the magnitude of $\partial\mu/\partial q$, the dynamic dipole associated with the normal coordinate displacement, dq, determines the intensity of the IR transition. In the case of hydrogen bonding to OH groups for molecules in solution, an enhancement of the ν(OH) integrated absorbance upon hydrogen bonding by a factor of 10 or more is often found.[76] The relatively low intensity ratio observed here (~ 4) may be due to a number of features of the O-H···N interaction in the complex, as mentioned above. An additional effect may be the strong dielectric screening of $\partial\mu/\partial q$ by the Al_2O_3, occasioned by the attraction of the TEDA molecule to the surface, causing the O-H bond to be twisted more parallel to the surface. In this inclined geometry, the dynamic dipole will induce a strong anti-parallel image dynamic dipole in the Al_2O_3, leading to depolarization and reduction of absorbance for the associated Al-OH···TEDA mode.[80] Such image effects would also contribute to a slight decrease of the -OH vibrational frequency. For the Al-OH···TEDA species, large shifts of ν(OH) of many hundreds of wavenumbers are seen (Figure I-6) masking any image effects.

In addition to reversible adsorption of TEDA on isolated Al-OH groups, a second stage of TEDA absorption is detected in this work, as shown in Figure I-7. After complete complexation of TEDA with all available Al-OH groups, significant additional adsorption of TEDA occurs. It is likely that additional TEDA adsorption occurs with Al^{3+} Lewis acid sites, but a clear spectral signature for TEDA adsorption in these sites has not been seen in this work.

The thermal desorption experiments shown here sample TEDA molecules adsorbed in two stages as indicated in Figure I-7. A detailed analysis of the desorption kinetics is not warranted because of the mix of binding types, and also because of the involvement of surface diffusion processes from the interior of the Al_2O_3 to vacuum as desorption occurs from the porous oxide. Interestingly, the chemical decomposition of TEDA on the surface at temperatures of about 725 K and above is observed by both mass spectroscopy and IR spectroscopy. The development of an N-H stretching mode at above 800 K indicates that C-H bond scission has occurred, and that self-hydrogenation processes occur on a surface species containing a N atom. The experiments carried out here were not designed to investigate the thermal decomposition of TEDA on Al_2O_3 in detail.

Finally, the observations of a +0.3 − +0.4% blue shift in the CH_2 scissor mode at 1455 cm^{-1} for adsorbed TEDA, and a -0.4 % red shift in the CN skeletal mode at 1060 cm^{-1}, compared to gas phase frequencies, are indicative of the nature of the surface bonding of TEDA. The direction and magnitude of the shifts of these two modes supply experimental information which may be useful for modeling of the surface bonding of TEDA.

I.6 Summary

The adsorption of triethylenediamine (TEDA) on highly hydroxylated γ-Al_2O_3 has been studied using transmission infrared spectroscopy and thermal desorption methods. The following results have been obtained:

1. TEDA has been found to adsorb on Al-OH groups by hydrogen bond formation, resulting is red shifts to the ν(OH) frequency by up to 1000 cm^{-1} or more. In addition, evidence for a second stage of TEDA adsorption is observed, and this likely involves attachment of the TEDA molecules to Lewis acid Al^{3+} sites.

2. TEDA adsorbs reversibly on the Al-OH sites, accurately obeying the Langmuir isotherm at 300 K. The observation of an isosbestic point in the spectral region between the isolated Al-OH modes and the associated Al-OH modes indicates that a stoichiometric conversion process is being observed.

3. Desorption of TEDA occurs in the range 300 K − 725 K without dissociation of the TEDA molecule on the Al_2O_3. Above 725 K, mass spectrometric and IR evidence indicates TEDA dissociation, and a surface species containing an N-H bond is formed probably as a result of self-hydrogenation resulting from C-H bond scission.

4. Characteristic blue shifts of +0.3 − +0.4 % are observed for the CH_2 scissor mode of TEDA when it is bound to the surface. The C-N skeletal mode exhibits a -0.4 % red shift for the adsorbed molecule.

5. At 85 K, TEDA adsorbs as an ice on the outer geometric surface of the powdered Al_2O_3 sample, and does not penetrate into the powder interior. Free sublimation of this condensed film of TEDA occurs with only minor entry into the pore structure of the Al_2O_3 when

the temperature is programmed upward at 1 K/sec. In contrast, at 300 K, mobility of TEDA throughout the compressed Al_2O_3 powder is observed.

I.7 Acknowledgement

We acknowledge with thanks the support of this work by The Army Research Office, and discussion with Dr. Alex Balboa of Aberdeen Proving Ground and with Dr. Joseph Rossin of Guild Associates.

II. Hydrogen Bonding of Triethylenediamine to Al-OH Groups*

II.1 Abstract

The hydrogen bonding of the triethylenediamine (TEDA) molecule to isolated Al-OH groups on partially dehydroxylated high area γ-Al_2O_3 powder has been studied using transmission IR spectroscopy. It has been found that TEDA adsorbs both singly and as multiple species to single Al-OH groups in clearly separable equilibrium stages of adsorption at 300 K. The reversible adsorption of a single TEDA molecule to Al-OH fits the Langmuir adsorption isotherm well, and the enthalpy of adsorption is found to be -15.6 ± 0.5 kJ mol^{-1} in the range of fractional coverage of 0.5 – 0.6. Red shifts of the Al-OH frequency from ~ -200 cm^{-1} to ~ -1000 cm^{-1} are observed as a result of -OH bonding to the N lone pair in the TEDA molecule.

* Reproduced with permission from S. Kim, O. Byl, J. T. Yates, Jr. "The Adsorption of Triethylenediamine on Al_2O_3-II: Hydrogen Bonding to Al-OH Groups", Journal of Physical Chemistry B 109, 3507 (2005). Copyright 2005 American Chemical Society.

II.2 Introduction

The strong bonding of triethylenediamine to Al-OH groups on high area γ-Al_2O_3 surfaces has been investigated in detail using transmission IR spectroscopy to observe hydrogen bonding to the partially dehydroxylated surface. The mode and strength of surface bonding is of importance because of the use of TEDA to enhance the adsorption properties of various support surfaces used for the adsorption of toxic gases. A previous paper[81] has described certain aspects of the bonding of TEDA to Al_2O_3 and its stability on the surface.

This paper reports the thermodynamic details of hydrogen bonding of TEDA to surface Al-OH groups. Surprisingly, two stages of TEDA adsorption by hydrogen bonding have been discovered, and these bonding modes are thought to involve the adsorption of either a single TEDA molecule or two TEDA molecules to a single Al-OH group. A key feature of the adsorption of molecules by hydrogen bonding to surface -OH groups is the large red shift in vibrational frequency experienced by the -OH group as well as a significant enhancement in its integrated IR intensity.[81]

II.3 Experimental Methods

The experimental methods used in this work are described in detail in reference.[81] Briefly, a transmission IR cell contains a flat tungsten grid into which the Al_2O_3 sample is pressed by a hydraulic press. The grid allows the sample to be heated electrically and cooled by a refrigerant, and the grid transmits about 80 % of the incident IR radiation. The IR cell is connected to a stainless steel vacuum system with a base pressure $< 1 \times 10^{-8}$ Torr. Gas may be dosed quantitatively onto the sample. Al_2O_3 activation is accomplished by heating the sample in vacuum to 1200 K to partially remove hydroxyl groups. A MKS capacitance manometer and a Bayard-Alpert ionization gauge are used to measure pressure, and a quadrupole mass

spectrometer may be used to measure the gas composition. A Bruker TENSOR 27 FT-IR spectrometer operating at 2 cm^{-1} resolution is used to obtain the absorption spectra.

II.4 Experimental Results

II.4.A IR Spectral Studies of TEDA Hydrogen Bonding

The spectral developments which occur in the Al-OH stretching region as TEDA is adsorbed to various coverages at increasing equilibrium partial pressures at 300 K are shown at Figure II-1.

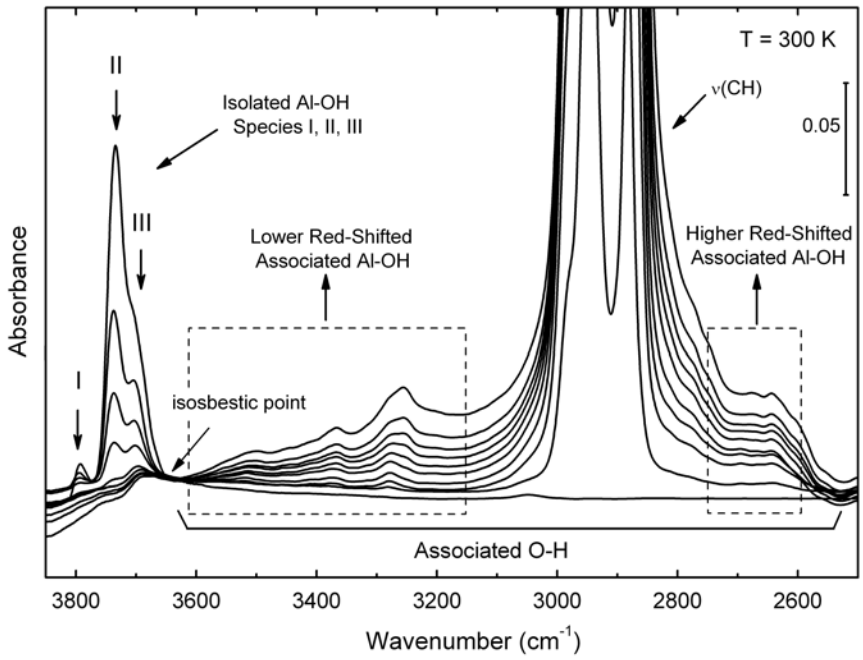

Figure II-1. FT-IR spectra of adsorbed TEDA on Al_2O_3 at 300 K with increasing equilibrium pressure of TEDA. P = 0, 1, 2, 3, 5, 18, 44, 82, 135, 246 mTorr.

It is observed that the absorbance of the isolated Al-OH modes are monotonously attenuated as the TEDA coverage increases, and that a broad band due to hydrogen-bonded Al-OH groups is produced. Superimposed on the broad hydrogen-bonded modes is the absorbance due to ν(CH)

bands for adsorbed TEDA. Two spectral regions due to associated Al-OH species are designated by dotted boxes in Figure II-1.

Three different kinds of isolated Al-OH species are observed prior to TEDA adsorption: (1) a terminal OH group (I) being coordinated to a Al^{3+} cation with ν(OH) ≅ 3800 cm^{-1}; (2) a bridging OH group (II) being coordinated to two neighbor Al^{3+} cations with ν(OH) ≅ 3740 cm^{-1}; and (3) a 3-fold bonded OH group (III) being coordinated to three Al^{3+} cations in octahedral coordination with ν(OH) ≅ 3700 cm^{-1}.[41] The observation of an isosbestic point suggests that a stoichiometric conversion from free -OH to isolated -OH groups is occurring. The shift in -OH frequency due to hydrogen bonding to TEDA occurs down to ~ 2600 cm^{-1}, over an amazingly large frequency range for hydrogen bonding. The three types of Al-OH group exhibit somewhat different kinetics for TEDA adsorption. As TEDA is adsorbed, the efficiency of hydrogen bonding to species (II) (~ 3740 cm^{-1}) is highest as shown in Figure II-2.

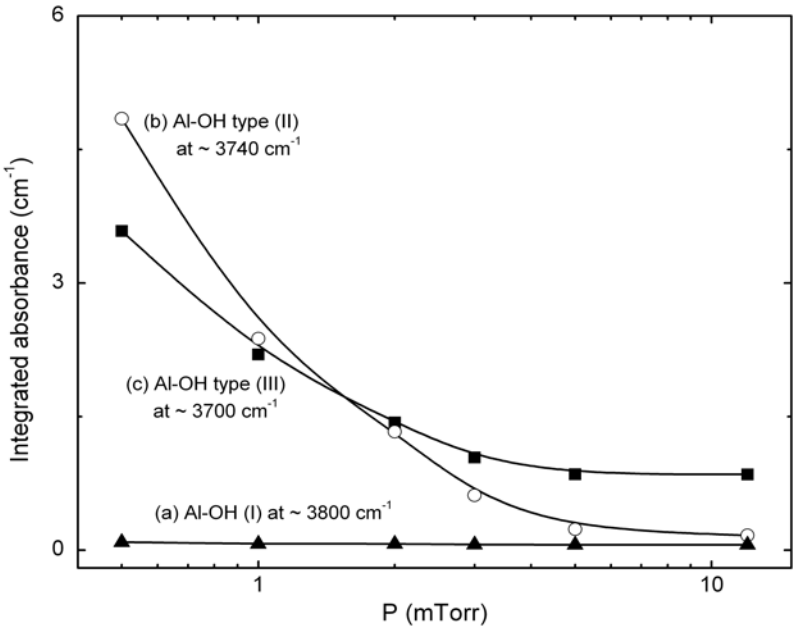

Figure II-2. The decrease in the integrated absorbance of: (a) type (I) Al-OH species observed at ~ 3800 cm^{-1}; (b) type (II) Al-OH species observed at ~ 3740 cm^{-1}; (c) type (III) Al-OH species observed at ~ 3700 cm^{-1}.

Figure II-3 shows a plot of the integrated absorbance of the isolated Al-OH modes compared to the integrated absorbance of the hydrogen-bonded Al-OH modes. The integrated absorbance of the hydrogen-bonded Al-OH modes is obtained in the 3640 − 2500 cm^{-1} region assuming a smooth contribution under the ν(CH) bands due to TEDA adsorption. At an equilibrium pressure of about 10 mTorr at 300 K, the isolated Al-OH species have been completely complexed by TEDA adsorption, and the integrated intensity of the associated Al-OH modes has reached a plateau in absorbance. This region of adsorption is designated Stage A, and is associated with the bonding of a single TEDA molecule to an isolated Al-OH group. Even after all the isolated -OH groups disappear in Stage A adsorption, the integrated intensity of associated Al-OH bands continues to increase during Stage B adsorption. At equilibrium pressures of TEDA above about 10 mTorr, Stage B of TEDA bonding is observed. Here, the integrated intensity of the associated Al-OH groups rises by more than a factor of 2 above its intermediate plateau value as a second TEDA molecule is adsorbed onto the Al-OH group. The two stages of TEDA adsorption may also be correlated with the increase of TEDA coverage.

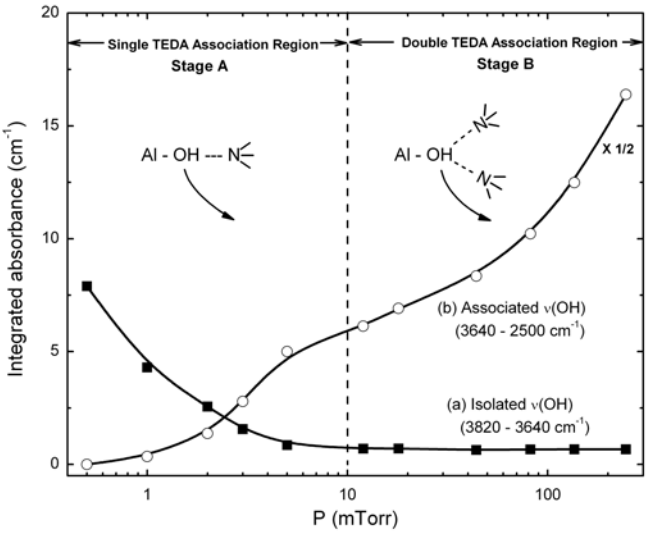

Figure II-3. Relationship between: (a) the decrease of the isolated Al-OH integrated absorbance in the 3820 − 3640 cm^{-1} region; and (b) the integrated absorbance of the associated Al-OH species in the 3640 − 2500 cm^{-1} region with increasing coverage of TEDA at 300 K.

Figure II-4 shows the integrated absorbance for two vibrational bands associated with the TEDA molecule as the equilibrium TEDA coverage is increased at 300 K. For both of the δ-CN skeletal deformation mode and the δ-CH deformation modes (1505 − 1405 cm^{-1}), two stages of adsorption are also observed. Stage A occurs below 10 mTorr; Stage B occurs above 10 mTorr, and both stages are designated by the cross-hatched regions on each isotherm in Figure II-4. These integrated absorbance measurements indicate that approximately ~ 30 % of the adsorption up to 250 mTorr occurs in stage B, after all Al-OH groups have been converted in Stage A adsorption to associated Al-OH groups by the adsorption of a single TEDA molecule.

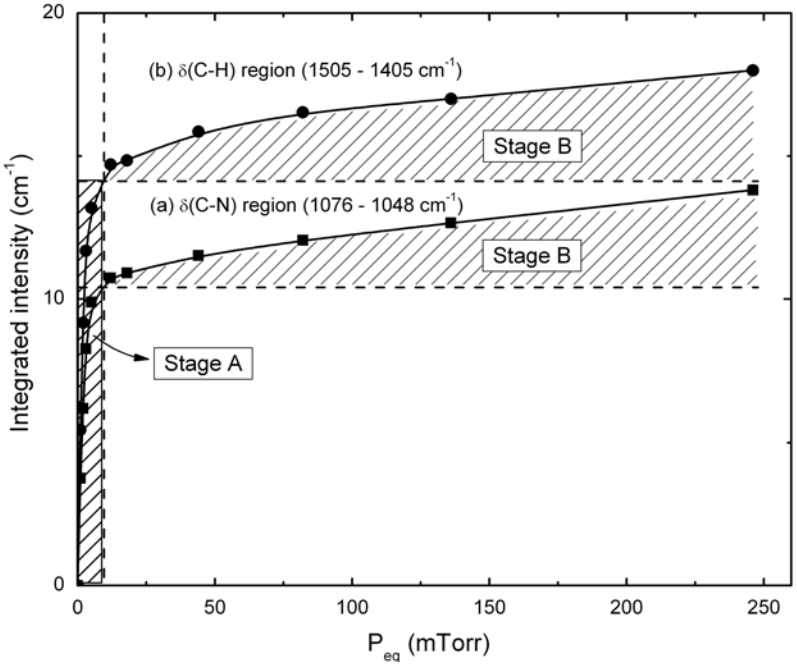

Figure II-4. Plots of the integrated absorbance of the several TEDA modes with increasing coverage of TEDA at 300 K: (a) δ(C-N) region (1076 − 1048 cm^{-1}); (b) δ(C-H) region (1505 − 1405 cm^{-1}).

The relative rate of TEDA adsorption by hydrogen bonding to the three types of Al-OH groups (I, II, and III) differs, as shown in Figure II-2. Also, the reactive rate of producing of hydrogen-bonded Al-OH···TEDA species varies as the TEDA coverage is increased. Figure II-5

shows the integrated -OH absorbance behavior of the two categories of associated Al-OH···TEDA species. We focus only on Stage B TEDA adsorption, where a second TEDA molecue is postulated to adsorb on an Al-OH group already containing a single TEDA molecule. It may be seen that Stage B of adsorption is more associated with the production of hydrogen-bonded Al-OH groups with lower red shifts. In Stage A of TEDA adsorption the higher red shifted Al-OH···TEDA species seem to be favored compared to the lower red-shifted species.

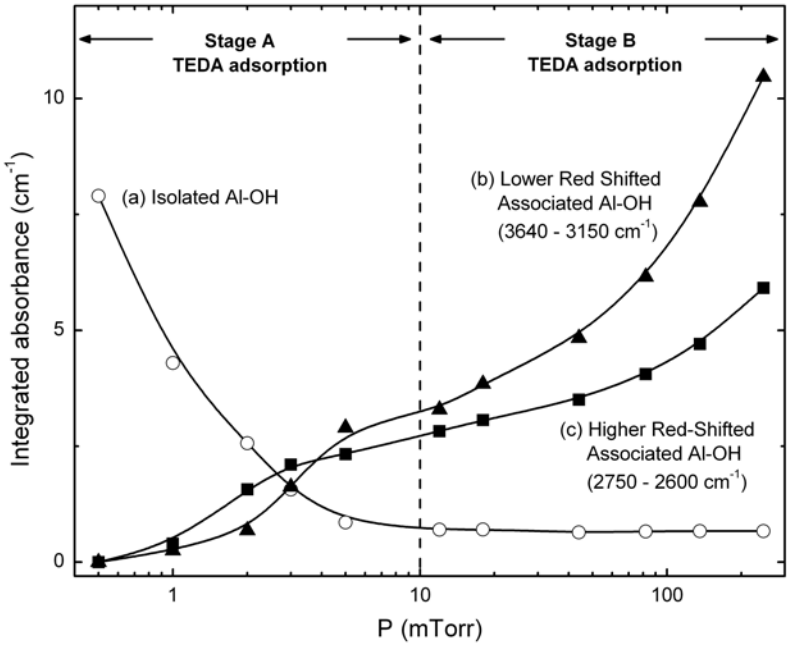

Figure II-5. The relationship between loss of (a) the isolated Al-OH species and (b) the gain of associated OH species in the lower red-shifted associated region (3640 − 3150 cm^{-1}) and (c) in the higher red-shifted associated region (2750 − 2600 cm^{-1}).

II.4.B Detailed Isotherm Studies

In the previous paper, TEDA adsorption on Al-OH sites at 300 K was fitted to the Langmuir adsorption kinetic model.[81] Figure II-6 shows the isotherms for TEDA absorption on Al-OH groups as a function of equilibrium pressure at various temperatures. These isotherms were measured in a special way in order to investigate bonding of TEDA ***specifically*** to the Al-

OH groups. We assume that the decrease in integrated absorbance of the isolated Al-OH groups is linearly dependent on the coverage on the single Al-OH···TEDA complex. Other measures of TEDA coverage might not be so specific to the Al-OH···TEDA species coverage.

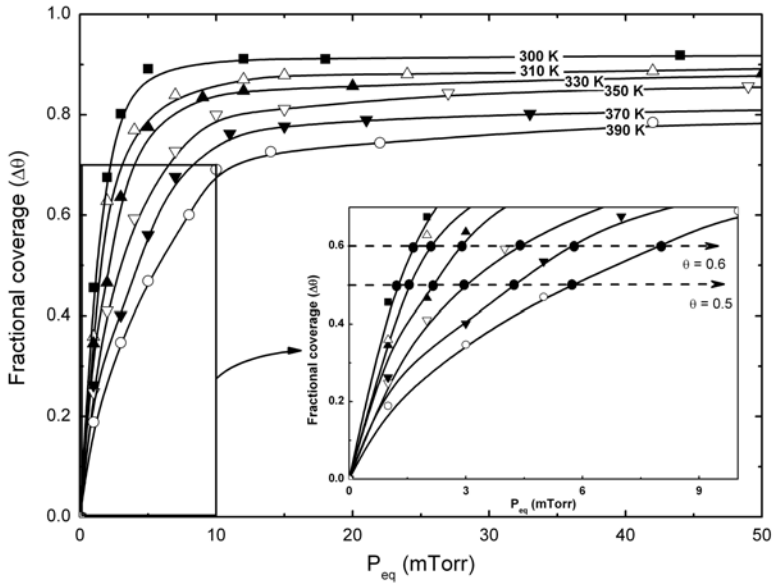

Figure II-6. Isotherm plots of TEDA adsorption on Al-OH groups at various temperatures. The insert shows a magnified view in the region below 10 mTorr (Stage A) and the cuts at θ = 0.5, and 0.6.

Figure II-6 shows, as would be expected, that the saturation equilibrium coverage of TEDA decreases monotonically as the temperature increases. The insert shows a magnified view of the isotherm behavior in the region below 10 mTorr (Stage A adsorption) where only a single TEDA molecule bonds to a single Al-OH group. Cuts across this isotherm at relative coverages of θ = 0.5 and θ = 0.6 are shown, and these cuts will be used to construct a van't Hoff plot to determine the enthalpy of adsorption, as will be shown later. Rather than fitting to the Langmuir model, the isotherm curves are spline fits to the equilibrium data. For the simple Langmuir equilibrium relationship, linear fits by plotting P_{eq} / θ vs. P_{eq} should be obtained. In the initial region (up to ~ 10 mTorr) of the isotherm, the plots of P_{eq} / θ as a function of P_{eq} with a linear fit

at each temperature are shown in Figure II-7. We believe that the data support the operation of a Langmuir equilibrium during Stage A adsorption within the limits of accuracy of the measurements.

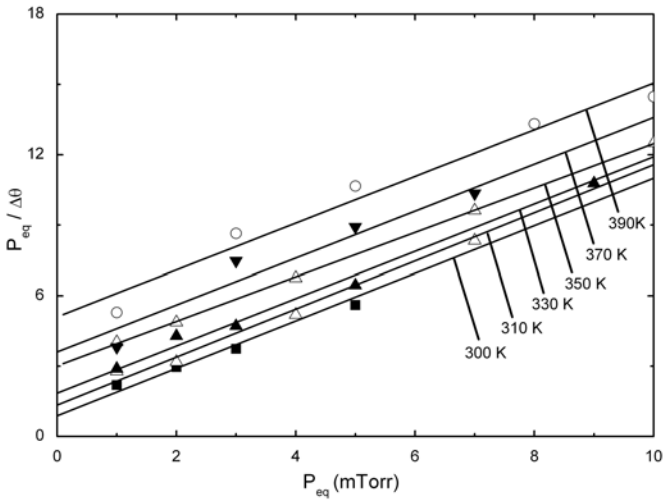

Figure II-7. Linear fitting of P_{eq} /Δθ vs. Peq in the Langmuir fit to isotherms shown Figure II-6 in the region below 10 mTorr (Stage A), corresponding to single TEDA molecule adsorption on Al-OH groups.

Figure II-8 shows the van't Hoff plot for the equilibrium between an Al-OH group and a single TEDA molecule in Stage A adsorption. The data are shown for two relative coverages, as indicated in Figure II-6. It may be seen that to within the experimental error, the values of ΔH_{ad} are equal at the two coverages, and the average value of ΔH_{ad} = -15.6 ± 0.5 kJ mol^{-1}. The data used in Figure II-8 are for equilibrium pressures of TEDA below 7.5 mTorr, clearly in the Stage A region of adsorption.

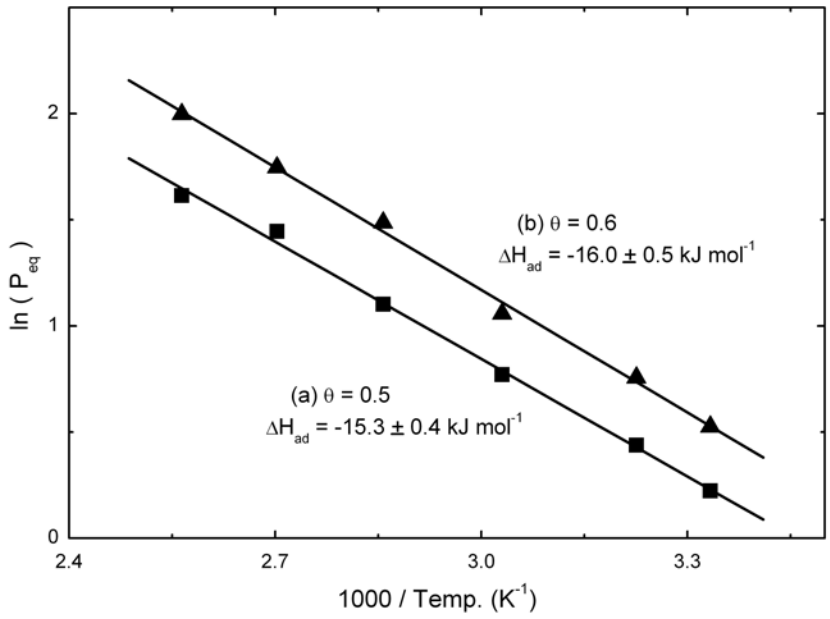

Figure II-8. Van't Hoff plots for the equilibrium between Al-OH species and TEDA molecules at: (a) θ = 0.5; and (b) θ = 0.6.

II.5 Discussion

II.5.A The Surface Hydrogen Bond of TEDA to Isolated Al-OH Groups

The complexation of a donor molecule to Al-OH groups occurs by hydrogen bonding which is primarily an ionic form of bonding.[76] Many factors influence both the red shift in frequency as well as the increase in integrated absorbance of hydroxyl groups which experience hydrogen bonding,[76] including the polarizability of the adsorbate,[41] and the ionization potential of the adsorbate.[82] The spectroscopic development of Al-OH groups associated with the TEDA molecule results in a large range of -OH stretching frequencies from about 3600 cm^{-1} to about 2600 cm^{-1}, suggesting that Al-OH groups with different degrees of coordination to the Al_2O_3 substrate experience large differences in their modification by hydrogen bonding.[41] A slightly higher efficiency of hydrogen bonding of TEDA to OH species II (~3740 cm^{-1}) having less positive net charge than species III (~3700 cm^{-1}) at OH is observed, as shown in Figure II-2.

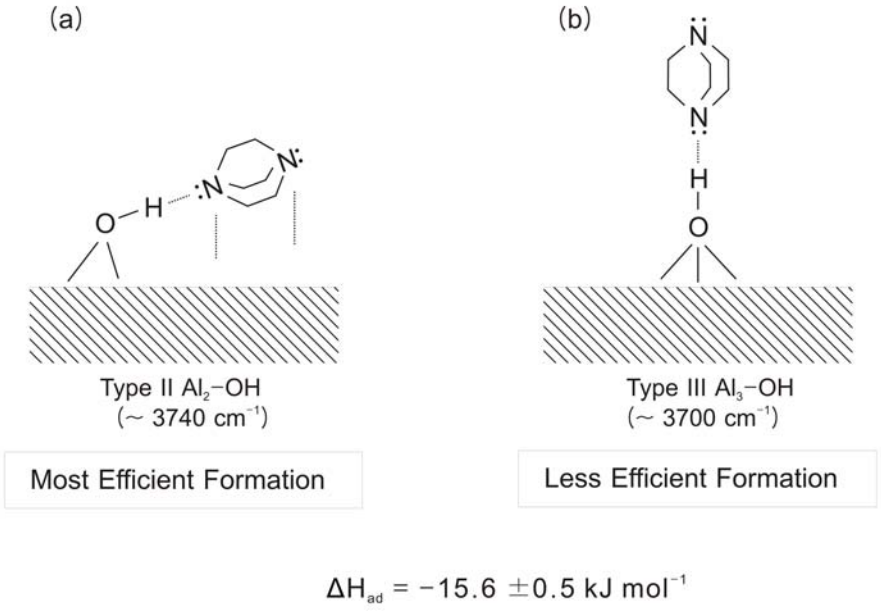

Figure II-9. Schematic picture of TEDA adsorption on: (a) type (II) Al-OH species at ~ 3740 cm^{-1}; (b) type (III) Al-OH species at ~ 3700 cm^{-1} during Stage A adsorption.

Figure II-9 schematically illustrates the difference between Type II and Type III Al-OH species. Type II (~3740 cm^{-1}) Al-OH species are bridge bonded to two Al^{3+} ions according to the assignment of Knözinger and Ratnasamy,[41] where Type III (~3700 cm^{-1}) is coordinated to three Al^{3+} ions. On this basis, one might expect for Type II Al-OH species that dispersive adsorption forces would cause the TEDA molecules to become more parallel to the surface as a result of bending of the bridged Al-O-Al type moiety. In contrast, little or no bending of the Al_3-O moiety could occur. We postulate that hydrogen binding of TEDA to Type II Al-OH species would result in the production of the highest red shift of ν(OH), where type III Al-OH···TEDA binding produces a lower red shift. This postulate then suggests, for Stage A adsorption, a larger efficiency of complexation of type II Al-OH groups to TEDA, and the more efficient formation of the least red-shifted Al-OH···TEDA species, correlating the observations in Figure II-2 and Figure II-5.

Other physically adsorbed molecules have also been observed to produce a wide range of red shifts for Al-OH groups upon hydrogen bonding.[83,84] This is a distinct behavior for Al-OH groups, not observed for Si-OH groups on SiO_2 surfaces, which undergo hydrogen bonding to molecules such as CO and N_2 at low temperatures, producing only 100 cm^{-1} to 50 cm^{-1} red shifts respectively in -OH frequency.[78,79]

It is very clear from the spectroscopic data as a function of the equilibrium pressure of TEDA that two rather distinct stages of adsorption occur. In Stage A, the isolated Al-OH groups are almost completely converted to hydrogen-bonded groups, and this is complete at an equilibrium pressure of ~ 10 mTorr at 300 K. The integrated absorbance of the complexed Al-OH groups produced by a single TEDA molecule is approximately twice the original intensity of the isolated Al-OH species before adsorption, as may be seen in Figure II-3. In the equilibrium pressure range 10 – 250 mTorr, Stage B of TEDA adsorption mainly occurs. Figure II-3 shows that Stage B adsorption results in more than a factor of two increase in integrated -OH absorbance, compared to that achieved at the end of Stage A. By correlation to the integrated absorbance changes for two vibrational bands associated with the TEDA molecule (Figure II-4), it may be seen that Stage B adsorption occurs during the last ~ 30 % of the coverage of TEDA which develops up to an equilibrium pressure of 250 mTorr. Thus, the effect of the adsorption of a second TEDA molecule on a TEDA-complexed Al-OH group exceeds, by a factor of about six, that of the first TEDA molecule is-so-far as measured by the integrated -OH absorbance.

The hydrogen bonding of more than a single species to -OH groups has been observed in homogeneous phase.[85,86] For adsorption on -OH groups, the bonding of one and then a second CO molecule to Si-OH groups on SiO_2 surfaces has also been reported,[78] and well defined stages of CO adsorption by hydrogen bonding were observed by IR spectroscopy.

II.5.B Thermodynamics of Hydrogen Bonding of Al-OH Groups to TEDA

The equilibrium adsorption of TEDA on isolated Al-OH groups on Al_2O_3 occurs according to the Langmuir adsorption isotherm, based on the fits to the Langmuir model, as shown in Figure II-7. These fits have been made only in the Stage A region, where single TEDA molecule adsorption occurs on single isolated Al-OH groups. Fitting these data to the van't Hoff equation yields the value of $\Delta H_{ad} = -15.6 \pm 0.5$ kJ mol^{-1}.

This value of ΔH_{ad} is in the range often found for hydrogen bonding, where values from -25.2 kJ mol^{-1} to -12.6 kJ mol^{-1} are reported.[76] The physical adsorption of smaller molecules, having lower polarizability and less electron donor capability than TEDA gives slightly lower values for the adsorption enthalpy. For example, ΔH_{ad}(CO) on Si-OH groups is -11.3 kJ mol^{-1},[78] and $\Delta H_{ad}(N_2)$ on Si-OH groups is -13.4 kJ mol^{-1}.[79] Our method of measuring the fractional coverage of TEDA in the isotherm study measures only single TEDA molecules adsorbed on Al-OH groups, and is therefore specific to this mode of surface bonding.

II.5.C Other TEDA Bonding Sites

The experiments reported here have almost exclusively focused on the behavior of the Al-OH groups which initially form a hydrogen bond to a single TEDA molecule. At higher coverage a fraction of the hydrogen-bonded species involve two TEDA molecules. Other more detailed studies (unpublished) find minor spectroscopic differences in the TEDA spectrum for different levels of hydroxyl group coverage. This suggests the presence of TEDA binding to Lewis acid Al^{3+} sites via the N atom lone pair electrons. Because of the focus of this paper on the Al-OH made during TEDA adsorption, the results do not address TEDA binding to Lewis acid sites.

II.6 Summary

The bonding of the TEDA molecule to partially hydroxylated γ-Al_2O_3 has been studied by transmission IR spectroscopy and the formation of Al-OH···TEDA hydrogen bonds has been characterized. The following results are found:

1. Single TEDA molecules adsorb selectively on isolated Al-OH groups with an enthalpy of adsorption of ΔH_{ad} = -15.6 ±0.5 kJ mol^{-1} at $\theta = 0.5 - 0.6$.

2. Equilibrium adsorption on Al-OH groups follows the Langmuir adsorption isotherm.

3. A second TEDA molecule can bind to an Al-OH···TEDA species as the coverage is increased at 300 K.

4. The hydrogen bonding of TEDA to Al-OH groups causes large red shifts in the -OH stretching frequency ranging up to -1000 cm^{-1}.

5. The largest efficiency of hydrogen bonding of TEDA occurs with type (II) -OH species (~ 3740 cm^{-1}) compared to type (III) -OH species (~ 3700 cm^{-1}).

II.7 Acknowledgement

We acknowledge with thanks the support of this work by The Army Research Office, and discussion with Dr. Alex Balboa of Aberdeen Proving Ground and with Dr. Joseph Rossin of Guild Associates. We also acknowledge the suggestion by a reviewer of the possible ionic character of the Type II complex shown in Figure II-9.

III. Bonding of Triethylenediamine to Lewis Acid Al^{3+} Sites*

III.1 Abstract

The adsorption of triethylenediamine (TEDA) on Lewis acid (Al^{3+}) sites of the highly dehydroxylated Al_2O_3 surface has been observed FT-IR spectroscopy. This was done by monitoring the competitive adsorption of TEDA and CO on the Al^{3+} sites. A stoichiometric replacement of $Al^{3+} - CO$ species was observed as $Al^{3+} - TEDA$ surface species were formed.

---

* Reproduced with permission from S. Kim, O. Byl, J. T. Yates, Jr. "The Adsorption of Triethylenediamine on Al_2O_3-III: Bonding to Lewis Acid Al^{3+} Sites", Journal of Physical Chemistry B 109, 6331 (2005). Copyright 2005 American Chemical Society.

III.2 Introduction

The triethylenediamine (TEDA) (also named 1, 4-diazabicyclo[2.2.2]octane, DABCO) molecule is useful for functionalizing oxide and carbon surfaces by adsorption.[8,22,71,72]

We have recently demonstrated that TEDA bonds, via hydrogen bonding, to surface Al-OH groups.[81,87] This occurs in two stages where first a single TEDA molecule forms a hydrogen bond, Al-OH···(TEDA) and then a second TEDA molecule forms an Al-OH···$(TEDA)_2$ species. The bonding enthalpy for the Al···(TEDA) species formation is -15.6 ± 0.5 kJ mol^{-1}.

This report demonstrates that the TEDA molecule also bonds to Al^{3+} Lewis acid sites on the Al_2O_3 surface. The work was done by using chemisorbed CO as a marker for the Al^{3+} sites. Previous work has shown that CO behaves as a donor molecule when it bonds to Al^{3+} sites,[40,88] and that the vibrational frequency of ν(C-O) may be used to measure the relative Lewis acidity of the Al^{3+} sites.[89,90] The ν(C-O) frequency of the adsorbed CO molecule is observed to shift up by about 50 cm^{-1} from its gas phase value when bound to a Lewis acid Al^{3+} site. This is thought to be due to the electric field effect on the CO molecule (Stark effect).

III.3 Experimental Methods

The experimental methods used in this work are described in detail in reference.[81] The ultrahigh vacuum system for IR measurement is designed such that the IR beam passes through a tungsten grid into which a powdered Al_2O_3 sample is pressed. The temperature of the grid is controlled by cryogenic cooling and resistive heating. The cell is maintained at a base pressure < 1 x 10^{-8} Torr with a turbo-molecular pump. A MKS capacitance manometer and a Bayard-Alpert ionization gauge are used to measure pressure.

The γ-aluminum oxide powder obtained from Guild Associates (surface area = 250 m^2/g) is pressed into a tungsten grid (0.002″ thickness) using a hydraulic press.[39] A highly

dehydroxylated Al_2O_3 surface is obtained by heating the sample for several hours at 1300 K in vacuum.[39,48] Gases are introduced into the chamber quantitatively and the gas line is evacuated with a sorption pump and a turbo-molecular pump between the dosages of different gases.

The infrared spectra are recorded with a Bruker TENSOR 27 FT-IR spectrometer. The spectrometer and the enclosed IR cell are purged continuously by dry air from which CO_2 and H_2O has been removed. Each spectrum is obtained by averaging 128 interferograms at 2 cm^{-1} resolution.

III.4 Results and Discussion

Previously papers reported exclusively about the hydrogen bonding of TEDA on Al_2O_3 surface via Al-OH surface groups.[81,87] Al-OH groups as well as Lewis acid Al^{3+} sites are present on the highly dehydroxylated Al_2O_3 surface and TEDA would be also expected to adsorb at Lewis acid (Al^{3+}) sites on Al_2O_3.

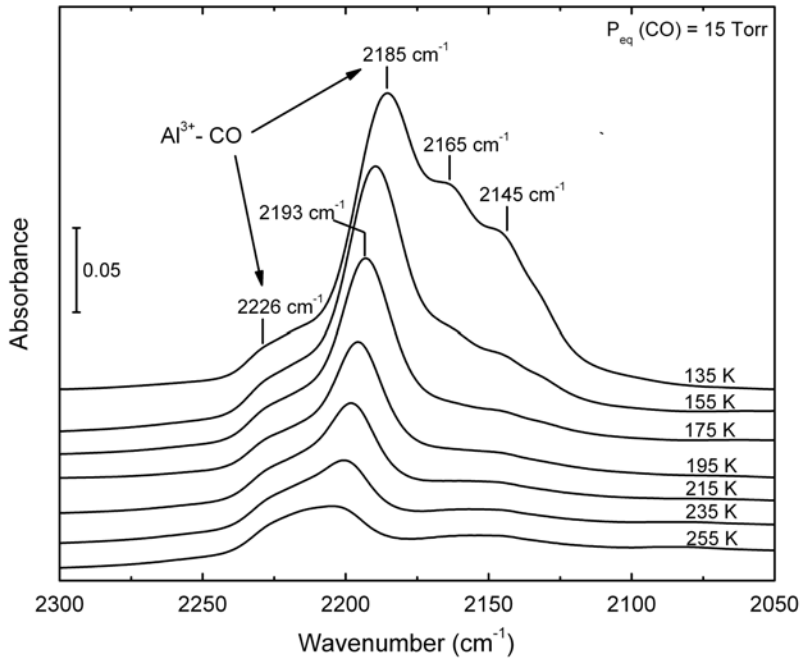

Figure III-1. FT-IR spectra of the decrease of CO adsorption on an Al_2O_3 surface upon heating up to 255 K, while maintaining the equilibrium CO pressure at 15 Torr.

The dependence of CO bonding onto the Al_2O_3 surface as a function of temperature at an equilibrium CO pressure of 15 Torr is shown in Figure III-1. The major ν(C-O) absorption band at ~ 2185 cm^{-1} and the shoulder features at ~ 2226 cm^{-1}, ~ 2165 cm^{-1} and ~ 2145 cm^{-1} are assigned to the CO bound to various sites on the Al_2O_3 surface.[40,47-49] The two bands at ~ 2165 cm^{-1} and ~ 2145 cm^{-1} are assigned to CO binding to the Al-OH groups by hydrogen bonding and to physically adsorbed CO respectively. These species are related to the production by CO adsorption on associated OH groups at ~ 3615 cm^{-1} (not shown). Upon heating from 135 K to 175 K under equilibrium conditions, the ν(C-O) modes (~ 2165 cm^{-1}, ~ 2145 cm^{-1}) are appreciably decreased in their absorbance, as Al-OH···CO and physically adsorbed CO species are depleted. The remaining ν(C-O) absorbances at 2193 cm^{-1} and 2226 cm^{-1} are due to CO binding to various Al^{3+} sites.[40,47-49] These features are due to CO adsorbed on coordinatively unsaturated octahedral and tetrahedral Al^{3+} sites respectively.[48,49] The temperature for our studies of the competition of TEDA and CO for Lewis acid sites on the Al_2O_3 surface has been chosen to be 175 K, where only chemisorbed CO binding to Lewis acid sites on Al_2O_3 is observed.

Various coverages of TEDA were adsorbed at 295 K on a highly activated Al_2O_3 surface containing small coverages of Al-OH sites and high coverages of Al^{3+} sites. The coverage of TEDA was monitored at equilibrium with gas phase TEDA in the pressure range up to ~ 10 mTorr, i.e. up to ~ 1 ML of TEDA.[81,87] After each TEDA adsorption dose at 295 K, gas phase TEDA was quickly pumped away, and the sample temperature was lowered to 175 K, and CO was admitted to 15 Torr pressure to saturate the empty Lewis acid sites still present. After that the sample was heated up to 295 K and evacuated in order to add more TEDA in the next adsorption step. The heating to 295 K caused complete desorption of CO. The spectra were taken at 175 K after CO was again adsorbed on the TEDA pre-covered Al_2O_3 surface. The relative

coverage of TEDA co-adsorbed with CO on the Lewis acid sites was calculated by integration of the TEDA IR feature near 1060 cm^{-1}, which is due to the δ(C-N) skeletal mode of the molecule, as shown in Figure III-2. The relative coverage of CO on the Al^{3+} sites was measured by integration of the ν(C-O) bands near 2193 cm^{-1} and 2226 cm^{-1}, as shown in Figure III-3.

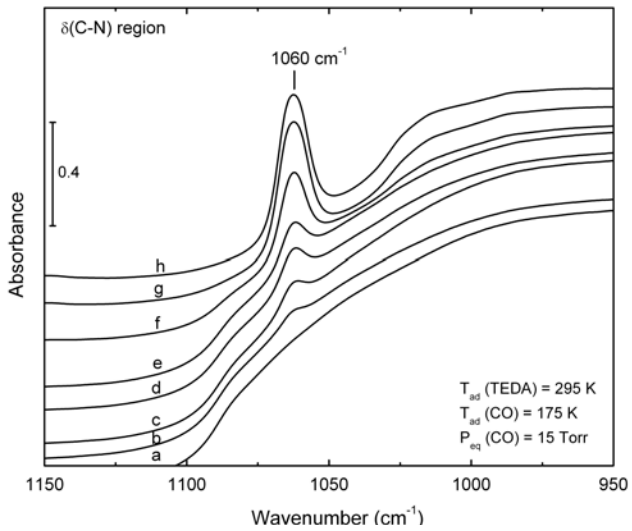

Figure III-2. FT-IR spectra of TEDA adsorption (δ(C-N) mode) to various coverages. Each measurement involves a mixture of chemisorbed TEDA and CO on Al^{3+} sites.

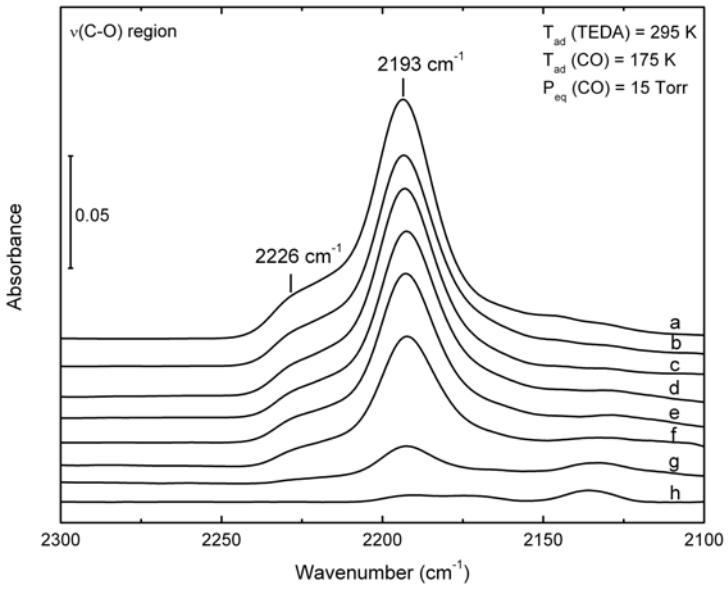

Figure III-3. FT-IR spectra of CO adsorption on Al_2O_3 containing various coverages of pre-adsorbed TEDA.

It may be seen by comparing Figures III-2 and III-3 that the monotonic increase in the absorbance due to the TEDA is accompanied by a monotonic decrease in absorbance of the CO molecule adsorbed on the Al^{3+} sites. As the coverage of TEDA is increased (g, h) a new feature at ~ 2135 cm^{-1} can be seen to develop in Figure III-3 and this is the subject of a future publication. Figure III-4 shows the inverse linear dependence of integrated absorbance for TEDA and CO molecules as they compete for Lewis acid sites. The linear relationship obtained indicates that stoichiometric Al^{3+} site blocking occurs when TEDA is adsorbed at 295 K, causing the saturated CO coverage to decrease with increased TEDA coverage.

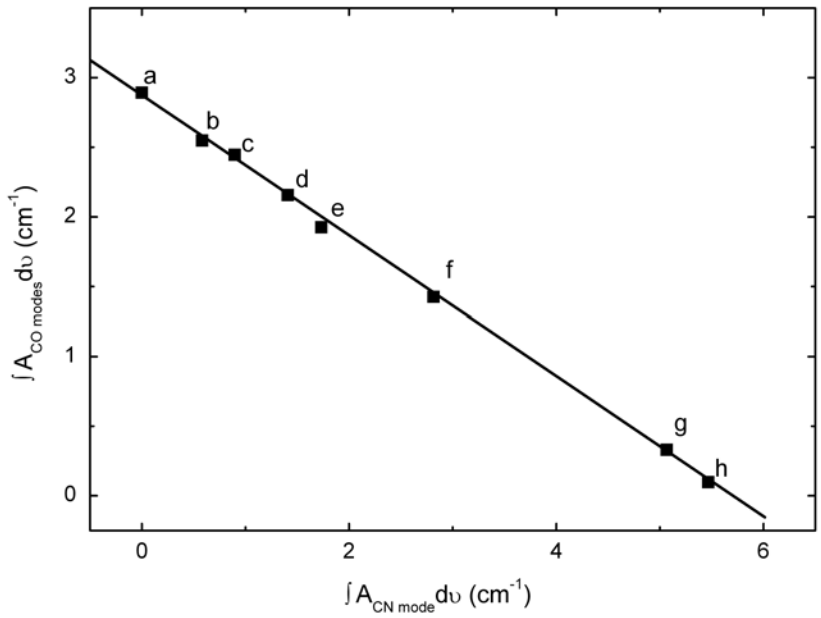

Figure III-4. The relationship between the integrated absorbance of ν(C-O) modes of Al^{3+}-CO species shown in Figure III-3 and the integrated absorbance of the δ(C-N) mode of pre-covered TEDA molecules shown in Figure III-2. A stoichiometric relationship between the coverage of TEDA and CO is seen for chemisorption on Al^{3+} sites.

III.5 Summary

The occupancy of Al^{3+} sites by adsorbed triethylenediamine (TEDA) has been demonstrated by observing the stoichiometric blocking of CO adsorption by TEDA on these

sites. Both CO and TEDA are electron donor molecule and the more strongly-bonded TEDA molecule effectively competes with CO for Al^{3+} sites in a stoichiometric manner on the Al_2O_3.

III.6 Acknowledgement

We acknowledge with thanks the support of this work by The Army Research Office, and discussion with Dr. Alex Balboa of Aberdeen Proving Ground and with Dr. Joseph Rossin of Guild Associates.

PART II. FT-IR Studies of Chemical Agent Adsorption on Amine- functionalized γ-Al_2O_3 Surface

IV. Perturbation of Adsorbed CO by Amine Derivatives Coadsorbed on the γ-Al_2O_3 Surface*

IV.1 Abstract

The coadsorption of CO and triethylenediamine (TEDA) (also called 1, 4-diazabicyclo [2.2.2]octane, DABCO) on a high area γ-Al_2O_3 surface has been investigated using transmission FTIR spectroscopy. It has been found that TEDA binds more strongly to both Lewis acid sites and to Brønsted- Al-OH sites than does CO. Competition experiments indicate that TEDA displaces CO to less strong binding sites. Evidence for weak CO···TEDA interactions is found in which small ν(CO) redshifts are produced. Comparison between different amines such as triethylenemonoamine (TEMA) (also called 1-azabicyclo[2,2,2]octane, ABCO), trimethylamine (TMA), and ammonia indicate that the ν(CO) redshift increases with increasing amine polarizability, indicating that the redshift is mainly due to dipole image damping effects on the CO oscillator frequency. The direct bonding between the exposed N lone pair electrons of the TEDA molecule and CO does not occur.

First principles theoretical studies have characterized the bonding of CO with γ-Al_2O_3 Lewis acid sites of various types as well as TEDA bonding to both Lewis acid sites and to Al-OH groups. The theoretical studies also indicate that strong bonding of adsorbed CO with TEDA molecules does not occur, and that the observed decrease in the binding energy of CO when coadsorbed with TEDA on γ-Al_2O_3 is expected.

---

* Reproduced with permission from S. Kim, D. C. Sorescu, O. Byl, J. T. Yates, Jr. "The Perturbation of Adsorbed CO by Amine Derivatives Coadsorbed on the γ-Al_2O_3 Surface - FTIR and First Principles Studies", Journal of Physical Chemistry B 110, 4742 (2006). Copyright 2006 American Chemical Society.

IV.2 Introduction

The adsorption behavior of triethylenediamine (TEDA) (also called 1, 4-diazabicyclo [2.2.2]octane, DABCO) on the high area γ-Al_2O_3 surface has been studied previously using transmission FTIR spectroscopy.[81,87,91] It was demonstrated that TEDA binds to Al-OH Brønsted acid sites via hydrogen bonding as well as to Al^{3+} Lewis acid sites on the Al_2O_3 surface. TEDA adsorption by hydrogen bonding involves both Al-OH···(TEDA) and Al-OH···$(TEDA)_2$ species formation.

Since TEDA has been used to enhance the adsorption capacity of various high area surfaces (charcoal, silicate, zeolite, etc.) for capture of chemical agents,[8,22,24,71,72] we have investigated the role of TEDA functionalization of γ-Al_2O_3 on the adsorption of carbon monoxide, using transmission FTIR spectroscopy. We find that CO binds weakly to TEDA on the Al_2O_3 surface causing the CO vibrational mode to be red–shifted by - 8 cm^{-1} from the frequency of CO(g). For this study other amines such as triethylenemonoamine (TEMA) (also called 1-azabicyclo[2,2,2]octane, ABCO), trimethylamine (TMA), and ammonia have also been employed for comparison with TEDA functionalization of γ-Al_2O_3 surfaces.

IV.3 Experimental & Computational Methods

IV.3.A Experiment

The experimental methods used in this work are described in detail in reference.[81] The turbo-pumped ultrahigh vacuum system (base pressure < 1×10^{-8} Torr) is designed to study a high area solid surface by transmission IR spectroscopy. A tungsten grid, into which γ-aluminum oxide powder is pressed at 70,000 psi, is clamped to a manipulator assembly with copper mounting rods which serve to conduct electrical heating current to the sample as well as to cool

the sample using contact with liquid N_2. A thermocouple is welded to the grid in order to measure and control the temperature of the sample between 83 K and 1500 K.

The Al_2O_3 powder is obtained from Guild Associates (surface area = 250 m^2/g, which was measured before heat treatment). The prepared Al_2O_3 sample is heated up to 1000 K for 1 min in vacuum to produce a highly dehydroxylated surface.[39-41,73,74,81] Triethylenediamine (TEDA) and triethylenemonoamine (TEMA) are obtained from Aldrich and used without further purification. Trimethylamine (TMA) and ammonia were also employed. Gases are introduced into the chamber quantitatively and the gas line is evacuated with a sorption pump and a turbo-molecular pump between the dosages of different gases.

The infrared spectra are recorded with a Bruker TENSOR 27 FT-IR spectrometer. Each spectrum is obtained by averaging 128 interferograms with 2 cm^{-1} resolution and the background spectrum taken through the empty grid region is subtracted.

IV.3.B Computational Methods

Two sets of calculations have been performed in the current study. The first set aimed to describe gas phase properties and the interaction between TEDA and CO molecules in the gas phase. These investigations have been done using Gaussian 03 suite of programs.[92] In this case the geometrical structure optimizations and vibrational frequency calculations have been done at the MP2/cc-pVDZ theory level. Further analysis of polarizability for a small set of amines (NH_3, TMA, TEMA and TEDA) has been performed at the MP2/cc-pVDZ level. In the case of NH_3 and TMA and TEDA molecules the polarizability results have been further refined by calculations at the MP2/aug-cc-pVTZ level.

The second set of theoretical investigations focused on description of the interaction between TEDA and CO molecules upon adsorption on the γ-Al_2O_3 surface. The calculations

performed in this study were done using the Vienna *ab initio* simulation package (VASP).[93-95] This program evaluates the total energy of periodically repeating geometries based on density-functional theory and the pseudopotential approximation. In this case the electron-ion interaction has been described by fully non-local optimized ultrasoft pseudopotentials (USPPs) similar to those introduced by Vanderbilt.[96,97] Periodic boundary conditions are used, with the one-electron pseudo-orbitals expanded over a plane-wave basis set. The cutoff energy used in these calculations was 495 eV corresponding to precision level *high* in VASP code.[98]

All calculations related to adsorption properties of CO and TEDA molecules on the γ-Al_2O_3 surface have been done using the PW91 generalized gradient approximation (GGA) of Perdew *et al*.[99] The sampling of the Brillouin zone was performed using a Monkhorst-Pack scheme[100] using grid mesh with a k-point separation of 0.05 $Å^{-1}$. The minimization of the electronic free energy was performed using an efficient iterative matrix-diagonalization routine based on a sequential band-by-band residuum minimization method (RMM)[93,94] or alternatively based on preconditioned band-by-band conjugate-gradient (CG) minimization.[101] The optimization of different atomic configurations was performed by conjugate-gradient minimization of the total energy.

The crystallographic structure of bulk γ-alumina was taken according to that reported by Digne.[34] In this model the monoclinic crystallographic unit cell of γ-Al_2O_3 contains 8 Al_2O_3 formula units. Based on a fit of the dependence of the unit cell energy on the corresponding cell volume with the Murnaghan equation of state,[34] an optimum volume of the unit cell of 381.592 $Å^3$ has been determined. The calculated cell volume per Al_2O_3 unit of 47.69 $Å^3/Al_2O_3$ unit is about 2.82 % larger than the one obtained experimentally (46.39 $Å^3/Al_2O_3$ unit).[102] The bulk modulus at zero pressure obtained from a Murnaghan analysis is 166.7 GPa, value which is also

close to the reported experimental data of 162 ±14 GPa.[103] The corresponding optimized lattice parameters were found to be a_{calc} = 5.598 Å, b_{calc} = 8.432 Å, c_{calc} = 8.083 Å, and β = 90.53°. These values are slightly larger by about 1.5% than those reported previously by Digne et al. based on plane-wave calculations using a cutoff energy of 300 eV.[104]

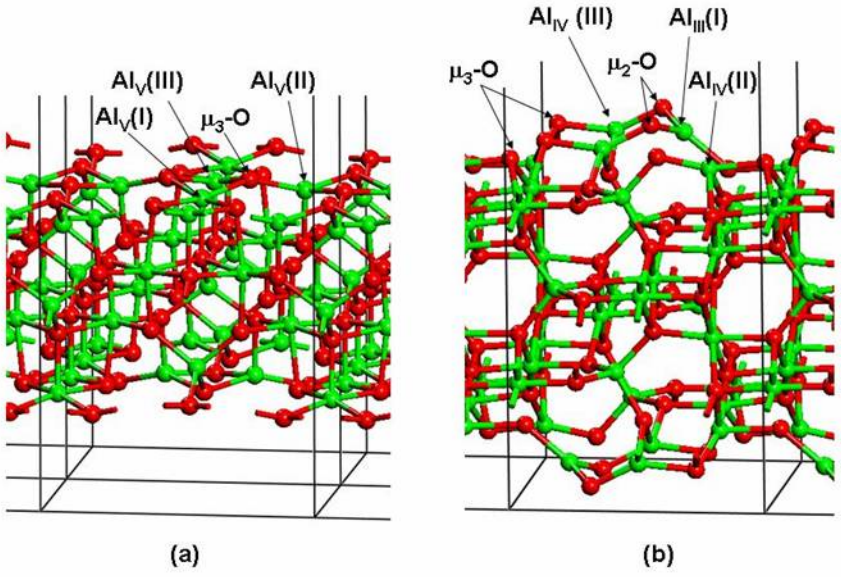

Figure IV-1. Pictorial view of the slab models used to describe the properties of (a). (100) and (b). (110) surfaces of the γ-Al_2O_3 surface. On the (100) surface the five-fold coordinated aluminum, Al_V, and three-fold oxygen, μ-O_3, sites are indicated. On the (110) surface the three-fold coordinated aluminum, Al_{III}, four-fold coordinated aluminum, Al_{IV} (II and III), two-fold coordinated oxygen, μ-O_2, and three-fold coordinated oxygen, μ-O_3, are indicated.

As was shown in previous studies,[37,104,105] the predominant surface orientations of γ-alumina are the (110) surface (70 – 83 %) followed by the (100) surface which accounts for about 17 % of the exposed surface. Consequently, in the current study we focused on these two types of surfaces exclusively. Following Ref. [34] these surfaces have been simulated using slab models with at least eight atomic planes (see Figure IV-1). Each slab was taken to be symmetrical to avoid unphysical dipole-dipole interactions between neighbor slabs. For the (110) and (100) surfaces the calculated surface energies were found to be 1498 mJ/m^2 and 958 mJ/m^2

similar to values of 1540 mJ/m^2 and 970 mJ/m^2, respectively obtained by Digne et al.[34] Following notation introduced in Ref. [34] the (100) surface presents five-fold coordinated aluminum atoms (denoted as Al_V) and three-fold coordinated oxygen atoms (denoted as μ_3-O in Figure IV-1a). In contradistinction, the (110) surface (see Figure IV-1b) presents several types of coordinated Al and O atoms, namely three-fold Al_{III} (I) and four-fold Al_{IV} (II and III) aluminum sites and two-fold μ_2-O and three-fold μ_3-O oxygen atoms.

Beside the description of surface properties, the plane-wave DFT method employed in the current work is also adequate for description of molecular systems of interest, namely CO and TEDA molecules. For example, the optimized bond length of an isolated CO molecule was found equal to 1.1453 Å and the vibrational frequency ν(C-O) = 2105.8 cm^{-1}. These values differ by 1.5 % and 1.7 %, from the experimental values of 1.128 Å and 2143 cm^{-1}, respectively[106] and they are practically identical to the theoretical results reported by Digne et al.[34] Similarly, based on optimizations of an isolated TEDA molecule in a cubic box of length 12 Å, we found that this molecule has D_{3h} symmetry with r(C-C) = 1.5624 Å, r(N-C) = 1.4711 Å, and r(C-H) = 1.0988 Å. These values are very close to those obtained using Gaussian 03 calculations[107] at MP2/cc-pVDZ level (r(C-C) = 1.5609 Å, r(N-C) = 1.4723 Å, and r(C-H) = 1.1042 Å).

The agreement between our results for the description of both the bulk and the surfaces of γ-alumina or of isolated TEDA and CO molecules with either experimental values or other high-level first principles calculations gives us confidence for the next step of our investigations, namely the theoretical investigation of the interactions of TEDA and CO molecules with the (110) and (100) surface of γ-alumina.

IV.4 Results – Experimental Studies

IV.4.A CO adsorption on nonfunctionalized γ-Al_2O_3

Carbon monoxide adsorption on the γ-Al_2O_3 surface has been studied extensively.[40,47-49] Because of the variety of adsorption sites on the Al_2O_3 surface, several ν(C-O) absorption bands are observed.

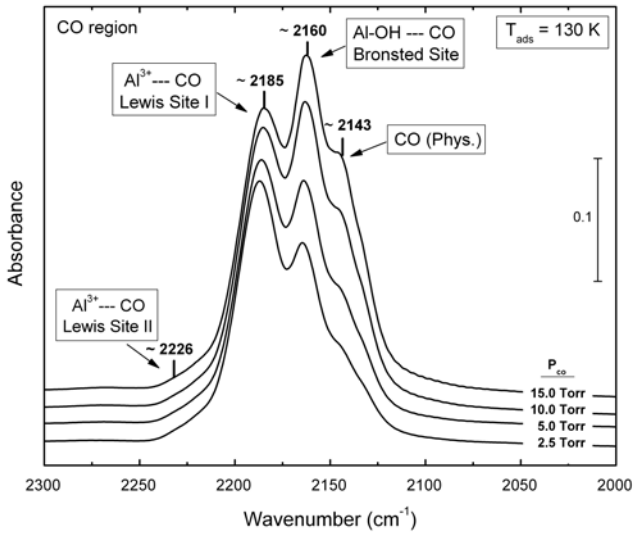

Figure IV-2. FTIR spectra of the CO adsorption on the Al_2O_3 surface with increasing CO exposure at P = 2.5, 5.0, 10.0, and 15.0 Torr and T = 130 K.

Figure IV-2 shows the IR spectrum for CO adsorption onto the Al_2O_3 surface for increasing CO pressure at 130 K. Because of the higher adsorption energy of CO on Lewis acid sites of the Al_2O_3 surface,[106] the absorbance for the vibrational modes at ~ 2226 cm^{-1} and ~ 2185 cm^{-1} develop first and almost saturate at P_{co} ~ 2.5 Torr. The adsorbed CO on Al-OH Brønsted acid sites at ν(CO) ≅ 2160 cm^{-1} and the physisorbed CO at ν(CO) ≅ 2143 cm^{-1} begin to form later and continue to develop up to P_{co} ~ 15 Torr of CO equilibrium pressure.

IV.4.B CO adsorption on TEDA-functionalized Al_2O_3.

When CO is exposed to a TEDA-precovered Al_2O_3 surface, the CO species observed on the unfunctionalized Al_2O_3 surface are absent and a new feature with ν(CO) ~ 2135 cm^{-1} is produced as shown in Figure IV-3.

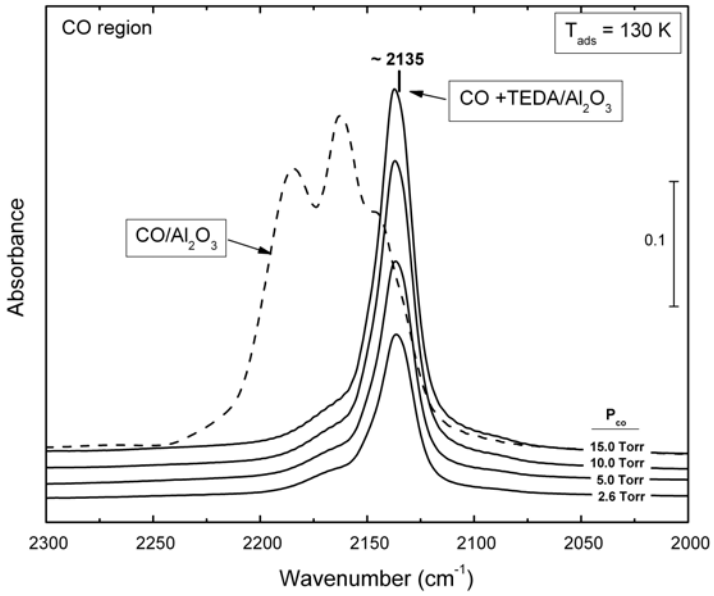

Figure IV-3. FTIR spectra of the CO adsorption on the TEDA-precovered Al_2O_3 surface with increasing CO exposure at P = 2.6, 5.0, 10.0, and 15.0 Torr, compared to the CO adsorption on the unfunctionalized Al_2O_3 surface at 15.0 Torr (dashed line) from Figure IV-2.

The pre-dosed pressure of the TEDA was chosen in the range of 10 ~ 15 mTorr where the binding of TEDA on Al_2O_3 surface was saturated.[81,87,91] As demonstrated in our previous studies,[81,87,91] TEDA competes with CO for the Al^{3+} Lewis acid and Al-OH Brønsted acid sites on the Al_2O_3 surface. Since these sites on the surface are already blocked with pre-dosed TEDA, the new feature at ~ 2135 cm^{-1} is likely to be caused by the CO and TEDA interaction. However, no significant change in the TEDA vibrational spectral region as well as in the Al-OH region occurs during CO exposure. This reveals that the CO interaction with TEDA is relatively weak.

The dependence of CO binding with the TEDA-functionalized Al_2O_3 as a function of temperature at an equilibrium CO pressure of 15 Torr is shown in Figure IV-4. The adsorbed CO

on the TEDA-precovered Al_2O_3 surface desorbs completely near 200 K. The enthalpy of CO adsorption on TEDA-precovered surface was measured to be -2.0 ± 0.3 kcal/mol from the van't Hoff plot as shown in the inset of Figure IV-4. The weakly-bound CO adsorbed on TEDA-precovered surfaces exhibits only ~ 1/3 the value of $\Delta H_{ad}(CO)$ for Lewis acid sites of the Al_2O_3 surface, which is estimated to be in the range of -4.8 to -7.1 kcal/mol.[40,47]

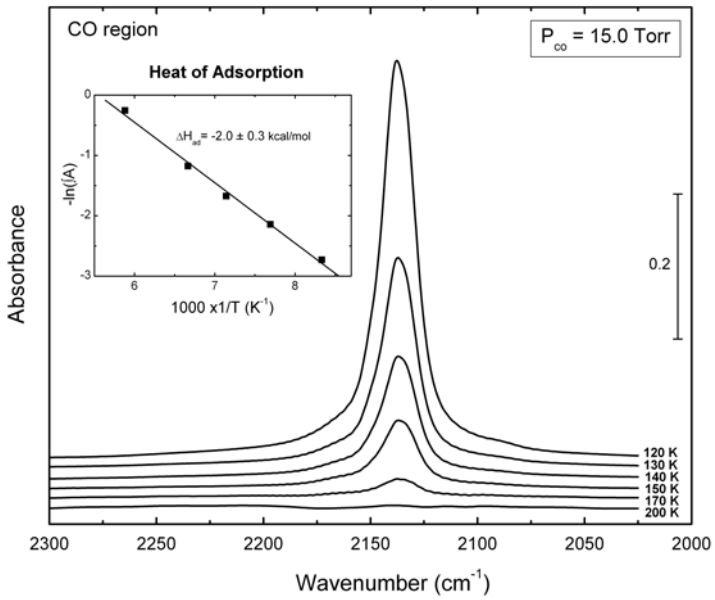

Figure IV-4. FTIR spectra showing the decrease of CO adsorption on the TEDA-precovered Al_2O_3 surface upon heating up to 200 K, while maintaining the equilibrium CO pressure at 15 Torr. The van't Hoff plot of -ln ($\int A_{co}$) vs. 1/T in the left insert yields $\Delta H_a d(CO)$ = -2.0 ± 0.3 kcal/mol on TEDA-precovered Al_2O_3.

IV.4.C Spectroscopic observation of site competition by CO during amine desorption from Al_2O_3

Because TEDA and other amines desorb intact from Al2O381,87,91 it is possible to perform a site competition experiment in which the TEDA (or other amine) molecules are slowly removed by thermal desorption in the presence of excess CO(g). As amine desorption occurs, the CO perturbed by the amine disappears and is replaced by CO adsorbed on sites vacated by the amine species. The desorbed amine is condensed on the outer surface of the Dewar filled with liquid N2. This experiment is schematically illustrated in Figure IV-5.

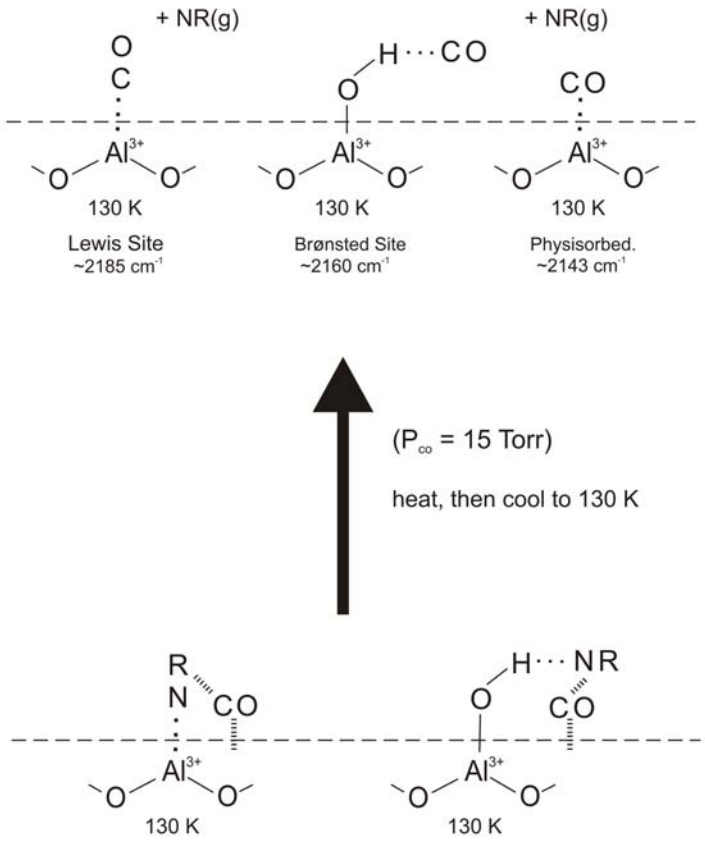

Figure IV-5. Schematic diagram of the CO adsorption site competition experiment with various amine molecules.

At the bottom of Figure IV-5, a complex of CO with the surface and with the amine (NR) is shown at 130 K. Amine molecules bound to both Al^{3+} sites and to Al-OH groups are indicated, in accordance with our findings for the TEDA molecule.[81,87,91] As amine molecules desorb thermally to produce NR(g), CO repopulates the surface at sites originally occupied by the amine molecule. Spectroscopic observations are made after cooling to the starting temperature of 130 K following desorption experiments at successively higher temperatures.

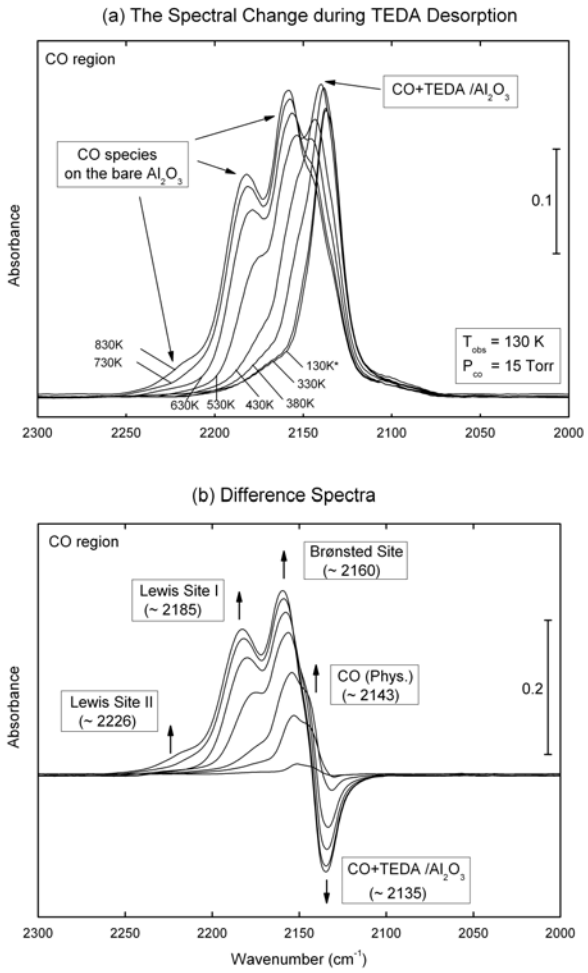

Figure IV-6. The spectral change of the adsorbed CO on TEDA-precovered Al_2O_3 surface (a) before (130 K*) and after heating the sample to T = 330, 380, 430, 530, 630, 730, and 830 K. All the spectra were taken at 130 K, at an equilibrium CO pressure of 15.0 Torr. (b) The difference spectra obtained by subtracting the original spectrum which is noted as 130 K* in (a).

Figure IV-6 shows a sequence of experiments supporting the scheme in Figure IV-5 in which heating up to 830 K is carried out, followed by cooling under excess CO(g). Figure IV-6(a) shows the actual spectra; Figure IV-6(b) shows difference spectra which are very informative. In Figure IV-6(b) we observe the loss of the CO absorbance at ~ 2135 cm^{-1} associated with the CO···TEDA/Al_2O_3 complex, and the concomitant formation of CO species bound to Brønsted sites and to the two types of Lewis acid sites. In addition, evidence for CO physisorption (~ 2143 cm^{-1}) is seen clearly in the difference spectra.

Figure IV-7 shows a set of difference spectra for similar experiments to those of Figure IV-6, in which TEMA, TMA, and NH_3 adsorbates are systematically desorbed with site repopulation by CO. The temperature range for each experiment is given in the figure caption. The behavior of TEDA, TEMA, TMA, and ammonia functionalities are very similar in the following ways:

1. A complex between the CO and the various amines is observed in each case with a low ν(CO) frequency.
2. This complex disappears as heating under CO(g) takes place and both Al-OH···CO and Al^{3+}-CO species are recovered as the amine coverage decreases, vacating Al-OH and Al^{3+} sites.

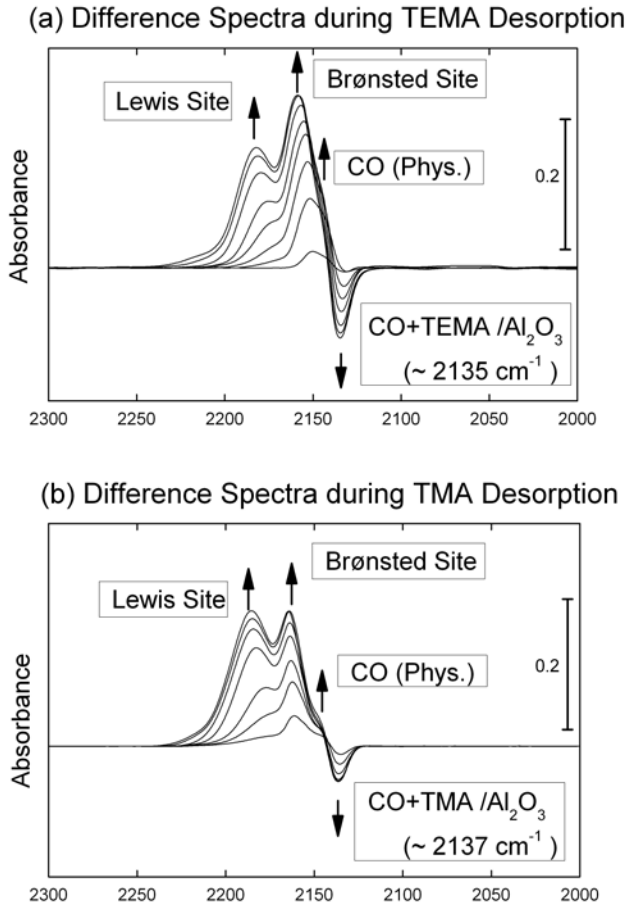

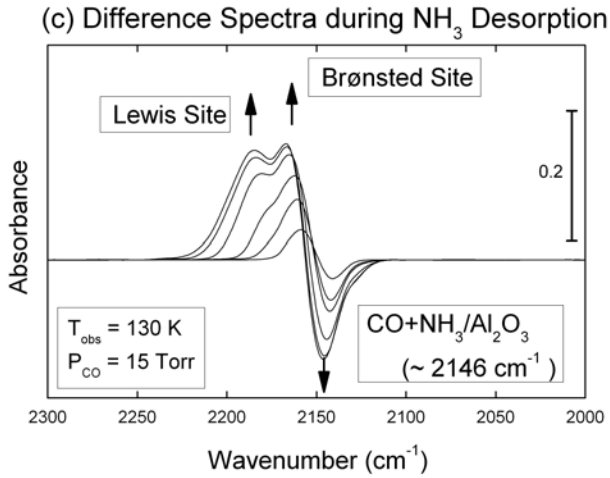

Figure IV-7. The difference spectra of adsorbed CO on : (a) the TEMA-precovered Al_2O_3 surface before and after heating sample to T = 330, 380, 430, 480, 530, 630, 730, and 830 K.; (b) the TMA-precovered Al_2O_3 surface before and upon heating sample to T = 330, 380, 430, 530, 630, 730, and 830 K.; (c) the NH_3-precovered Al_2O_3 surface before and upon heating sample to T = 330, 380, 430, 480, 530, 630, and 730 K. All the spectra were taken at 130 K after heating, at an equilibrium CO pressure of 15.0 Torr.

IV.4.D Comparative studies of amine desorption by FTIR

Figure IV-8 shows a plot of the normalized amine desorption behavior for the four molecules which form a surface complex with adsorbed CO, causing its C-O frequency to decrease. The normalized absorbances of the δ(N-H) mode at ~ 1240 cm^{-1} (NH_3) and the δ(C-H) modes at ~ 1240 cm^{-1} (TMA), at ~ 1202 cm^{-1} (TEMA), and at ~ 1323 cm^{-1} (TEDA) are plotted as a function of the temperature as shown in Figure IV-8. To within our experimental error, all four amines exhibit similar behavior in their desorption kinetics. This behavior is a composite of amine desorption processes from both Al-OH bonding sites and Al^{3+} bonding sites, and desorption occurs over a very wide temperature range by a sequence of kinetic processes which are not investigated in this work.

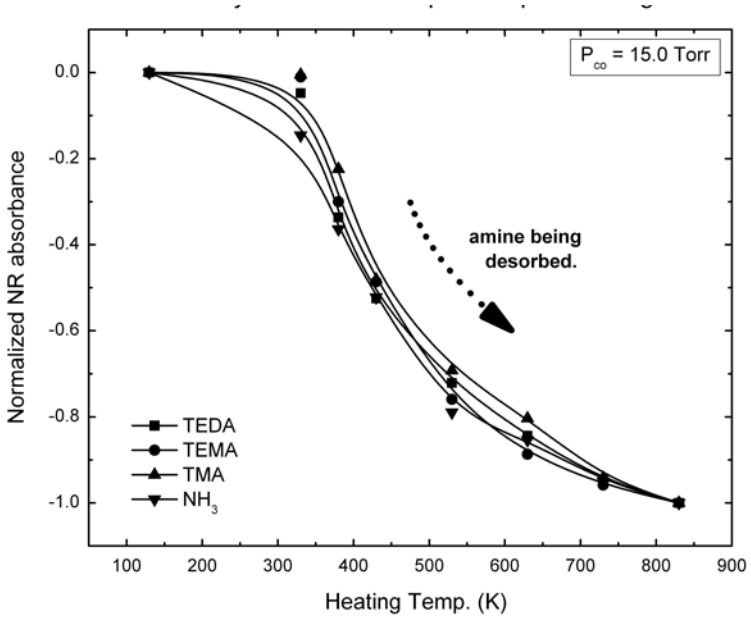

Figure IV-8. The decrease in the normalized absorbance of a selected vibrational mode of the precovered amine upon heating up in steps to 830 K in the CO adsorption site competition experiment. The δ(N-H) mode at ~ 1240 cm^{-1} (NH3) and the δ(C-H) modes at ~ 1240 cm^{-1} (TMA), at ~ 1202 cm^{-1} (TEMA), and at ~ 1323 cm^{-1} (TEDA) are selected in each measurement.

IV.5 Results – Theoretical Studies

IV.5.A Interaction of CO and TEDA molecules in gas phase

In a first set of theoretical investigations we focused on a description of the interaction properties between CO and TEDA molecules in gas phase. Several configurations of the CO molecule around TEDA have been considered corresponding to face, bridge and end-on conformations. In each case, frequency calculations have been performed to confirm the existence of a local minimum on the potential energy surface. The resulting configurations, which have been found to correspond to a local minimum on the potential energy surface, are presented in Figure IV-9.

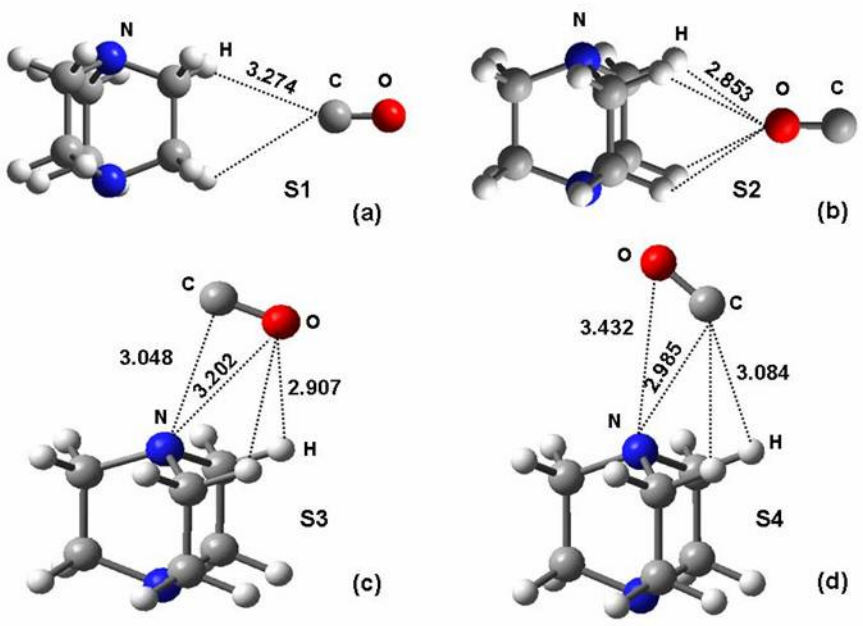

Figure IV-9. Pictorial view of the isomeric forms of the TEDA-CO complex as determined based on molecular orbital calculations at MP2/cc-pVDZ level of theory: (a) edge perpendicular structure (S1), (b) face perpendicular structure (S2) (c) and (d) end-tilt structures (S3 and S4).

In this figure, the edge and face perpendicular structures S1 and S2 have been found to have C_{2v} symmetry while the end tilted configurations S3 and S4 have C_s symmetry. In all four cases the CO bond distances seem to be little affected with values ranging between 1.147 – 1.148 Å. Similarly, the CO stretching frequencies are only weakly modified relative to the MP2/cc-pVDZ calculated vibrational frequency of isolated CO of 2113.9 cm^{-1}, namely $\Delta\nu_1 = 1.0$ cm^{-1} for S1, $\Delta\nu_2 = -8.9$ cm^{-1} for S2, $\Delta\nu_3 = -9.9$ cm^{-1} for S3 and $\Delta\nu_4 = -2.9$ cm^{-1} for S4. When the above identified structures are further optimized by considering the counterpoise correction, we found that only structures S2 and S4 correspond to a local minimum. The S1 structure was found to correspond to a second order saddle point while structure S3 is a transition state. Using the basis set superposition error corrected energies we estimate very small binding energies of CO to TEDA with values of 0.48 kcal/mol for S2 and 1.1 kcal/mol for S4 configurations, respectively.

These results indicate very small interaction energies between TEDA and CO molecules in the gas phase.

IV.5.B Adsorption and coadsorption of CO and TEDA molecules on (100) and (110) surfaces of γ-Al_2O_3

The adsorption studies of individual CO and TEDA molecules and the coadsorption of TEDA-CO molecules on the γ-Al_2O_3 surface were done using the slab models presented in Figure IV-1, corresponding to the (100) and (110) surface orientations. The corresponding adsorption energies calculated throughout this work were obtained based on the expression

$$E_{ads} = E_{molec} + E_{slab} - E_{(molec+slab)} \qquad \text{(IV-1)}$$

where E_{molec} is the energy of the isolated adsorbate molecule in its equilibrium position, E_{slab} is the total energy of the slab and $E_{(molec+slab)}$ is the total energy of the adsorbate/slab system. A positive E_{ads} corresponds to a stable adsorbate/slab system. The energy of the isolated adsorbate molecule was determined from calculations performed on a single molecule in a cubic cell of length 12 Å. The same Brillouin-zone sampling has been used to calculate the energies of the bare slab and of the molecule-slab systems.

As the current experimental work has been done in high vacuum conditions using surfaces annealed up to 1000 K it is considered that the main spectral features observed will be mainly due to interaction of adsorbates with unsaturated Al ion sites. Consequently, in our theoretical work we have focused first on the description of adsorption at these sites and on identification of the corresponding CO stretching frequencies. The corresponding results related to adsorption of isolated CO molecules on (100) and (110) surfaces of γ-Al_2O_3 surface are presented in Table 3 while representative configurations are depicted in Figures IV-10(a)-(c).

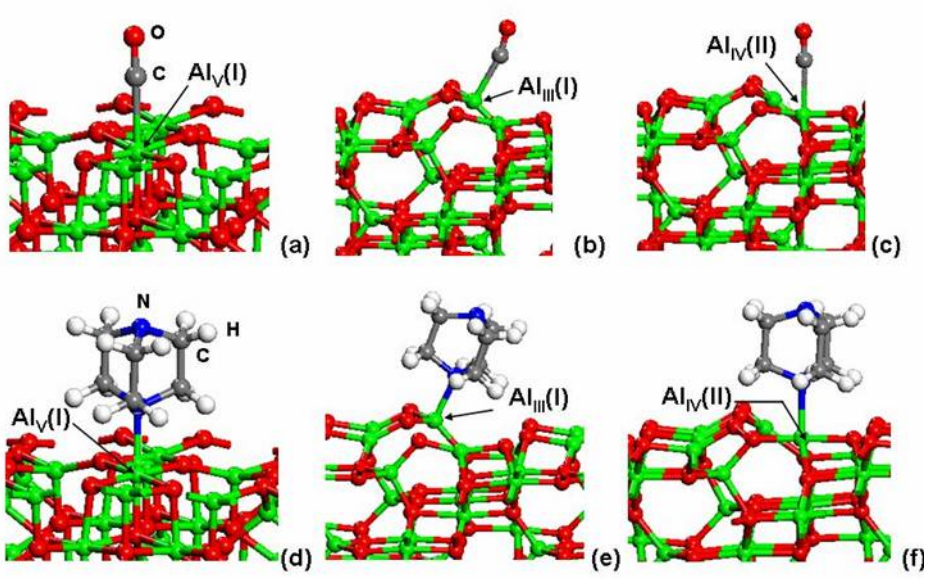

Figure IV-10. Representative adsorption configurations of CO and TEDA molecules on (100) and (110) γ-Al_2O_3 surfaces. Panels (a) and (d) correspond to (100) surface while the remaining panels correspond to the adsorption configuration on the (110) surface.

Table 3. Calculated equilibrium distances and adsorption energies for CO, TEDA and OH molecules on (100) and (110) surfaces of γ-Al_2O_3 surface. In the case of CO structures the corresponding frequency shift δν(C-O) with respect to the calculated gas phase vibration frequency of 2105.8 cm^{-1} is also indicated.[1]

System/ Surface	Site	d(Al…CO)/[2] d(Al…OH)	d(C-O)/[2] d(O-H)	d(Al…N)/ d(OH...N)	E_{ads}[3]	δν(C-O)
a) CO Adsorption						
(100)	Al_V(I)	2.158	1.141		9.5	24.2
	Al_V(II)	2.305	1.142		4.6	16.2
	Al_V(III)	2.231	1.142		5.3	10.1
(110)	Al_{III}(I)	2.136	1.137		17.1	64.1
	Al_{IV}(II)	2.184	1.141		9.6	28.2
	Al_{IV}(III)	2.239	1.142		4.0	21.4
b) TEDA Adsorption						
(100)	Al_V(I)			2.244	19.3	
	Al_V(II)			2.323	13.8	
	Al_V(III)			2.152	18.3	
(110)	Al_{III}(I)			2.014	40.0	
	Al_{IV}(II)			2.080	27.0	
	Al_{IV}(III)			2.145	17.4	

(Table 3, Continued)

c) CO…TEDA Coadsorption						
(100)	T(Al_V(I))-CO(Al_V(II))	2.256	1.147	2.265	4.6	-26.1
	T(Alv(I))-CO(Alv(III))	2.632	1.146	2.251	0.4	-17.8
	T(Al_V(III))-CO(Al_V(I))	2.232	1.145	2.237	1.1	-18.8
	T(Alv(III))-CO(Alv(II))	2.355	1.145	2.168	1.8	-17.0
(110)	T(Al_{III}(I))-CO(Al_{IV}(III))	2.457	1.141	2.013	2.8	-10.6
	T(Al_{IV}(II))-CO(Al_{IV}(III))	2.372	1.148	2.093	1.0	-29.1
d) OH Adsorption						
(100)	μ_1-Al_V(I)	1.809	0.974		37.5	
	μ_1-Al_V(II)	1.858	0.977		28.6	
	μ_1-Al_V(III)	1.771	0.970		35.0	
(110)	μ_1-Al_{III}(I)	1.692	0.968		61.1	
	μ_1-Al_{IV}(III)	1.792	0.974		35.7	
	μ_2-Al_{IV}(III)	1.936	0.975		44.7	
e) OH-TEDA Adsorption						
(100)	μ_1-Al_V(III)-TEDA	1.791	0.973	2.171	16.4	
(110)	μ_1-Al_{III}(I)-TEDA	1.697	0.975	1.977	17.9	
	μ_1-Al_{IV}(II)-TEDA	1.773	0.981	2.102	18.3	
	μ_2-Al_{IV}(II)-TEDA	1.954	0.983	2.214	17.0	
f) OH-TEDA...CO Coadsorption						
(100)	OH(Alv(III))-TEDA...	1.780	0.977	2.068		
	CO(Al_V(II))	2.229	1.147		6.4	-26.0
(110)	μ_1-Al_{III}(II)-TEDA...	1.710	0.974	2.067		
	CO(Al_{IV}(III))	2.488	1.150		2.4	-51.0
	μ_1-Al_{III}(II)-TEDA...	1.778	0.980	2.129		
	CO(Al_{IV}(II))	2.216	1.144		5.0	-11.8

[1]Bond distances are given in Angstroms, adsorption energies in kcal/mol and vibrational frequency shifts in cm^{-1}.

[2] The bond distance d(Al…CO) is considered in the case of CO adsorption, d(Al…OH) is considered in the case of OH adsorption and d(OH…N) is considered for TEDA binding to OH group. Similarly, d(C-O) and d(O-H) relate the corresponding bond distances in the case of CO and respectively, OH adsorption.

[3] In the case of coadsorption studies only the adsorption energy of CO is reported; this was calculated with respect to isolated gas phase CO molecule and the surface with preadsorbed TEDA or OH-TEDA molecules, respectively.

We found that on the (100) surface, the CO molecule binds on Lewis Al^{3+} sites with adsorption energies ranging from 4.6 to 9.5 kcal/mol while on the (110) surface the binding increases to values up to 17.1 kcal/mol. The higher binding energies correspond to Al atoms with a high degree of unsaturation as is the case of Al_{III}(I) sites on the (110) surface. Corresponding to these changes in the binding energy there is also a corresponding upward vibrational shift (blue shift) in the range of 10 – 64 cm^{-1} (see section a) in Table 3) with the largest shifts obtained for the case of (110) surface. These results are very similar to those reported before by Digne et al.[34] who have analyzed in detail the effect of hydration upon the surface Lewis acidity.

In the case of TEDA adsorption, the results of adsorption calculations are also given in section b of Table 3 while representative configurations are depicted in Figure IV-10, panels (d)-(f). It can be seen from these figures and data in Table 3 that the TEDA molecule adsorbs with N towards the unsaturated Al sites of the surface at Al…N separations in the range 2.014 – 2.323 Å. Similar to the CO case, adsorption of the TEDA molecule is the strongest in the case of the (110) surface, particularly for the case of binding at Al_{IV}(II) and Al_{III}(I) sites which are the most uncoordinated. In these cases the binding energy increases to 27 and 40 kcal/mol respectively. Based on these results it follows that the TEDA molecule interacts significantly more strongly with both (100) and (110) surfaces of γ-Al_2O_3 compared to CO.

One main implication of the above presented results is that in the case of coadsorption studies in which the TEDA molecule was adsorbed prior to CO adsorption, it is expected that all surface sites which present the strongest interaction with TEDA, namely Al_V(I) on the (100) surface and respectively Al_{III}(I) and Al_{IV}(II) sites on the (110) surface will be primarily occupied by TEDA molecules. In order to further understand the effect upon binding and vibrational properties of CO when exposed to a TEDA-precovered Al_2O_3 surface we have considered that

the TEDA molecule will occupy the most stable surface sites while the CO molecule will adsorb at nearby surface sites, exhibiting an interaction with TEDA. The corresponding results are given in section c) of Table 3 while representative configurations are depicted in Figure IV-11.

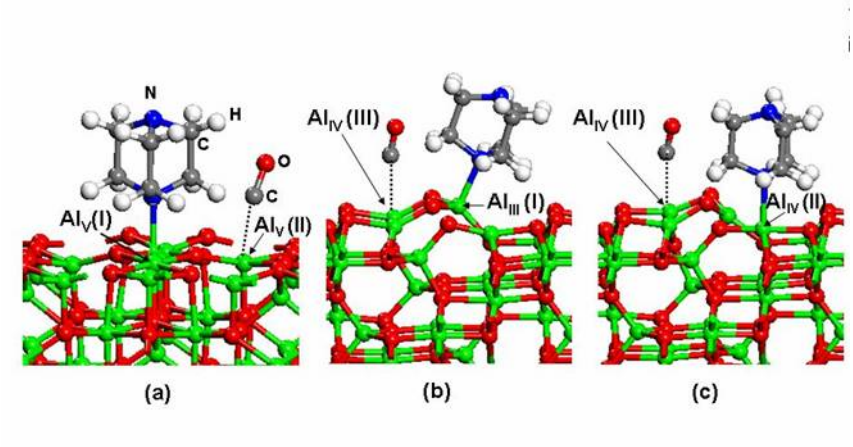

Figure IV-11. Representative coadsorption configurations of TEDA and CO molecules on (100) Al_2O_3 (panel a) and (110) Al_2O_3 (panels b and c).

From the data given in Table 3 it follows that a significant weakening of the CO bonding to the surface takes place in the vicinity of a bound TEDA molecule. In particular, in the case of the (110) surface which is the dominant orientation in the case of polycrystalline Al_2O_3, the binding energies of CO on the TEDA-precovered surface have small values in the range 1.0 – 2.8 kcal/mol. This binding energy compares favorably with the experimental result (2.0 ±0.3 kcal/mol) shown in Figure IV-4. Our calculations also show that for both (100) and (110) surface orientations, important downward shifts of the C-O vibrational frequencies occur compared to gas phase CO with shifts in the range -10.6 to -29.1 cm^{-1}. The experimental shift for the CO···TEDA/Al_2O_3 case is -8 cm^{-1} as seen in Figure IV-5.

Beside adsorption at the unsaturated Al^{3+} sites, we have also analyzed the possibility of TEDA molecules adsorbing at Al-OH Brønsted acid sites. In their previous study Digne et al.[34] have done a systematic study of the hydration process for γ-alumina and of the corresponding

modifications of OH-stretching frequencies. In this study we will restrict our investigations to the case of small coverage of OH species with the intention to determine how the TEDA molecule will adsorb at such sites. The corresponding results are presented in sections d) and e) of Table 3. Our calculations confirm that the TEDA molecule adsorbs on hydroxyl groups by formation of O-H···N hydrogen bonds. This confirms earlier experimental studies.[87] As indicated in Table 3 the OH···N bond distances exhibit variations between 2.095 – 2.214 Å. The highest binding energy of 31.9 kcal/mol is obtained for the case when the OH group is adsorbed at the Al_{III}(I) unsaturated site on the (110) surface. However, in all the other cases we investigated there is only a small dependence on the surface site and OH orientation, as reflected by the corresponding binding energies with values in the range 16.4 – 18.3 kcal/mol for the OH···TEDA binding energy, in the limit of zero coverage. Experiments measured an energy of ~ 3.7 kcal/mol[87] which is probably so low compared to the calculated energy because of the higher TEDA coverage in the experiments.

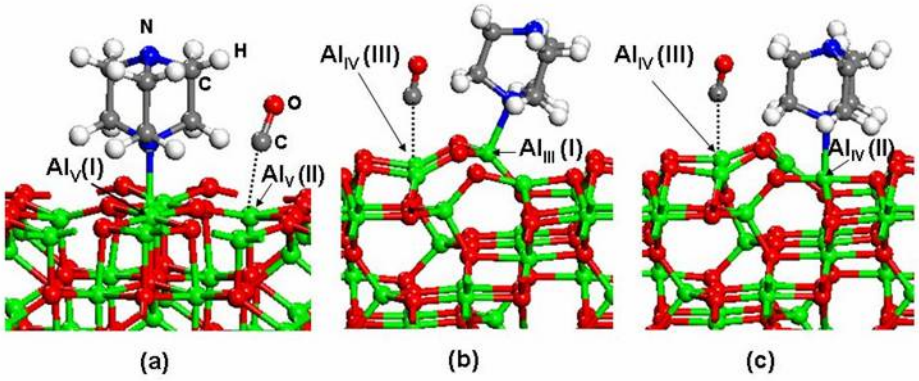

Figure IV-12. Representative adsorption configurations of TEDA molecule at OH Brønsted sites on (100) Al_2O_3 (panel a) and (110) Al_2O_3 (panels b and c).

A final point we have analyzed was related to modifications of the CO vibrational frequencies in the case of coadsorption with TEDA molecules adsorbed at hydroxyl sites. This

point has been considered only for few configurations indicated in Table 3 section f). The results obtained indicate a downward shift of CO vibrational frequencies relative to gas phase values. Consequently, our calculations support the fact that independent of the type of Lewis or Brønsted surface sites at which the TEDA molecule adsorbs on the surface, when CO molecules are coadsorbed at nearby unsaturated aluminum sites a downward shift of the CO vibrational mode frequency will take place.

IV.6 Discussion

IV.6.A CO adsorption on TEDA-precovered Al_2O_3 surface

In this study we found a weakly-bound CO species on the TEDA-precovered Al_2O_3 surface. The existence of this CO···TEDA complex species with ν(CO) ~ 2135 cm^{-1} is evident from the TEDA thermal desorption experiment (Figure IV-6). As the coverage of TEDA is decreased by successive heating, the absorbance of adsorbed CO species on the TEDA-precovered surface also decreases in the difference spectrum as shown Figure IV-6(b). By heating the sample up to 830 K most of the TEDA (~99%) desorbs from the surface. As a result, the spectral feature in the CO region (see Figure IV-6(a)) becomes identical to that observed in Figure IV-2, corresponding to CO adsorption on the unfunctionalized Al_2O_3 surface.

Additional insight into the geometry of the CO···TEDA complex can be obtained by analyzing CO adsorption on TEMA-precovered surfaces. TEMA has the same cage structure as TEDA with one of the terminal nitrogen atoms replaced by a carbon atom. The spectrum of the adsorbed TEMA on Al_2O_3 surfaces (not shown here) shows the production of a broad band centered at ~ 3530 cm^{-1}, which is assigned to the Al-OH mode which has been shifted due to interaction with the TEMA molecule, while the δ(C-N) mode is red-shifted by - 8 cm^{-1} from the gas phase frequency. These vibrational spectral changes agree with the idea that TEMA also

adsorbs on the Al_2O_3 surface via the N atom anchored to surface as would be expected. Upon TEMA adsorption followed by exposure to CO(g) a new spectral feature at frequency 2135 cm^{-1} is observed (see Figure IV-7(a)), similar to that observed in the case of CO adsorption on the TEDA-functionalized surface. This result indicates that it would be very unlikely that a CO molecule binds to the exposed N atom of TEDA molecules in an end-on bonding configuration, since ν(CO) for the TEDA···CO and the TEMA···CO complexes are identical. These findings are also consistent to the results of *ab initio* molecular orbital calculations. As is discussed in Section IV-5.A, the interactions between TEDA and CO molecules in the gas phase are very weak, with binding energies in the range 0.5 – 1.0 kcal/mol. For this reason it is expected that direct bonding of CO and TEDA molecules is not significant and consequently on the Al_2O_3 surface the CO molecule will rather bind to the surfaces sites unoccupied by TEDA molecules, and will be weakly influenced by neighbor TEDA molecules. In our experimental work, adsorption of CO was carried out on a TEDA-precovered surface. It is expected that TEDA molecules will occupy the most energetically favorable sites while CO molecules will be positioned on the remaining surface sites in the vicinity of TEDA molecules. Based on this surface occupation scheme, our calculated results presented in Section c of Table 3 have shown that a significant weakening of CO binding with the surface takes place in the case of TEDA-CO coadsorption relative to the case when only CO molecules are adsorbed on the surface. Consistent with this binding energy trend, we have determined that the CO modes in the TEDA···CO complex are red-shifted by - 10.6 to - 29.1 cm^{-1} compared to the vibrational frequency of CO in the gas phase. These theoretical findings are also in agreement with our experimental results where a ν(CO) red shift of - 8 cm^{-1} is observed.

IV.6.B CO adsorption on the clean Al_2O_3 surfaces

In this work the Al_2O_3 sample was prepared by heating at 1000 K and the oxide surface is mostly dehydrated and exposes mainly unsaturated Al^{3+} sites. We have shown in the theoretical section (see Figure IV-1) that several Al_V, Al_{IV} and Al_{III} unsaturated aluminum atom sites (Lewis acid sites) can be identified on both (100) and (110) surfaces with the (110) surface having a higher surface density of broken Al-O bonds[34] than the (100) surface. The results of our DFT plane-wave calculations in conjunction with slab model calculation have indicated that both TEDA and CO molecules can adsorb at these unsaturated Al ion sites, but the bonding energy of TEDA molecules is higher than that of CO molecules on these sites. Upon adsorption at such Lewis acid sites, a blue shift in ν(CO) in the range of 10 to 64 cm^{-1} relative to the gas phase value has been determined for ν(CO). Such a blue shift is caused by strong electron-withdrawing properties of the Al^{3+} sites. This shift is correlated to the strength of CO bonding to the surface which varies in the order $E_{ads}(Al_V) \leq E_{ads}(Al_{IV}) < E_{ads}(Al_{III})$. It is highest in the case of Al_{III} sites on the (110) surface.

IV.6.C TEDA adsorption on the clean Al_2O_3 surface

Besides adsorption of TEDA on unsaturated Al sites we have determined that TEDA molecules can also adsorb on Brønsted OH sites by formation of OH···N hydrogen bonds.[81,87] As determined by theory, the binding in this case occurs with energies in the range 16.4 – 18.3 kcal/mol which is somewhat weaker than found for direct TEDA bonding to unsaturated Al sites. Additionally, based on a limited set of coadsorption studies, we have determined that the CO vibrational frequency for the OH···TEDA···CO complex is also red-shifted relative to the gas phase value. These results suggest that the measured shift of the CO vibrational frequency can be

used both as a measure of the surface acidity as well as an indicator of the amount of TEDA (or other amine molecules) present on the surface.

IV.6.D Perturbation of adsorbed CO on various amine-precovered surfaces

In the site competition experiment with TMA and NH_3, as the precovered amine desorbs thermally, the difference spectra in the CO vibrational mode region also indicate the loss of a weakly interacting CO···TEDA complex, as is shown in Figure IV-7(b) and 7(c). In the report by Hadjiivanov et al.[108] they could not find either any evidence of a direct interaction between CO and pre-adsorbed NH_3 on a TiO_2 surface. They mentioned the possibility that CO might adsorb physically on the ammonia-covered part of the surface judging by the enhancement of the physically adsorbed CO mode after coadsorption. In our current work, the shifted ν(CO) mode of the weak CO···amine complex was clearly resolved by the site competition experiment.

The observed mode shifts of CO on various amine-precovered surfaces are shown in Table 4 together with the polarizability value for each amine as determined from *ab initio* molecular orbital calculations. It can be observed that as the CO molecule interacts with polarizable amine molecules in the order NH_3 < TMA < TEMA/TEDA. The ν(CO) vibrational frequency of the CO···amine complex appears to move increasingly downward, as the amine polarizability increases, as would be expected for vibrational shifts due primarily to image effects.[109]

Table 4. The Effect of Amine Derivatives on the Frequency Shifts of Adsorbed CO

Observed Mode Shift (cm^{-1}) 2143 (cm^{-1})[1]	**Effective Mode Shift** (cm^{-1})	α^2 (Bohr^3)	
		Cal.[3]	**Exp.**[4]
NH_3 (+ 3)	+**3**	**14.18** (8.73)	**14.72**
TMA (- 6)	**- 9**	**50.62** (42.69)	**55.02**
TEDA (- 8)	**- 11**	**82.57** (72.61)	
TEMA (- 8)	**- 11**	(75.60)	

[1] The frequency of the CO vibrational mode in the gas phase.
[2] Isotropic polarizability.
[3] The calculation was done at the MP2/aug-cc-pVTZ level with Gaussian 03 program. The values in parentheses are from the calculation with MP2/cc-pVDZ basis set.
[4] The experimental values are from ref. [110].

The desorption behavior of amines on Al_2O_3 is monitored by plotting the normalized absorbance of the vibrational mode of the various amines upon desorption, as shown Figure IV-8. The essentially coincident curves for the four amines show that there is little difference in the desorption kinetics of these amines on Al_2O_3 surfaces. The amount of remaining amine after heating up to 830 K can be calculated by integrating the absorbance of one of the selected vibrational modes. The final coverage of amines is below ~ 5 % of the initial amount of amine on the surface in all cases. All the amines which are used in this study are classified as strong

bases by the value of the ionization constants of onium acids ($pK_a(BH^+)$) which are in the range of 8.5 to 11.0. On the assumption that these amines have similar reactivity and binding to the Al_2O_3 surface, the trend of showing more downward CO vibrational frequency with the more polarizable amine molecule can be explained best by the image dipole effect for the dynamic dipole of the CO molecule. As the polarizability of a pre-adsorbed amine become larger, the amine would support a stronger induced image dipole for the CO oscillator, resulting in stronger damping and in a larger red shift.[78,109-113] Since the chemical bonding effect between CO and chemisorbed amine can be estimated to be +3 cm^{-1} from the mode shift of CO on the ammonia-precovered surface (where there is little image-dipole effect for the NH_3), the real dynamic dipole image effects of other amines can be deduced as shown in Table 4, using the +3 cm^{-1} shifted frequency as a reference.

IV.7 Summary

The interaction of CO and triethylenediamine (TEDA), coadsorbed on γ-Al_2O_3, has been studied using transmission infrared spectroscopy and first principles theory. The following results have been obtained:

1. The interaction of the adsorbed TEDA molecule with chemisorbed CO on γ-Al_2O_3 is very weak as indicated by the presence of a slightly red-shifted ν(CO) mode at ~ 2135 cm^{-1}. The studies with CO will therefore provide a comparison to other molecule – amine surface complexes where strong interactions are expected.

2. The enthalpy of CO adsorption on the TEDA-functionalized surface is measured to be -2.0 ± 0.3 kcal/mol which is much smaller than the enthalpy of CO adsorption on the unfunctionalized surface (- 4.8 to - 7.1 kcal/mol).

3. By comparing the interaction of CO with TEDA-functionalized and TEMA-functionalized surfaces, no evidence is found for the bond formation between CO and the exposed basic N atom of the TEDA functionality.

4. First principles theoretical analysis indicates that chemical bond formation between adsorbed TEDA and CO is absent and that the observed decrease in CO binding energy for a TEDA-functionalized surface is expected.

5. The small redshift in ν(CO), due to interaction with a series of coadsorbed amines on Al_2O_3, increases as the polarizability of the amine increases, indicating that image dipole effects are mainly involved in causing damping of the CO oscillator.

IV.8 Acknowledgement

We acknowledge with thanks the support of this work by The Army Research Office, and discussion with Dr. Alex Balboa of Aberdeen Proving Ground and with Dr. Joseph Rossin of Guild Associates. Grants of computer time at the Army Research Laboratory and Pittsburgh Supercomputer Center are also gratefully acknowledged.

V. Competitive Adsorption between TEDA and HCN on the γ-Al_2O_3 surface*

V.1 Abstract

The adsorption and vibrational properties of chemisorbed HCN on Lewis acid sites, Lewis base sites, and Brønsted Al-OH acid sites on a partially hydroxylated γ-Al_2O_3 surface have been obtained by a combination of FTIR and density functional theory studies. The vibrational modes from the molecular and dissociative adsorption of HCN were assigned by using deuterium and ^{13}C labeled D^{13}CN molecules at 170 K. In addition, η^2(C, N)-HCN bonding is also found from the ν(C=N) vibrational spectra. Good correlation of the calculated vibrational frequencies for the adsorbed species with experimental data is found.

The effect of triethylenediamine (TEDA) (also called 1, 4-diazabicyclo [2.2.2]octane, DABCO) on the adsorption of hydrogen cyanide (HCN), on the high area γ-Al_2O_3 surface has been investigated using transmission FTIR spectroscopy. During HCN adsorption on TEDA-functionalized surfaces there is no spectral change or emerging feature in either the TEDA or HCN spectral regions, indicating that no direct interaction occurs between these two molecules. Instead, we found that TEDA competes with HCN for the active sites on γ-Al_2O_3. The observed ν(C≡N) mode on a TEDA-precovered surface is due to the HCN adsorption on Lewis base sites (Al-*O*-Al) which are less affected by TEDA pre-adsorption.

V.2 Introduction

Research on the adsorption of HCN on oxide surfaces has a long history,[114-118] but the precise identification of different binding modes based on infrared spectroscopic measurements is still lacking, especially on the γ-Al_2O_3 surface. It is generally accepted that HCN adsorbs molecularly as well as dissociatively on oxide surfaces, and polymerization of HCN is also reported. On silicate and titania surfaces, the formation of isocyanide species (M-NC) as well as cyanide species (M-CN) from HCN adsorption has been observed and assigned by using isotopically-labeled hydrogen cyanide.[116,117] In contrast to the dissociative adsorption of HCN, studies of the non-dissociated species and their binding sites have not been made, so that the vibrational assignment of HCN on Lewis acid, Lewis base, and Brønsted acid sites has not been made. This investigation focuses on this point. In addition, we have observed η^2 (C,N)-HCN binding to γ-Al_2O_3 where N and C atoms bond simultaneously to a pair of Al and O sites at 170 K. The experimental results are compared to DFT calculations.

We have also investigated the role of triethylenediamine (TEDA) (also called 1, 4-diazabicyclo[2.2.2]octane, DABCO) functionalization of γ-Al_2O_3 on the adsorption of hydrogen cyanide. The TEDA molecule is used as an impregnant to enhance the adsorption of chemical agents and other toxic industrial compounds such as HCN, ClCN, SO_2, H_2S, CH_3I, etc. on activated charcoal adsorbents.[15,22,72,119] It is believed that the amine groups present on the opposite ends of the TEDA molecule provide the chemical bonding to the charcoal surface as well as an amine site on the opposite end of the TEDA molecule for subsequently adsorbed species. In order to enhance the sorptive properties of TEDA-treated charcoal, additional functionalization with Cu^{2+} cations is often employed. For HCN adsorption, Cu^{2+} functionalization of TEDA-treated surfaces has been shown to be important.[23] Theoretical

studies suggest the existence of significant interactions between the Cu^{2+} center and HCN with binding energies for the HCN···Cu^{2+} complex as high as ~ 112 kcal mol^{-1}, whereas the HCN···TEDA complex exhibits a much smaller binding energy of only ~ 7 kcal mol^{-1}.[120]

In this work, no evidence of a direct interaction between TEDA and HCN molecules is found. Instead, it is shown that TEDA competes with HCN for the active sites on γ-Al_2O_3. The saturated coverage of adsorbed HCN molecules on TEDA-precovered γ-Al_2O_3, judging from the integrated absorbance of the ν(C≡N) modes, falls to ~ 1/7 of its value on unfunctionalized γ-Al_2O_3.

V.3 Experimental and Computational Methods

V.3.A Experimental

The experimental methods used in this work were described in detail previously.[81] The high vacuum infrared cell system (base pressure ≅ 1 × 10^{-8} Torr) was designed to provide temperature control of a high area solid adsorbent from 83 K to above 1400 K. The cell has two KBr windows, allowing the IR beam to pass through a tungsten grid, into which γ-aluminum oxide powder is pressed.[39,40]

The Al_2O_3 powder was obtained from Guild Associates (surface area = 250 m^2/g). The Al_2O_3 sample was briefly heated to 1000 K in vacuum to produce a highly dehydroxylated surface.[39-41,74] The triethylenediamine (TEDA) and triethylenemonoamine (TEMA also called 1-azabicyclo[2,2,2]octane, ABCO) were obtained from Aldrich. HCN was prepared by the reaction of KCN with H_2SO_4.[121] $D^{13}CN$ was obtained commercially. The isotopic purity of the $D^{13}CN$ was checked using a quadrupole mass spectrometer (QMS) and by IR spectroscopy and was found to be higher than 90 % (the main impurity is $H^{13}CN$).

TEDA vapor was admitted into the chamber, with the temperature of the alumina sample at 300 K, to form the adsorbed phase of TEDA.[81] After TEDA adsorption, the chamber was evacuated by a turbo-molecular pump and then the TEDA-functionalized alumina sample was exposed to HCN(g) at 170 K. The infrared spectra were recorded at each indicated temperature with a Bruker TENSOR 27 FT-IR spectrometer. Each spectrum was obtained by averaging 64 interferograms with 2 cm^{-1} resolution and the background spectrum, taken through the empty grid region, was subtracted.

V.3.B Computational Method.

The theoretical work performed in this study focused on a description of the chemisorption and vibrational properties of HCN and CN species adsorbed on the γ-Al_2O_3 surface. The computational method used for this purpose is similar to that employed by us to describe the chemisorption properties of TEDA and CO molecules on the same surface.[122] As a result, here we will provide only the essential elements for the current work.

The calculations were performed using the Vienna *ab initio* simulation package (VASP).[93-95,122] This program evaluates the total energy of periodically repeating geometries based on density-functional theory and the pseudopotential approximation. In this case the electron-ion interaction has been described by fully non-local optimized ultrasoft pseudopotentials (USPPs) similar to those introduced by Vanderbilt.[96,97] Periodic boundary conditions are used, with the one-electron pseudo-orbitals expanded over a plane-wave basis set with a cutoff energy of 495 eV.

The adsorption properties of HCN and CN species on the γ-Al_2O_3 surface have been done using PW91 generalized gradient approximation (GGA) of Perdew *et al*.[99] Spin polarized calculations have been considered for the case of radical species. The sampling of the Brillouin

zone was performed using a Monkhorst-Pack scheme[100] using a grid mesh with a k-point separation of 0.05 $Å^{-1}$.

The crystallographic structure of bulk γ-alumina was taken according to the structure reported in Ref. [34]. We have considered the adsorption properties on both (100) and (110) surfaces of γ-Al_2O_3, as these surface orientations have been shown to be predominant for the exposed surface.[34,37,105] These surfaces have been simulated using slab models with at least eight atomic planes. Each slab was taken to be symmetrical to avoid unphysical dipole-dipole interactions between neighbor slabs. Further details of the relaxation and surface energies for these surfaces can be found in our previous work.[122] We note here the diversity of surface sites on these surfaces. Specifically, the (100) surface presents five-fold coordinated aluminum atoms (denoted as Al_V) and three-fold coordinated oxygen atoms (denoted as μ_3-O) while the (110) surface presents several types of coordinated Al and O atoms, namely three-fold Al_{III} (I) and four-fold Al_{IV} (II and III) aluminum sites and two-fold (μ_2-O) and three-fold (μ_3-O) oxygen atoms.

Beside an accurate description of the γ-Al_2O_3 surface as described in our previous work[122] the current plane-wave DFT method employed is also adequate for description of the geometric parameters and vibrational properties of HCN and CN species. For the HCN(g) molecule, the optimized bond lengths were found equal to r(C-N) = 1.156 Å, r(C-H) = 1.069 Å while for the CN(g) radical the equilibrium distance is 1.065 Å. These values are in very good agreement to corresponding experimental values of r_{exp}(C-N) = 1.153 Å, r_{exp}(C-H) = 1.065 Å for HCN, and of 1.172 Å for the CN radical. Similarly, the calculated vibrational frequencies for the HCN molecule of ν(C-N) = 2107 cm^{-1}, ν(C-H) = 3382 cm^{-1}, and for CN radical of 2067 cm^{-1}

were found to reproduce sufficiently accurately the experimental data, namely ν_{exp}(C-N) = 2097 cm^{-1}, ν_{exp}(C-H) = 3311 cm^{-1} for the HCN molecule, and 2068 cm^{-1} for the CN radical.

On the Based on this comparison to experimental data, it is expected that the current computational method, previously proven to be accurate for the description of the adsorption properties of TEDA and CO molecules on γ-Al_2O_3,[18] is also adequate to describe the chemisorption properties of HCN and CN species on γ- Al_2O_3 surfaces.

V.4 Results: Experimental Studies

V.4.A HCN Adsorption on Clean γ-Al_2O_3 Surfaces

Figures V-1 and V-2 show the IR spectra for the HCN adsorption at 170 K, followed by heating up to 290 K at an HCN equilibrium pressure of ~15 mTorr. The infrared spectra in the ν(O-H), ν(C-H) region and the ν(C≡N) region are shown and group frequency assignments for the various species are indicated in bold letters on the labels in the spectra. In addition, for ease of understanding, the bold arrows indicate the growth or loss of absorbance upon heating. Two broad bands develop in the 3600 cm^{-1} – 3300 cm^{-1} region, and in the 3300 cm^{-1} – 2800 cm^{-1} region, and a sharp peak at ~ 3300 cm^{-1} is observed to develop upon HCN exposure at 170 K as shown in Figure V-1.

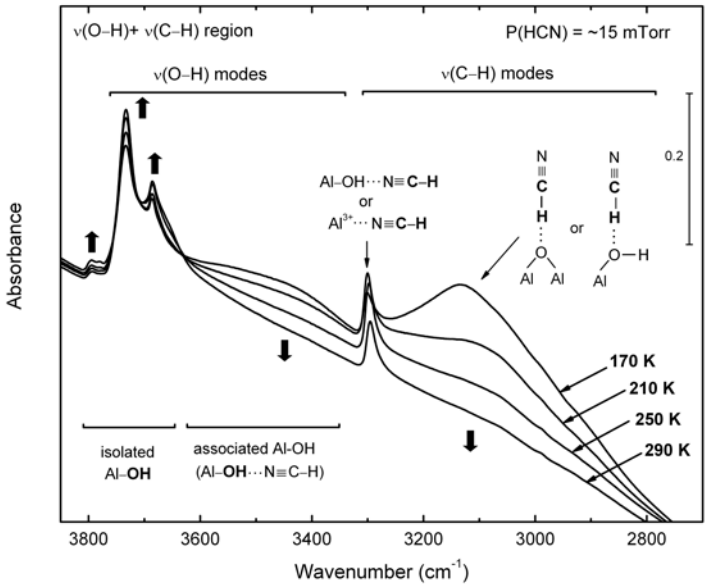

Figure V-1. FTIR spectra for HCN adsorption on Al_2O_3 at 170 K followed by sequential heating to 290 K at an HCN equilibrium pressure of ~15 mTorr.

The HCN molecule can adsorb on the surface either via a nitrogen atom or via a hydrogen atom. The hydrogen bonding of HCN molecules through the N atom to Al-OH groups (Brønsted acid sites) produces the associated OH species (3600 cm^{-1} – 3300 cm^{-1}), consuming the higher frequency isolated Al-OH species, as is often observed for hydrogen bonding of adsorbed molecules (stages of adsorption not shown). In addition to this type of surface binding, the HCN adsorption on Al^{3+} ions (Lewis acid sites) occurs via the nitrogen atom of HCN. Both of these HCN bonding structures produce a sharp ν(C-H) mode for HCN as observed at ~ 3300 cm^{-1}. In addition to Brønsted acid and Lewis acid sites, Lewis base sites also exist on partially dehydroxylated γ-Al_2O_3 (hereafter denoted Al-*O*-Al). HCN molecules bind to these sites via hydrogen bonding, producing strongly red-shifted and broadened C-H modes as seen in the ~ 3300 cm^{-1} – ~ 2800 cm^{-1} spectral region. As the Al-OH···NCH and the Al-O···HCN species are depopulated by heating to 290 K, the ν(C-H) mode at ~ 3300 cm^{-1} decreases only slightly in absorbance, indicating that Al^{3+}···NCH species remain on the surface up to 290 K.

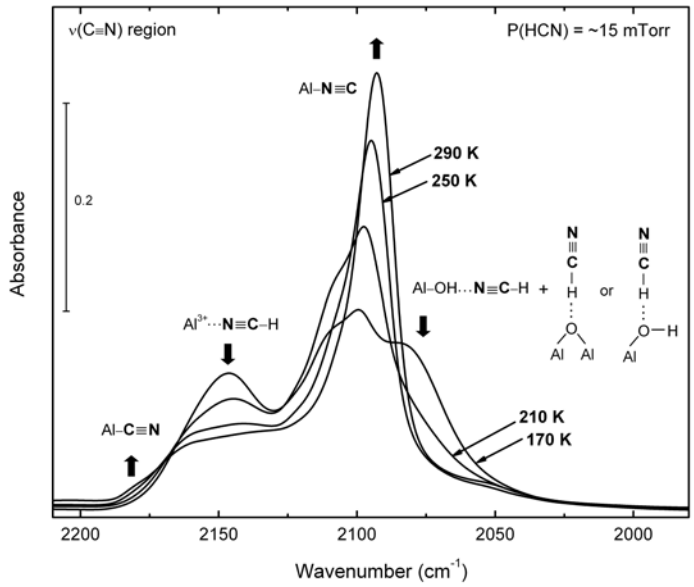

Figure V-2. FTIR spectra for HCN adsorption on Al_2O_3 at 170 K followed by sequential heating to 290 K at an HCN equilibrium pressure of ~15 mTorr.

The spectra in the ν(C≡N) vibrational region are shown in Figure V-2 for heating in the range 170 K – 290 K. Because of the diversity of the HCN binding structures, at least four overlapping ν(C≡N) absorption bands appear at 170 K. Upon heating in the temperature interval 170 K – 290 K, two ν(C≡N) features intensify at ~ 2179 cm^{-1}(weak) and at ~ 2100 cm^{-1} (strong). During heating the other ν(C≡N) modes at ~ 2147 cm^{-1} and ~ 2079 cm^{-1} decrease at different rates. At 290 K, the mode at ~ 2147 cm^{-1} is still visible while the mode at 2079 cm^{-1} is no longer visible. The prominent growth of intensity of the ~ 2100 cm^{-1} mode upon heating is attributed to HCN decomposition on the surface, producing Al-NC species.

In the same manner the spectra of the adsorbed $D^{13}CN$ on γ-Al_2O_3 are shown in Figure V-3 and V-4. Spectral features due to Al-OH species hydrogen bonded to $N\equiv{}^{13}CD$ are observed, as in Figure V-1, but are not shown here.

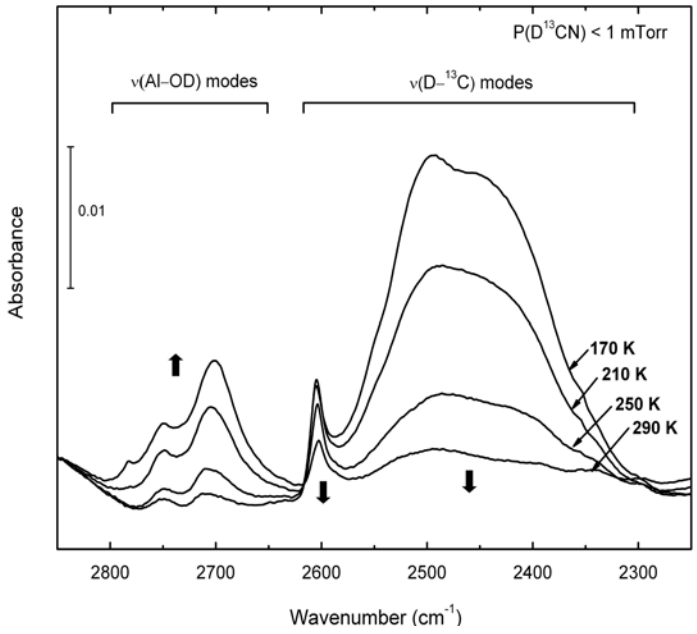

Figure V-3. FTIR spectra for $D^{13}CN$ adsorption on Al_2O_3 at 170 K followed by sequential heating to 290 K at a $D^{13}CN$ equilibrium pressure of < 1 mTorr.

The observation of the formation of isolated Al-OD modes[42,74] from $D^{13}CN$ adsorption indicates that the ^{13}C-D bond breaks upon adsorption, leading to ^{13}CN species formation (as will be shown in Figure V-4). In addition various $\nu(^{13}C\text{-}D)$ modes are observed to form which are analogous to the ν(C-H) modes shown and assigned in Figure V-1. The higher relative intensity of the broad band in the 2600 cm^{-1} – 2300 cm^{-1} region is due to associated Al-OD species whose absorbance underlies the $\nu(^{13}C\text{-}D)$ region. The analogous associated Al-OH modes do not overlap the ν(C-H) modes in Figure V-1. In addition a broadening of the shoulder is observed in the $\nu(^{13}C{\equiv}N)$ region (< 1900 cm^{-1}), indicating the additional $D^{13}CN$ species bound to Al-OD groups (as will be shown in Figure V-4).

By using double labeling in $D^{13}CN$ we are able to separate ν(C≡N) modes for $D^{13}CN$ surface species and for ^{13}CN surface species. The mode for non-dissociated $D^{13}CN$ species will

be lower in frequency than the modes for chemisorbed ^{13}CN species. This allows us to separate the overlapping of HCN- and CN- derived modes which are present in Figure V-2.

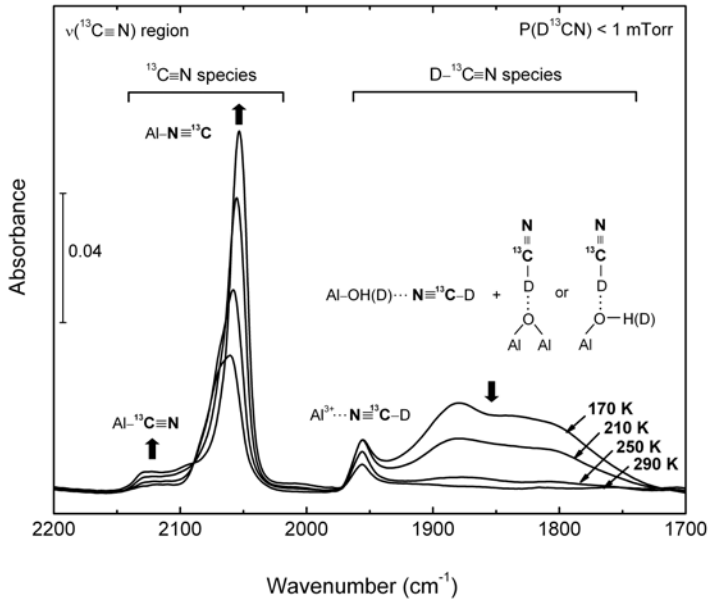

Figure V-4. FTIR spectra for $D^{13}CN$ adsorption on Al_2O_3 at 170 K followed by sequential heating to 290 K at a $D^{13}CN$ equilibrium pressure of < 1 mTorr.

As shown in Figure V-4, these two types of species are separated spectroscopically. Upon heating from 170 K to 290 K, Al-N≡^{13}C and Al-^{13}C≡N species are observed to develop together as $D^{13}CN$ thermally dissociates. The various surface species derived from undissociated $D^{13}CN$ are displayed at lower frequencies. It may be seen from comparing data in Figures V-4 with V-2 that the thermal decomposition of the hydrogen cyanide molecule is clearly witnessed without spectral overlap in the wavenumber region below ~ 1975 cm^{-1}. A comparison of the frequencies and isotopic shifts for HCN- and DCN-derived surface species is given in Table 5, along with comparisons to the literature.

Table 5. The Isotope Shifts of ν(C≡N) Modes and their Assignments (in units of cm^{-1})

HCN(g)	Isotopomer	Isotope shifts		Assignments		
2097[a]	1911[a] ($D^{13}CN$)(g)		-186	Gas Phase		
	2063[a] ($H^{13}CN$)(g)	-34				
HCN /Al_2O_3[b]	$D^{13}CN$ /Al_2O_3[b]				HCN /TiO_2[c]	HCN /SiO_2[c]
2179	2129	-50		Al-CN (M-CN)[d]	2195	2213
2165						
2147	1956		-191	HCN on Lewis acid sites		
2110	2070	-40		Al-NC (M-NC)[d]	2147	2159
2100	2060	-40				
				(HCN on Brønsted acid sites)[d]	2096	2105
~ 2079	~1882		-197	HCN on Brønsted acid sites & Lewis base sites		

[a] The frequencies are from this work and ref. [123]. [b] See the spectra in Figures V-2 and V-4.
[c, d] The frequencies in last column and their assignments in parentheses are from ref. [117].

Figure V-5 shows the IR spectra for the HCN adsorption at 170 K in the ν(C=N) vibrational region upon increasing the equilibrium pressure of HCN. In addition to the various ν(C≡N) modes in Figure V-2, a spectral feature is observed at ~ 1698 cm^{-1} upon HCN exposure indicating η^2(C, N)-HCN bonding on γ-Al_2O_3. The η^2(C, N)-HCN and Al^{3+}···NCH species are depopulated by heating to 400 K, and the dissociatively adsorbed species (Al-CN and Al-NC) still remain on γ-Al_2O_3 (not shown here).

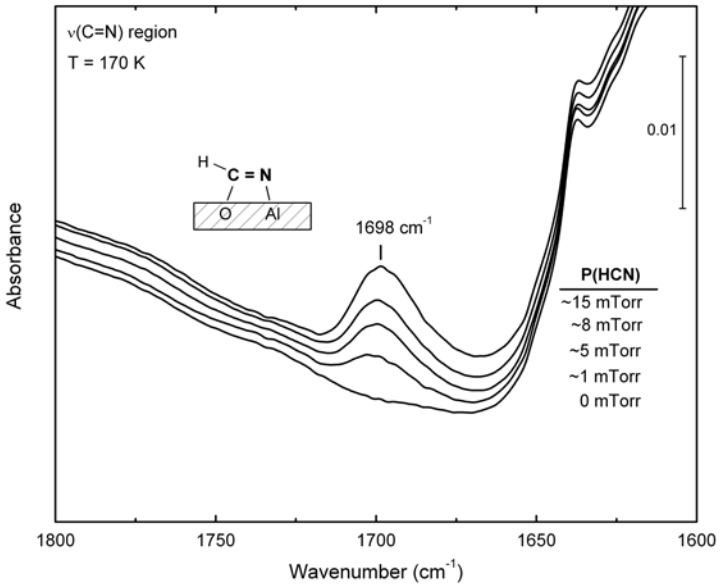

Figure V-5. FTIR spectra for HCN adsorption on Al_2O_3 at 170 K upon raising the HCN equilibrium pressure.

In summary, for HCN adsorption on γ-Al_2O_3, we find that HCN binds to Al-OH groups and to Al-*O*-Al Lewis base centers, as well as to Al^{3+} centers. Thermal dissociation occurs in the range 170 K – 290 K producing Al^{3+}-NC and Al^{3+}-CN species, and deuterium ions generated from D-^{13}CN(a) decomposition react (or exchange with Al-OH groups) to produce Al-OD groups. In addition η^2(C, N)-CN bonding occurs as evidenced by the ~ 1698 cm^{-1} mode in the C=N double bond vibrational region.

V.4.B HCN Adsorption on TEDA-precovered γ-Al_2O_3 Surfaces

In Figure V-6, HCN was adsorbed on top of a TEDA-functionalized γ-Al_2O_3 surface.

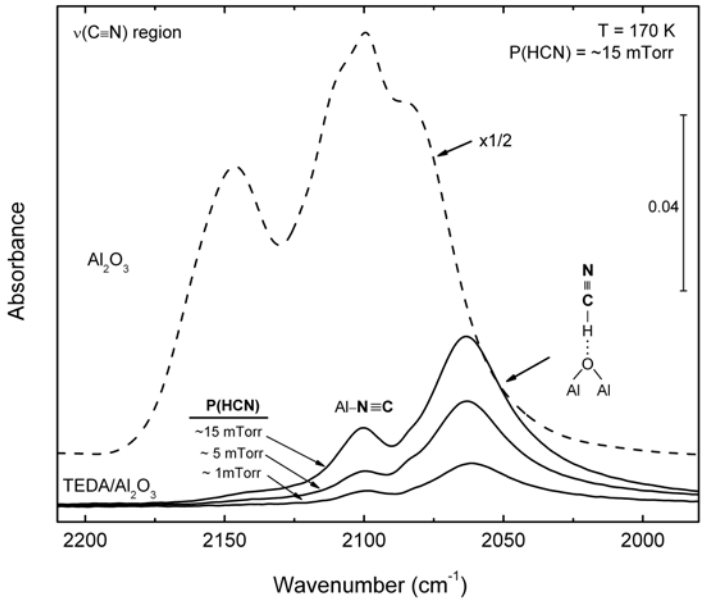

Figure V-6. FTIR spectra of the HCN adsorption on the TEDA-precovered Al_2O_3 surface at 170 K with increasing HCN exposure at P = ~ 1.0, ~5.0, and ~ 15 mTorr, compared to HCN adsorption on the clean Al_2O_3 surface at 15 mTorr (dashed line) from Figure V-2. In order to remove the TEDA background in this region, the spectrum taken before admitting HCN (P(HCN) = 0) is subtracted from the spectra following HCN adsorption on the TEDA-precovered surfaces.

Spectra in the ν(C≡N) region are chosen for display. The dashed spectrum shows the spectrum for HCN adsorption on to pure γ-Al_2O_3 at 170 K (reproduced from Figure V-2) and includes two or more bonding structures of HCN. The comparison shows that TEDA effectively competes for various HCN adsorption sites causing the integrated ν(C≡N) spectra to be reduced to 1/7th the value obtained in the absence of pre-adsorbed TEDA. Upon heating above 170 K the growth of Al-NC species (~ 2100 cm^{-1}) is also observed (not shown), just as seen for the clean γ-Al_2O_3 (in Figure V-2). The loss of Al_2O···HC≡N and Al^{3+}···N≡CH species accompanies the HCN dissociation at T > 170 K (not shown).

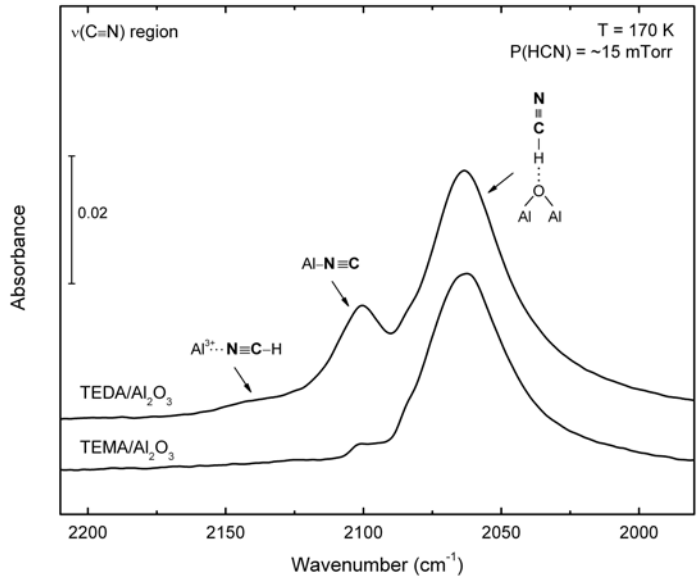

Figure V-7. FTIR spectra for HCN adsorption on the TEDA, and TEMA-precovered Al_2O_3 surface at 170 K with an HCN equilibrium pressure of ~ 15 mTorr. The spectrum taken before admitting HCN (P(HCN) = 0) is subtracted from the spectra following HCN adsorption on the TEDA (TEMA)-precovered surfaces.

Figure V-7 displays a comparison of HCN adsorption on TEDA and TEMA-precovered γ-Al_2O_3 surfaces. The purpose of our study of TEMA is to remove the outer N atoms of the amine functionalized surface to check for any influence of the outer N functionality on HCN adsorption. The two spectra of Figure V-7 show that no significant ν(C≡N) spectral differences are seen for HCN adsorption on TEDA and TEMA-functionalized γ-Al_2O_3 surfaces. The TEMA coverage is slightly higher than the TEDA coverage in this comparison. Thus the outer amine group is not involved in bonding HCN to TEDA-functionalized γ-Al_2O_3 and *only site blocking effects by TEDA and TEMA are observed*.

Another spectroscopic evaluation of the interaction of TEDA and HCN can be made by carefully looking for changes in the IR spectra of TEDA during adsorption of HCN. This is seen in Figure V-8, where two spectral regions, ν(C-H) and δ(C-N) for TEDA, are shown as the coverage of HCN is increased at 170 K. No spectral shift in the TEDA vibrational modes is

observed for both frequency regions. Shifts, particularly in the δ(C-N) mode, have previously been shown to occur upon chemical interaction with the nitrogen atoms of TEDA molecules.[81] These results, coupled with others shown above, indicate that adsorbed TEDA molecules on γ-Al_2O_3 do not undergo chemical interactions with adsorbed HCN species.

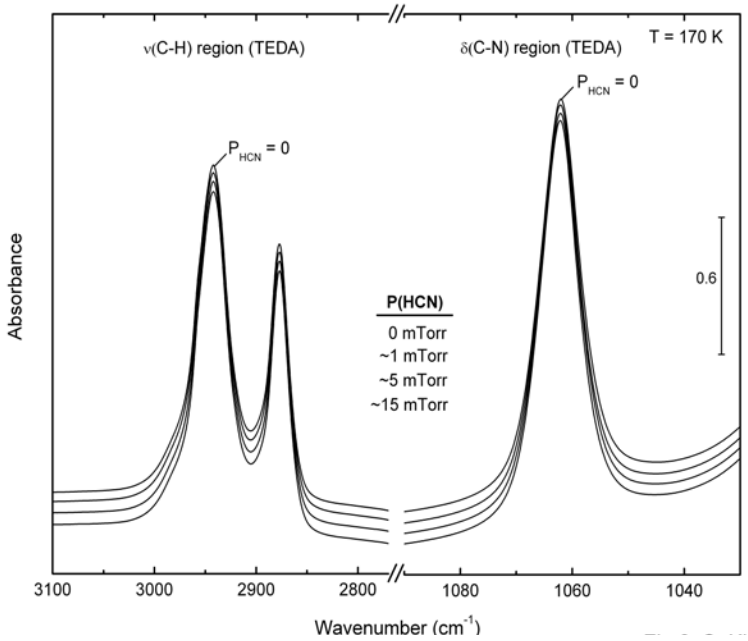

Figure V-8. FTIR spectra of the TEDA/ Al_2O_3 surface in the ν(C-H) and δ(C-N) frequency regions upon HCN adsorption, showing the lack of an HCN effect on the spectra of adsorbed TEDA.

V.5 Results: Theoretical Studies

V.5.A HCN and CN Adsorption on (100) and (110) Surfaces of γ-Al_2O_3

The adsorption properties of HCN molecules on the γ-Al_2O_3 surface were investigated for the case of (100) and (110) surface orientations using the slab models described in Section V-3B. The corresponding adsorption energies calculated throughout this work were obtained based on the expression

$$E_{ads} = E_{molec} + E_{slab} - E_{(molec+slab)} \qquad \text{(V-1)}$$

where E_{molec} is the energy of the isolated adsorbate molecule in its equilibrium position, E_{slab} is

the total energy of the slab and $E_{(molec+slab)}$ is the total energy of the adsorbate/slab system. The only exception from the above definition was considered in the case when HCN adsorption is mediated by OH groups. In this case E_{slab} energy was taken as the total energy for the slab with the adsorbed OH group. A positive E_{ads} as determined based on Eq. (V-1) corresponds to a stable adsorbate/slab system. The energy of the isolated adsorbate molecule was determined from calculations performed on a single molecule in a cubic cell of length 12 Å. The same Brillouin-zone sampling has been used to calculate the energies of the bare slab and of the molecule-slab systems. The corresponding results corresponding to adsorption of HCN on (100) and (110) surfaces are given in Table 6 while representative configurations are depicted in Figures V-9 (a)-(g).

Table 6. Calculated Equilibrium Distances, Adsorption Energies and Vibrational Frequencies for HCN, CN+H and NC+H Adsorbed on (100) and (110) Surfaces of the γ- Al_2O_3 Surface.[a]

System/ Surface	Site	d(Al…X)[b]	d(O...Y)/[c] d(H...N)	d(N-C)	d(C-H)	E_{ads}	ν(C-H)	ν(N-C)
a) Al...NCH Adsorption								
(100)	Al_V(II)	2.130		1.149	1.069	7.4	3398	2169
	Al_V(I)	2.166		1.150	1.070	8.0	3387	2155
	Al_V(III)	2.079		1.148	1.070	12.7	3393	2173
(110)	Al_{III}(I)	1.985		1.145	1.071	27.5	3386	2201
	Al_{IV}(II)	2.045		1.148	1.069	13.7	3402	2175
	Al_{IV}(III)	2.152		1.150	1.071	7.2	3385	2166
b) η^2(C,N)-HCN Adsorption								
(110)	Al_{III}(I), μ_3-O	1.880	1.469	1.250	1.091	17.6	3104	1634
	Al_{IV}(II), μ_2-O	1.881	1.451	1.250	1.093	11.8	3078	1652
	Al_{IV}(III),μ_3-O	1.839	1.443	1.424	1.097	9.6	3029	1710
c) O...HCN Adsorption								
(100)	μ_3-O		2.093	1.157	1.083	2.1	3193	2088
	μ_3-O		2.277	1.158	1.077	2.6	3285	2094
(110)	μ_2-O		1.968	1.158	1.086	5.3	3153	2084
	μ_3-O		1.995	1.157	1.084	2.2	3177	2090

(Table 6, Continued)

d) OH...NCH Adsorption								
(100)	μ_1-Al_V(I)		2.097	1.154	1.070	3.1	3380	2124
	μ_1-Al_V(II)		1.970	1.154	1.070	5.0	3384	2126
	μ_1-Al_V(III)		1.916	1.154	1.070	4.9	3386	2128
(110)	μ_1-Al_{III}(I)		1.975	1.154	1.070	4.4	3383	2119
	μ_1-Al_{IV}(III)		1.903	1.154	1.070	5.8	3375	2127
	μ_2-Al_{IV}(III)		1.935	1.154	1.070	5.2	3383	2119
e) Al...CN + OH								
(100)	Al_V(II)	1.997		1.168				2175
	Al_V(I)	1.971		1.167				2188
	Al_v(III)	1.981		1.168				2173
(110)	Al_{III}(I)	1.952		1.166				2190
	Al_{IV}(II)	1.967		1.168				2179
	Al_{IV}(III)	1.965		1.167				2179
f) Al...NC + OH								
(100)	Al_V(II)	1.882		1.179				2087
	Al_V(I)	1.857		1.181				2084
	Al_v(III)	1.876		1.180				2083
(110)	Al_{III}(I)	1.831		1.181				2079
	Al_{IV}(III)	1.850		1.180				2086
g) Al..CN..Al + OH								
(100)	Al_V(III), Al_V(I)	2.088[d]		1.178				2077
		2.162						
(110)	Al_{III}(I), Al_{IV}(II)[e]	2.079		1.174				2118
		2.074						
	Al_{III}(I), Al_{IV}(II)[f]	2.005		1.169				2150
		2.046						

[a] Bond distances are given in Angstroms, adsorption energies in kcal/mol and vibrational frequencies in cm^{-1}. [b] X stands for N in the case of NCH or NC adsorption with the N atom towards the surface, and for C in the case of CN adsorption with the C atom towards the surface. [c] The bond distance d(O…Y) is considered in the case of NCH adsorption to a surface O atom through the N end, or to a C atom for NCH adsorption in a η_2 configuration d(H…N) is considered in the case of OH…NCH adsorption. [d] For the Al..CN..Al configurations the first bond corresponds to the Al…N distance while the second to the Al…C distance. [e] Configuration with a H atom at a short separation (~ 2.1 Å) from NC. [f] Configuration with the H atom at a large separation (~ 3.7 Å) from NC.

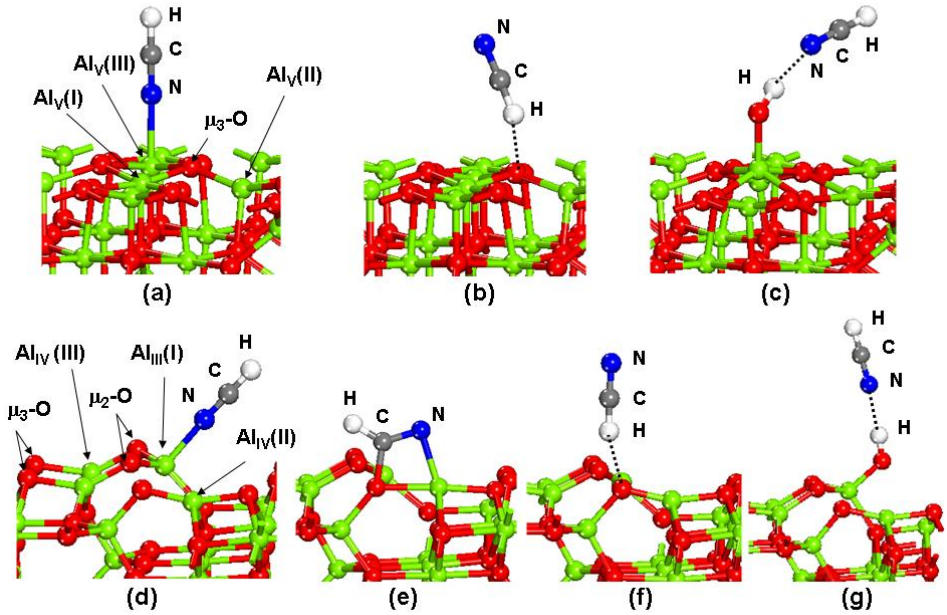

Figure V-9. Representative configurations of the HCN molecule adsorbed on (100) (panels a)-c)) and (110) (panels d)-g)) γ- Al_2O_3 surfaces. Possible bonding configurations of the HCN molecule as Al…NCH (panels a) and d)), O…HCN (panels b) and f) or OH…NCH (panels c) and g)) are illustrated. In the case of the (110) surface, panel e) illustrates the η^2(C,N)-HCN bonding type.

As can be seen from data presented in Figure V-9 and Table 6 several bonding types of HCN molecule to the surface can take place. The main bonding mechanism is seen for the case of HCN adsorption at unsaturated Al sites with the N end of the molecule oriented toward the surface. On the (100) surface the calculated binding energies were found to range between 7.4 – 12.7 kcal/mol while on the (110) surface the binding energies increase up to 27.5 kcal/mol. The corresponding Al…N separations range between 2.166-1.985 Å. The largest adsorption energy is seen in the case of (110) surface when the molecule adsorbs at the highly unsaturated Al_{III}(I) site (see Figure V-9 (d)) on the (110) surface. On the (100) surface the calculated C-N vibrational frequencies of the HCN molecule range from 2155 – 2169 cm^{-1} while on the (110)

surface the corresponding vibrational frequencies are blue shifted in the range 2166 – 2201 cm^{-1} consistent to the larger binding energies observed on this surface.

A second set of HCN adsorption configurations identified correspond to η^2(C, N)-HCN species where both C and N atoms are simultaneously bonded to a pair of nearby Al and O surface sites. Such bonding configurations are possible on both (100) and (110) surfaces but only those on the later surface were found to be stable with respect to the energy of the isolated HCN molecule and of the slab surface. As a result, in Table 6 we provide only the data corresponding to η^2(C, N)-HCN configurations on the (110) surface (see also Figures V-9(e)). For these configurations we found that the corresponding C-N bonds are elongated on average by 0.1 Å relative to the standing up states indicating a softening of these bonds. Consistent to these changes the corresponding C-N vibrational frequencies are red shifted into the range 1634 – 1710 cm^{-1}.

The third category of bonding configurations of HCN molecules, denoted O··HCN in Table 6, correspond to hydrogen bonding to surface O atoms through the H end of the molecule (see also Figures V-9(b),V-9(f)). In these cases the binding energies were found to be smaller than in previous cases with values in the range 2.2 – 5.3 kcal/mol. Additionally, only small shifts relative to the gas phase values of C-N vibrational modes are seen with values in the range 2084 – 2094 cm^{-1}.

Finally, we have analyzed the possibility of HCN molecules adsorbing at Al-OH Brønsted acid sites (see configurations in Figure V-9(c), V-9(g)) and data in Table 6(d). Our calculations in this case were restricted to the case of small coverages of OH species as this is expected to be the case for a surface annealed up to 1000 K in high vacuum conditions as was done in the current study. We found that the HCN molecule can adsorb on hydroxyl groups by

formation of O-H···N hydrogen bonds with lengths in the range 1.903-2.097 Å (see Table 6(d)). For this type of bonding there is only a small dependence on either the surface orientation or the surface site as reflected by the narrow range of variation in binding energies, i.e. 3.1 – 5.8 kcal/mol.

Beside the molecular adsorption of HCN species on the γ-Al_2O_3 surface we have further expanded our analysis to the case of dissociated species with the formation of adsorbed CN and H species. The main purpose of this analysis was to estimate the corresponding range of C-N vibrational frequencies for various configurations adsorbed on the surface. No attempt was made to map the potential energy surface for dissociation of HCN species on the γ-alumina surface leading to formation of either Al···CN or Al···NC species.

Specifically, CN species were considered to adsorb at unsaturated Al sites while the dissociated H atom binds to a surface O site, forming an OH group (see Figure V-10). For CN radicals adsorption with C (see Figures V-10(a), V-10(d)), and N moieties (see Figures V-10(b), V-10(e)) oriented towards the surface were analyzed. As the dissociated H atoms can also interact with the adsorbed CN species in a manner which is dependent on the relative separations, a large number of configurations are possible.

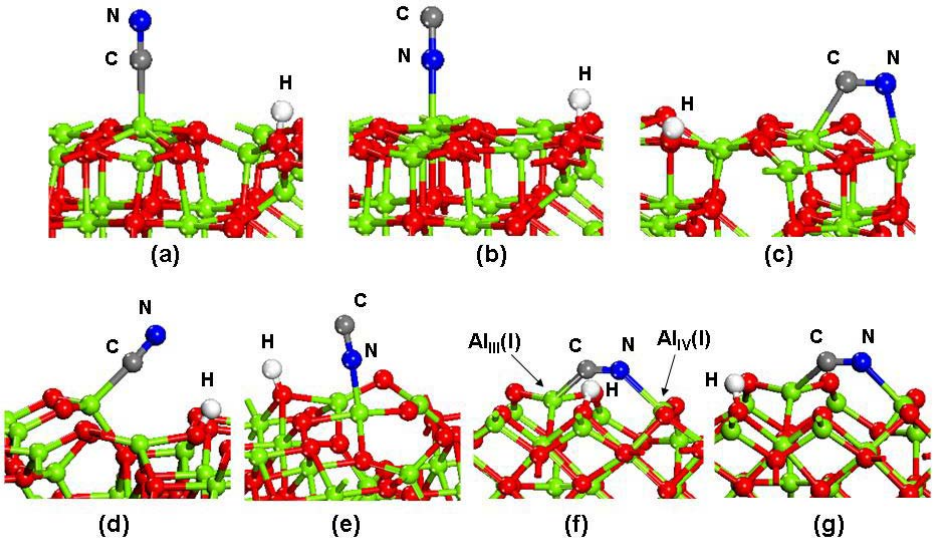

Figure V-10. Representative configurations of the CN radical adsorbed on (100) (panels a) - c)) and (110) (panels d)- f)) γ- Al_2O_3 surfaces. Bonding through the C end (panels a) and d)), the N end (panels b) and e)) or through a bridge configuration (panels c), f) and g)) are illustrated. Panels f) and g) illustrate the case when the dissociated H atom binds at two different surface O sites near (~2.1 Å), and further away (~3.7 Å) from the CN species. In the case of panels c), f) and g) the slab orientation is rotated 90° relative to the other panels in order to allow a clearer view of the bridge CN species.

In our analysis here we limit ourselves to the case when the H atom is separated by the largest distance allowed by our slab model from the bonding site of C or N moieties. Beside the vertical configurations we have also identified states in which the dissociated CN species are lying down on the surface, with simultaneous bonding at both ends to Al surface sites. Such configurations are indicated in panels (c) and (f) of Figure V-10 while corresponding results are given in Table 6(g).

On the based of the data given in Table 6(e) it can be seen that in the case of Al···CN bonding, the range of C-N vibrational frequencies is 2175 – 2188 cm^{-1} on the (100) surface, and 2179 – 2190 cm^{-1} on the (110) surface. Alternatively, in the case of Al···NC bonding, the C-N vibrational frequencies (see Table 6(f)) range from 2083 – 2087 cm^{-1} on the (100) surface while a range of 2079 – 2086 cm^{-1} was determined on the (110) surface (see Table 6(f)).

Finally, in the case of the lying down configurations Al···NC···Al, a significant frequency shift relative to gas phase values is observed, particularly in the case of the (110) surface. In this case the bonding to the surface involves the unsaturated Al_{III}(I) and Al_{IV}(II) sites (see Figure V-10(f)). For this configuration we exemplify the effect of frequency shift when the H atom is moved away from the CN molecule. Specifically, in the case when the H atom is placed at a short distance (see Figure V-10(f)), the CN vibrational frequency is 2118 cm^{-1}. By increasing the separation among H and CN species (see Figure V-10g) the frequency is further shifted to higher values of 2150 cm^{-1} with a corresponding shortening of the CN bond from 1.176 Å to 1.169 Å

The ensemble of data presented in this section indicates a complex infrared spectral signature of HCN molecules when adsorbed on the γ-Al_2O_3 surface due to several factors. Among these we have analyzed here the influence of different bonding configurations such as molecular bonding at Al^{3+} Lewis acid sites or at Al-OH Brønsted acid sites, at Lewis base O sites with O···HCN hydrogen bond formation, or at mixed Al and O sites through an η^2(C, N) configuration. We noted important variations among the (100) and (110) surface orientations particularly due to the presence of different unsaturated Al sites. Furthermore, beside the molecular species, dissociated CN+H species can be also present on the surface. We have shown that orientations of CN species with either the C or N ends toward the surface, or simultaneous bonding at both C and N ends, as well as the presence of a dissociated H atom with OH formation at a nearby site, can lead to variations in the C-N vibrational frequencies. The complexity of the experimental IR spectrum of HCN molecules on γ-Al_2O_3 is a reflection of superposition of all these contributions.

V.6 Discussion

V.6.A HCN Adsorption on Clean γ-Al_2O_3 Surfaces

Even though it has been observed that doped aluminum ions on oxide surfaces act as catalytic sites on the surface reaction of HCN molecules causing dissociation and polymerization,[114] there is a lack of studies of HCN adsorption on the γ-Al_2O_3 surface itself. Because of the different binding sites on γ-Al_2O_3 surfaces, several configurations for HCN molecular adsorption can occur: (a) Al^{3+}···NCH (Lewis acid sites); (b) Al-O*H* ···NCH (Brønsted acid sites); (c) Al-*O*-Al(or H)···HCN (Lewis base sites). These molecular adsorbed species have C-H (C-D) stretching vibrational modes shown in Figure V-1 and V-3. The isotope shift of C-H stretching mode by deuterium and ^{13}C labeling is -720 cm^{-1}, which is obtained from the difference of ν(C-H) mode frequency between HCN and D^{13}CN in the gas phase.[123] The vibrational modes at ~ 2604 cm^{-1} (sharp) and at 2600 cm^{-1} – 2300 cm^{-1} (broad) upon D^{13}CN exposure (see Figure V-3) correlate with the modes at ~ 3300 cm^{-1} (sharp) and 3300 cm^{-1} – 2800 cm^{-1} (broad) upon HCN adsorption (see Figure V-1) respectively, showing the same behavior. Frequency shifts in each case (sharp and broad) are observed to be about -700 cm^{-1}. Thus the abnormally broad band at 3300 cm^{-1} – 2800 cm^{-1} as well as the sharp peak at ~ 3300 cm^{-1} in HCN adsorption can be confirmed as ν(C-H) modes. The C≡N stretching modes in molecular adsorption are highly isotopically shifted in D^{13}CN from ~ 2097 cm^{-1} for HCN to ~ 1911 cm^{-1} for D^{13}CN (see Figure V-4). This highly negative shift (-Δν = 191 – 197 cm^{-1}) is the result of a deuterium isotope effect as well. Only thermal depletion is observed in these molecularly adsorbed species. It is shown that HCN binding to Lewis acid sites (Al^{3+}···NCH) is relatively strong compared to Brønsted acid sites (Al-O*H*···NCH) and Lewis base sites (Al-*O*-Al···HCN).

The ν(C≡N) frequency of adsorbed HCN molecules at Brønsted acid sites (Al-O*H*···NCH) can not be separated from other species.

The existence of dissociative adsorption of HCN is proved by the separation of Al-CN (Al-NC) species from adsorbed HCN molecular species in the ν(^{13}C≡N) spectral region. Compared to the isotope shifts of D^{13}CN species (-Δν = 191 – 197 cm^{-1}), the isotope shifts of dissociated ^{13}CN species are smaller (-Δν = 40 – 50 cm^{-1}) for the ν(^{13}C≡N) mode. Since the Al-^{13}CN would be more affected by ^{13}C isotope labeling,[116] we can separate Al-^{13}CN from Al-N^{13}C species based on the isotopic shifts. Thus the prominent ^{13}C-labeled species at ~ 2060 cm^{-1} shifts to ~ 2100 cm^{-1} for ^{12}C-labeled species and is assigned to Al-N^{13}C; the ^{13}C-labeled species at ~ 2129 cm^{-1} shifts to ~ 2179 cm^{-1} for the ^{12}C-labeled species and is assigned to Al-^{13}CN, as shown Table 5. A -51 cm^{-1} isotope shift for Si-^{13}CN and a -39 cm^{-1} shift for Si-N^{13}C were observed by changing from ^{12}C to ^{13}C,[116] which is consistent with our results. These dissociation reactions accompany the development of isolated Al-OH (Al-OD) surface species, as seen in Figure V-3.

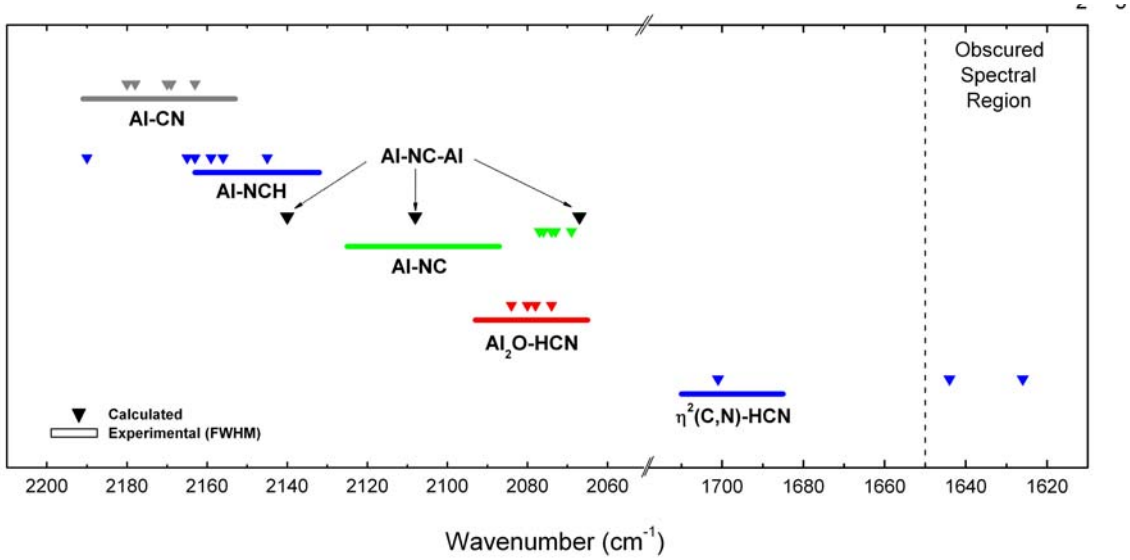

Figure V-11. Correlation between experimental and computed vibrational frequencies of HCN and CN species adsorbed on Al_2O_3 surfaces. Solid lines indicate FWHM of the ν(C≡N) and ν(C=N) band in each binding configuration which are measured from the curve-fitted FTIR spectra (Figure V-2 and V-5). Triangle symbols are from the computational results given in Table 6. The theoretical values were divided by a

correction factor, 1.004768 = 2107 cm^{-1} /2097 cm^{-1} (= ratio between theoretical and experimental ν(C≡N) frequency values for gas phase HCN).

Based on these assignments, these experimental results are correlated with the theoretical values as shown in Figure V-11. The solid lines indicate the FWHM of the ν(C≡N) and ν(C=N) modes in each bonding configuration which is obtained from the curve-fitted FTIR spectra (Figure V-2 and V-5). The symbols are from the computed values in Table 6. In most cases excellent agreement is obtained. The theoretical frequency values of ν(C≡N) in the Al-NC geometry deviate slightly from the experimental range. In addition, one of the Al-NC-Al configurations exhibits its theoretical ν(C≡N) frequency in the middle of the experimental range. Therefore the contribution of bridged forms of CN has been postulated. In the case of HCN adsorption on the highly unsaturated Al_{III}(I) site on the (110) surface bound with the N end of the molecule, the theoretical vibrational frequency (~ 2201 cm^{-1}) occurs far away from the corresponding experimental observation. Since the Al_{III}(I) site on the (110) surface is considered as the most reactive site on γ-Al_2O_3 surfaces, HCN molecules might not remain undissociated on this site.

However in the ν(C-H) region the highly red-shifted ν(C-H) frequency in the Al_2O···HCN configuration is also calculated to be in the range of 3150 cm^{-1} – 3200 cm^{-1} (compared to calculated ν(C-H) frequency, 3382 cm^{-1}, in gas phase) just as observed in the experiments. The ν(C-H) mode would be expected to be highly perturbed in this hydrogen-atom bound configuration.

Here, two possible mechanisms for the surface dissociative adsorption of HCN can be proposed. The first one requires that the C-H bond in Al^{3+}···NC-H species (on Lewis acid sites) is cleaved, and then the hydrogen atom is flipped to a nearby oxygen atom (Al-*O*-Al) to produce an

Al-OH group. The second mechanism requires that the C-H bond of Al_2-O···H-CN species (on Lewis base sites) is broken producing the Al-OH group, followed by CN adsorption on an aluminum ion site. In both cases, the aluminum ion (Al^{3+}) sites are of importance. On a highly hydroxylated surface which is generated by the adsorption of large amounts of H_2O, where the aluminum ion sites are more fully coordinated, the Al-NC (Al-CN) as well as Al^{3+}···NCH species are not observed (data not shown here). This shows that the aluminum ion (Al^{3+}) sites are the centers for the surface dissociative reaction of HCN.

A major finding in the present work is the observation of the η^2(C, N)-HCN bonding on the γ-Al_2O_3 surface. The η^2(C, N) configuration of nitrile groups on a surface, where both C and N atoms are simultaneously bonded to surface sites, was first proposed for acetonitrile adsorption on the Pt(111) surface.[124] Acetonitrile molecules form a saturated monolayer by η^2(C, N)-CH_3CN bonding. The ν(C≡N) frequency at ~ 2270 cm^{-1} observed in the multilayer disappears, and then a new feature at ~ 1615 cm^{-1} appears in ν(C=N) frequency region after annealing at 180 K. For the Al_2O_3 surface, the η^2(C, N)-CH_3CN adsorbed species is also observed by others at 1611 cm^{-1}.[125]

In the η^2(C, N)-HCN adsorbed configuration observed in this study, the CN stretching vibrational mode is also found at a much lower frequency (~ 1698 cm^{-1}, see Figure V-5) than that of end-on adsorbed HCN species (~ 2200 – ~ 2000 cm^{-1}, see Figure V-2). The ~ 1698 cm^{-1} mode is in the C=N double bonding region. The C≡N triple bond in the nitrile group converts to a C=N double bond by η^2 bonding. The observed ν(C=N) frequency in the η^2(C, N)-HCN species also matches the calculated values (1634 – 1710 cm^{-1}, see Table 6. b) and Figure V-11). The thermal stability of η^2(C, N)-HCN species on the γ-Al_2O_3 surface is observed to be similar to the end-on adsorbed HCN on Lewis acid sites (Al^{3+}···NCH).

V.6.B HCN Adsorption on TEDA-precovered γ-Al_2O_3 Surfaces

Because Brønsted acid sites and Lewis acid sites are occupied by pre-adsorbed TEDA (TEMA) on γ-Al_2O_3 surfaces,[81,91] most of the ν(C≡N) modes formed on clean Al_2O_3 surfaces are absent on TEDA(TEMA)-functionalized γ-Al_2O_3 surface as seen in Figure V-6 and V-7. Only a minor spectral difference is found for HCN adsorption comparing TEDA- and TEMA-precovered surfaces in Figure V-6 and V-7. The small difference due to the different coverages of pre-adsorbed TEDA and TEMA as has been demonstrated in separate experiments (not shown here). The results of Figure V-7 and Figure V-8 indicate that no chemical interaction between adsorbed TEDA species and HCN occurs. The HCN species adsorbed on Lewis base sites (Al-*O*-Al) are also unaffected by TEDA.

In this work, it is shown that the presence of the exposed amine functionality of the adsorbed TEDA molecules for HCN adsorption is not important. Unlike silicate and charcoal supports, the alumina surface itself contains Al^{3+} ion sites where the HCN molecules are active. Therefore TEDA only competes with HCN for these sites on γ-Al_2O_3. The function of the TEDA molecules, employed with cations such as Cu^{2+}, Zn^{2+}, and Cr^{6+}, for HCN adsorption is to bind the cations by forming complexes with them. Such anchored cations then bind HCN. The effect of these anchored cations is therefore more important than TEDA molecules in causing HCN capture by the surface.

V.7 Summary

The adsorption of HCN on the γ-Al_2O_3 surface has been studied using transmission FTIR spectroscopy. It is demonstrated that the HCN molecule binds to Brønsted acid sites (Al-O*H*···NCH), Lewis acid sites (*Al*$^{3+}$···NCH), and Lewis base sites Al-*O*-Al(or H)···HCN on the γ-Al_2O_3 surface. In addition to molecular binding, HCN dissociative adsorption also occurs at 170

K, and it is enhanced by heating to 290 K. It is shown that aluminum ion (Al^{3+}) sites are centers for the surface dissociative reaction in which the H-CN bond is broken. In addition, η^2(C, N)-HCN bonding is also observed with a ν(CN) frequency at ~ 1698 cm^{-1}, indicating the shift from a C≡N triple bond to a C=N double bond by the η^2 bonding of the nitrile group on γ-Al_2O_3.

No direct binding of HCN to the exposed amine group on TEDA pre-adsorbed on γ-Al_2O_3 is found. Instead the TEDA molecule effectively competes with HCN for binding sites on the γ-Al_2O_3 surface. The observed ν(C≡N) mode on a TEDA-precovered surface is due to the HCN adsorption on Lewis base sites (Al-*O*-Al) where TEDA does not bind.

V.8 Acknowledgement

We acknowledge with thanks the support of this work by The Army Research Office, and discussion with Dr. Alex Balboa of Aberdeen Proving Ground. A grant of computer time at the Army Research Laboratory is also gratefully acknowledged.

VI. Infrared Spectroscopic Study of ClCN Adsorption on Clean and TEDA-precovered γ-Al_2O_3*

VI.1 Abstract

The effect of triethylenediamine (TEDA) (also called 1, 4-diazabicyclo [2.2.2]octane, DABCO) on the adsorption of ClCN, on a γ-Al_2O_3 absorbent has been investigated. Both FTIR and theoretical studies indicate that no direct interaction between amine groups of TEDA and ClCN molecules takes place. Instead, we found that TEDA competes with ClCN for active surface sites on γ-Al_2O_3.

In addition, the adsorption behavior of cyanogen chloride (ClCN) on a clean γ-Al_2O_3 surface has been studied. The sequence of the thermally activated processes of diffusion, adsorption, desorption and decomposition of ClCN molecules on the clean γ-Al_2O_3 surface following ice-like ClCN layer formation at lower temperature was observed. One of the decomposition products, Al-NCO, were assigned by using an Al-^{18}OH labeled surface for reaction with ClCN. In addition, Al-CN and Al_2-OCN species were also detected upon ClCN decomposition. Good correlation of the calculated vibrational frequencies for the adsorbed species with experimental data is found.

VI.2 Introduction

We have investigated the role of triethylenediamine (TEDA) (also called 1,4-diazabicyclo[2.2.2]octane, DABCO) functionalization of γ-Al_2O_3 on the adsorption of cyanogen chloride. In environmental and military applications triethylenediamine (TEDA) has been used as an impregnant in filtration and air-cleaning systems. TEDA is known to remove radio-active gases such as methyl iodide forming a quaternary ammonium salt.[8-11] In the carbon filter, inorganic impregnants such as copper, chromium, silver, zinc, molybdenum, sulfur, manganese, etc. are added to TEDA-functionalized adsorbents to provide additional chemical or catalytic interactions with low boiling toxic vapors and to promote decomposition of such gases into non-toxic deposits or innocuous gases. The amines are known to stabilize the inorganic impregnants shielding the active sites from water adsorption and increasing the shelf life of carbon filters. It was also found that organic amine compounds such as pyridine, picoline, and TEDA are able to reduce the aging effect of carbon filters, which is a characteristic problem under humid conditions.[15-18]

The retention of ClCN was tested in copper, silver, zinc, and molybdenum incorporated carbon filters with varying water content by Deitz.[17,18] As the relative humidity value increased from 0 % to 80 %, the ClCN retained in the filter decreased from 260 mg to 4 mg. In the presence of TEDA, the retained amount of ClCN was restored up to ~ 230 mg, but it did not exceed the value measured under in the dry conditions. Thus amine-impregnated materials show a considerably enhancement for the retention of cyanogen chloride. It has been reported that TEDA itself plays its role on the adsorption of cyanogen chloride directly, in analogy to the reaction with CH_3I, as shown in Figure VI-1.[21-23]

Figure VI- 1. The proposed reaction between TEDA and cyanogen chloride. [21-23]

Therefore, in the present work the role of pre-adsorbed TEDA on the ClCN adsorption properties on a γ-Al_2O_3 surface has been investigated. The adsorption of TEDA on the γ-Al_2O_3 surfaces would be expected to occur in some cases by surface binding to one end of the molecule, leaving the other amine group exposed. Then, the adsorbed TEDA molecule might be able to provide the exposed amine moiety as a bonding site for subsequently adsorbed ClCN forming $(TEDA\text{-}CN)^+$ species as illustrated in Figure VI-1. Spectroscopic evaluation of the interaction of TEDA and ClCN has been made by comparing the IR spectra of ClCN adsorbed on a clean γ-Al_2O_3 surface and on a TEDA-precovered surface.

In addition, the adsorption and decomposition behavior of ClCN on the clean γ-Al_2O_3 surface has been studied in this work. Even though the adsorption of other CN-containing molecules such as HCN, CH_3CN, CH_3NC on oxide surface has a long history,[117,125-130] there is a dearth of detailed studies of ClCN adsorption on surfaces. We report the sequence of the processes of diffusion, adsorption, desorption and decomposition of ClCN molecules, thermally activated on the γ-Al_2O_3 surface, following ice-like ClCN layer formation on the outer geometric surface of a pressed disk of γ-Al_2O_3 at low temperature. The vibrational assignment of ClCN adsorbed on Lewis acid sites (Al^{3+}), Brønsted acid sites (Al-OH) and Lewis base sites (Al-O-Al)

is made, and is correlated with theoretical results. Cyanate (Al_2-OCN), isocyanate (Al-NCO) and cyanide (Al-CN) species are produced at elevated temperature.

VI.3 Experimental and Computational Methods

VI.3.A Experimental

The experimental methods used in this work were described in detail elsewhere.[81] Briefly, a transmission IR cell contains a tungsten grid into which γ-Al_2O_3 powder is pressed by a hydraulic press.[39,40] A type K thermocouple is welded on the upper empty region of the grid. The grid allows the sample to be heated electrically and cooled by a refrigerant in the range of 83 K – 1500 K. The IR cell is connected to a stainless steel vacuum system with a base pressure < 1 x 10^{-8} Torr.

The γ-Al_2O_3 powder was obtained from Guild Associates (surface area = 250 m^2/g). The Al_2O_3 sample was briefly heated to 950 K in vacuum to produce a partially dehydroxylated surface.[39,41,73,74] ClCN gas was obtained commercially and further purified with freeze-pump-thaw cycles using liquid nitrogen. $H_2{}^{18}O$ was obtained from Isotec, Inc. with an isotope purity of 95 atom %. The isotopic conversion of Al-^{16}OH species on the γ-Al_2O_3 surface to Al-^{18}OH was achieved by heating the sample up to 1050 K under a high pressure of $H_2{}^{18}O$.[83] Triethylenediamine (TEDA) was purchased from Aldrich. TEDA vapor was admitted into the IR cell, with the temperature of the alumina sample at 300 K, to form the adsorbed phase of TEDA.[81] After TEDA adsorption, the cell was evacuated by a turbo-molecular pump and then the TEDA-functionalized alumina sample was exposed to ClCN(g) at lower temperature.

The infrared spectra were recorded at each indicated temperature with a Bruker TENSOR 27 FT-IR spectrometer. Each spectrum was obtained by averaging 64 interferograms with 2 cm^{-1} resolution and the background spectrum, taken through the empty grid region, was subtracted.

VI.3.B Computational Method

The computational method used in this work is similar to the one considered by us to describe the coadsorption properties of TEDA-CO[122] and TEDA-HCN[131] systems on the γ-Al_2O_3 surface. Here we will indicate only the essential elements for the current work.

The calculations were performed based on first principles density functional theory with plane-wave basis sets and supercell models as implemented in the Vienna *ab initio* simulation package (VASP).[93-95] The electron-ion interaction has been described by fully non-local optimized ultrasoft pseudopotentials (USPPs) similar to those introduced by Vanderbilt.[96,97] Periodic boundary conditions were used, with the one-electron pseudo-orbitals expanded over a plane-wave basis set with a cutoff energy of 495 eV, corresponding to precision level *high* as detailed in the VASP manual.[98] The sampling of the Brillouin zone was performed using a Monkhorst-Pack scheme[100] and a grid mesh with a k-point separation of 0.05 $Å^{-1}$. For the treatment of exchange and correlation we have used the generalized gradient approximation (GGA) with the Perdew *et al*.[99] (PW91) functional. Hereafter we will name our computational method as US-PW91. In the case of radical species spin polarized calculations have been considered. The majority of calculations done in this study were performed with a vacuum width of 14 Å. However, in the case of coadsorption studies, where ClCN or CN can adsorb on top of a TEDA molecule, the vacuum width has been further increased to 18.5 Å to minimize any interaction across the vacuum with the neighbor slab.

Similar to our previous two studies[122,131] the model used to simulate the surface of γ-Al_2O_3 is the one proposed by Digne et al.[34] Within this model we have analyzed the adsorption properties on both (100) and (110) surfaces which have been shown to be predominant for the

exposed surface.[34] A full description of the slab models used to represent these two surface orientations can be found in our previous work.[122]

Here we only point to the reader the diversity of surface sites present on these surfaces. Specifically, the (100) surface presents five-fold coordinated aluminum atoms (denoted as Al_V) and three-fold coordinated oxygen atoms (denoted as μ_3-O) while the (110) surface presents several types of coordinated Al and O atoms, namely three-fold Al_{III} (I) and four-fold Al_{IV} (II and III) aluminum sites and two-fold μ_2-O and three-fold μ_3-O oxygen atoms.

The adsorption properties of individual molecules and radicals on the γ-Al_2O_3 surface were done using slab models corresponding to (100) and (110) surface orientations. For all the adsorption configurations identified in this work the corresponding binding energies have been determined based on the expression

$$E_{ads} = E_{molec} + E_{slab} - E_{(molec+slab)} \qquad \text{(VII-1)}$$

where E_{molec} is the energy of the isolated adsorbate molecule in its equilibrium position, E_{slab} is the total energy of the slab and $E_{(molec+slab)}$ is the total energy of the adsorbate/slab system. A positive E_{ads} corresponds to a stable adsorbate/slab system. The energy E_{molec} of the isolated adsorbate molecule in Eq. (VII-1) was determined from calculations performed on a single molecule in a cubic cell of length 12 Å. The same Brillouin-zone sampling has been used to calculate the energies of the bare slab and of the molecule-slab systems. There were two slight variations from the above general definition. The first one corresponds to the case when ClCN adsorption is mediated by an OH group with formation of an OH···NCCl complex. In this case the E_{slab} energy in Eq. (VII-1) was taken as representing the total energy of the slab model and of the OH group adsorbed on the surface. Secondly, in the case of the dissociated species, Cl+CN,

the total binding energies are reported for uniformity with respect to the energy of the bare slab and of an isolated ClCN molecule in gas phase, and are designed as ΔE.

The TEDA-ClCN gas phase investigations are done by optimizations performed in large supercells of 15x15x20 $Å^3$ size. This choice of the supercell model was considered in order to minimize the lateral interactions that might exist between the repeating periodic units

As was described in our previous work[122,131] the computational method described above has been tested to predict the properties of γ-Al_2O_3 surface as well as of the molecular species TEDA, CO and HCN. In this study we further expand our tests by comparing in Table 7 the calculated bond distances and the vibrational frequencies for gas phase ClCN, NCO and CN species to the corresponding experimental or other reported theoretical data. As can be seen from the data in Table 7 both the calculated geometric parameters and the vibrational frequencies reproduce sufficiently accurately the experimental data. The largest variations are noticed for the geometric parameters of the NCO radical for which the equilibrium distance r^{exp}(C-O)=1.206 Å was determined to be slightly larger than r^{exp}(C-N)=1.200 Å. However, our calculations indicate a slighter larger value for the C-N bond distance, r^{calc}(C-N)=1.229 Å, than for the C-O distance, r^{calc}(C-O)=1.192 Å, in good agreement to other *ab initio* calculated values.[132] For example, as can be seen in Table 7 the geometric parameters predicted in this study using GGA-PW91 method are practically identical to those determined using the high quality *ab initio* MR-CI method from Ref. [132].

Table 7. Comparison of the Calculated Bond Distances and Vibrational Frequencies of ClCN and NCO Systems in Gas Phase to the Corresponding Experimental Data or Other Theoretical Values.

System		d(Cl-C)	d(C-N)	d(C-O)	ν(C-Cl)	ν(C-O)	ν(C-N)
ClCN	(calc)[a]	1.623	1.166		729		2200
	(exp)[b]	1.629	1.160		744		2216
NCO	(calc)[a]		1.230	1.191		1240	1961
	(MR-CI)[c]		1.230	1.190			
	(exp)[d]		1.200	1.206		1279	1951
CN	(calc)[a]		1.173				2067
	(exp)[b]		1.172				2068

[a] Values calculated in the current study. [b] Experimental values from Ref.[133]. [c] Theoretical values indicated in Ref. [132]; [d] Experimental values from Ref. [132].

Based on these and our previous sets of results[122,131] it is expected that the current computational method is able to provide an accurate description of both TEDA, ClCN NCO and CN molecular systems and their interactions with γ-alumina surfaces.

VI.4 Results

VI.4.A ClCN adsorption on a γ-Al_2O_3 surface

A condensed ClCN layer was formed on the outer geometrical surface of the pressed-disk γ-Al_2O_3 sample upon ClCN exposure at 110 K. The FTIR spectrum of the ice-like ClCN layer in the ν(O-H) and ν(C≡N) spectral regions is shown separately in Figure VI-2 (a) and (b). The sharp spectral line shape and frequencies of the ice peaks are identical to those of crystalline ClCN.[134] It was observed that the absorbance of the sharp ClCN vibrational modes increases monotonously as dosage increases and that the isolated Al-OH modes are hardly influenced upon ClCN adsorption, as would be expected for ClCN(s) formation on the outer geometric surface of the γ-Al_2O_3 powder at 110 K. The condensed ClCN phase is detectable up to ~ 150 K judging by the sharp modes.

The spectral changes upon heating up to 500 K in vacuum following the formation of the outer-surface crystalline ClCN film at 110 K are shown in Figures VI-2 – VI-4. For ease of

understanding, frequency assignments for the species are given on the labels in the spectra and the bold arrows indicate the growth or loss of absorbance upon raising temperature. FTIR spectra in the first heating stage (110 K – 160 K) are shown in Figure VI-2. Two broad bands develop at ~ 2275 cm^{-1} and ~ 2204 cm^{-1} in the ν(C≡N) region upon heating. The ClCN molecule can adsorb on both the Lewis acid sites and the Brønsted acid sites on the γ-Al_2O_3 surface. The hydrogen bonding of ClCN to Al-OH groups (Brønsted acid sites) produces the associated OH species (3650 cm^{-1} – 3400 cm^{-1}) while consuming the higher frequency isolated Al-OH species (3800 cm^{-1} – 3650 cm^{-1}), as is shown in the ν(O-H) region in Figure VI-2 (a). In the ~ 2275 cm^{-1} region, at least two vibrational modes are overlapped as shown in the insert to Figure VI-2 (b). The incremental increase in the spectral absorbance for each temperature interval is obtained by spectrum subtraction of the 110 K spectrum providing enhanced resolution of the overlapped modes, and the increments from 130 K to 160 K are shown in the insert to Figure VI-2 (b). Two features at ~ 2287 cm^{-1} and ~ 2271 cm^{-1} are barely resolved in the insert. The mode at ~ 2287 cm^{-1} is assigned to ν(C≡N) of ClCN species adsorbed on Lewis acid Al^{3+} sites. The mode at ~ 2271 cm^{-1} is assigned to ν(C≡N) of the cyanate species, Al_2-OCN, which is due to the dissociative adsorption of ClCN on Lewis base sites (Al-O-Al). The two kinds of ClCN species bound to Al-OH (~ 2204 cm^{-1}) and Al^{3+} sites (~ 2287 cm^{-1}), as well as Al_2-OCN species, increase in absorbance upon heating to 160 K, as the condensed ClCN molecules are depopulated. The AlOH···NCCl species (~ 2204 cm^{-1}) have disappeared by about 210 K (Figure VI-3(b)), whereas the Al-NCCl (~ 2287 cm^{-1}) species increase in infrared absorbance up to about 300 K.

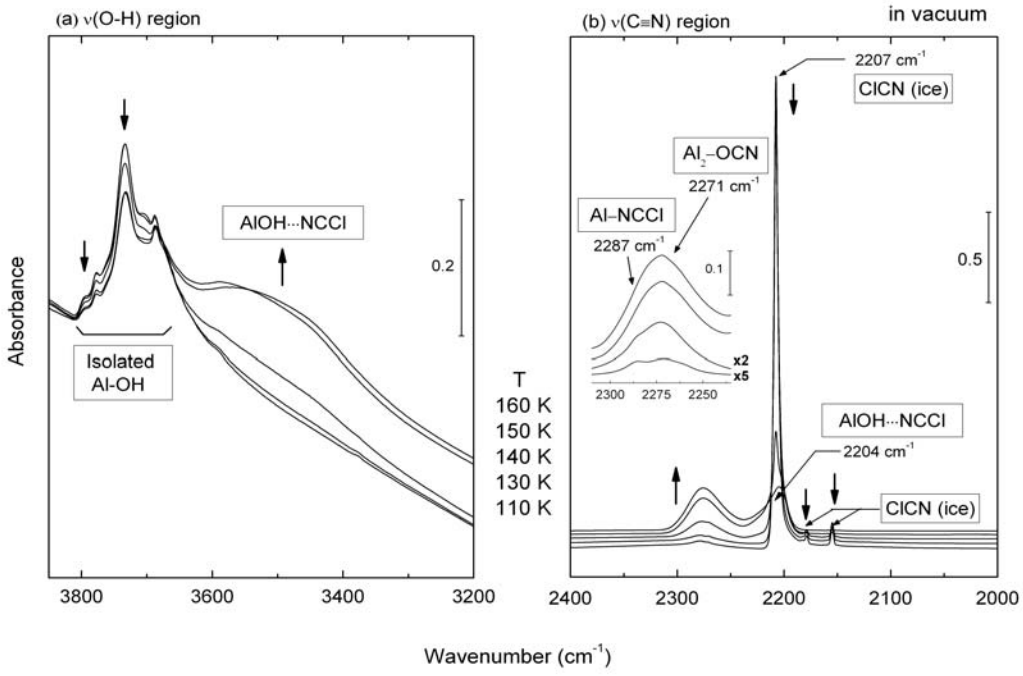

Figure VI-2. FTIR spectra for ClCN adsorption on γ-Al_2O_3 at 110 K followed by sequential heating up to 160 K at vacuum: (a) in the ν(O-H) region; (b) in the ν(C≡N) region. The left insert shows the incremental increase in FTIR spectrum from 130 K to 160 K using difference spectra based in the 110 K spectra.

The spectra in the ν(C≡N) and ν(O-H) vibrational region for heating in the range of 170 K – 290 K are shown in Figure VI-3. The ClCN species adsorbed on Brønsted acid sites (Al-OH···NCCl at ~ 2204 cm^{-1}) begin to decrease in intensity near 170 K and the associated OH species are simultaneously converted back to particular isolated Al-OH species (~ 3730 cm^{-1}). But the comparison with the Al-OH spectrum before ClCN exposure (dotted line) shows that the regeneration of isolated Al-OH species is not complete, and the basic isolated Al-OH modes in the ~ 3780 cm^{-1} region do not return at all. In the ν(C≡N) region a new feature at ~ 2245 cm^{-1} develops accompanied by the development of another weak mode at ~ 1342 cm^{-1} (not shown here). These modes are assigned to ν_{as}(NCO) (~ 2245 cm^{-1}) and ν_s(NCO) (~ 1342 cm^{-1}) modes of the isocyanate Al-NCO species.[135] The basis for this assignment, comparing the behavior of Al-^{16}OH and Al-^{18}OH covered surfaces, will be shown in Figure VI-5.

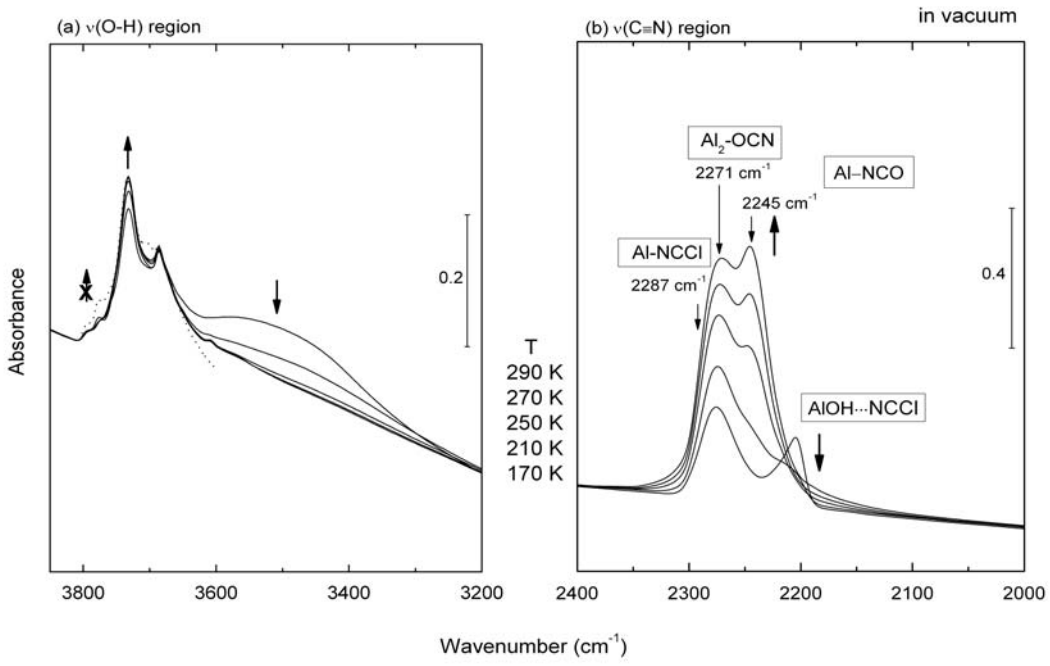

Figure VI-3. FTIR spectra for ClCN adsorption on γ-Al_2O_3 upon heating in the range of 170 K – 290 K: (a) in the ν(O-H) region, compared to the spectrum before ClCN exposure (dotted line); (b) in the ν(C≡N) region.

In the third heating stage, from 310 K to 500 K (Figure VI-4), the Al_2-OCN species at ~ 2271 cm^{-1} still increase in absorbance. The Al-NCO species at ~ 2245 cm^{-1} also gain intensity in a process associated with the consumption of isolated Al-OH species with frequencies at ~ 3780 cm^{-1} and ~ 3740 cm^{-1}. In addition, a broad feature centered at about 3600 cm^{-1} increases in absorbance upon heating, as has been observed upon HCl adsorption on the alumina surface. It has been reported that a broad band centered between 3400 ~ 3500 cm^{-1} develops upon HCl dissociative adsorption on γ-Al_2O_3 surfaces. The broad feature has been assigned to new Al-OH groups with a Cl atom nearby, which is caused by the HCl interaction with Lewis base sites (Al-O-Al) on the surfaces.[136-138] However, HCl gas phase is not observed in the FTIR spectra in this work, since it will condense on the *l*-N_2 filled reentrant Dewar which holds the sample grid. A new band at ~ 2190 cm^{-1} in the ν(C≡N) region is attributed to ClCN thermal decomposition on the surface and is assigned to Al-CN species in accordance with our previous study.[131]

In the last stage above 550 K, the Al-NCO and Al_2-OCN species are depopulated forming decomposed residues on the surfaces (not shown here).

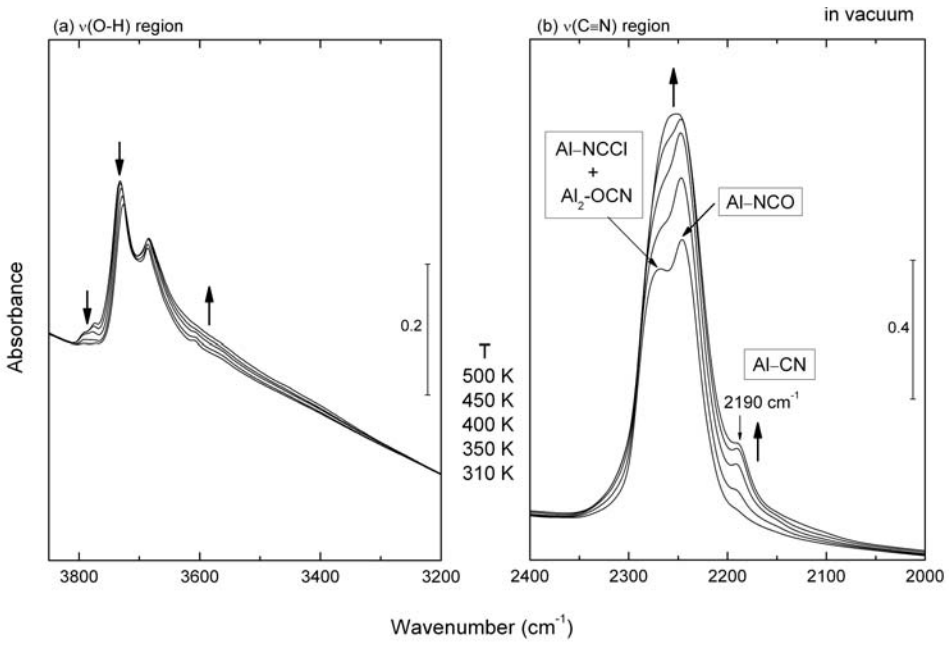

Figure VI-4. FTIR spectra for ClCN adsorption on γ-Al_2O_3 upon heating in the range of 310 K – 500 K: (a) in the ν(O-H) region, compared to the spectrum before ClCN exposure (blue line); (b) in the ν(C≡N) region.

Figure VI-5 shows the FTIR spectra for the ClCN adsorption and decomposition on the Al-^{18}OH isotopically labeled Al_2O_3 surface compared to the Al-^{16}OH surface. The spectra of the Al-OH groups after $H_2{}^{18}O$ treatment are shown in Figure VI-5 (a), compared to that before ^{18}O labeling (dashed line). The isolated Al-OH bands are observed to shift downward by ~ 11 cm^{-1} due to the isotopic labeling of Al^{16}O-H with heavier mass ^{18}O. The calculated ν(O-H) vibrational shift at ~ 3733 cm^{-1} with ^{18}O isotope labeling is ~ -13 cm^{-1} based on the change in reduced mass. It is assumed that most of the surface Al-^{16}OH groups change to Al-^{18}OH in this work. The spectral change for the ClCN adsorption on the Al-^{18}OH labeled Al_2O_3 surface in the ν(C≡N) region at 170 K and 250 K is shown in Figure VI-5 (b) (dashed lines for Al-^{16}OH labeling are

reproduced from Figure VI-3). The Al-NCO species at ~ 2245 cm^{-1} produced near 250 K is shifted by ~ -25 cm^{-1}, whereas the mode at ~ 2200 cm^{-1} due to Al-OH···NCCl and the spectral features in the 2275 cm^{-1} region due to Al-NCCl and Al_2-OCN are hardly affected, as seen in Figure VI-5 (b). This indicates that the Al-NCO formation is due to the interaction of ClCN with Al-OH groups on the Al_2O_3 surface with the formation of HCl.

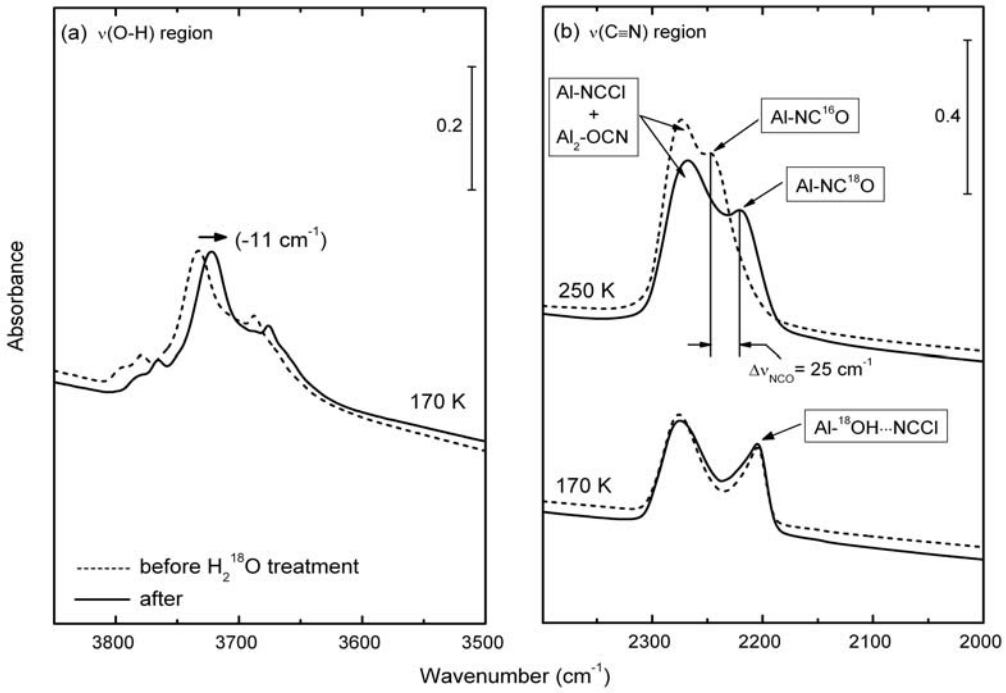

Figure VI-5. FTIR spectra for the ClCN adsorption on Al-^{18}OH isotopically labeled γ-Al_2O_3 surface, compared to those before ^{18}O labeling (dashed line): (a) in the ν(O-H) region before ClCN exposure; (b) in the ν(C≡N) region after ClCN exposure at 170 K and 250 K.

VI.4.B ClCN adsorption on a TEDA-precovered γ-Al_2O_3 surface

FTIR spectra for ClCN adsorption on a TEDA-precovered γ-Al_2O_3 surface are shown in Figure VI-6 (a), compared to (b) which corresponds to ClCN adsorption on the clean γ-Al_2O_3 surface. Since surface active sites are blocked by adsorbed TEDA molecules, the amount of ClCN adsorbed is much less than that on the clean alumina surface. Upon heating the ClCN/TEDA layer above 170 K, the development of Al_2-OCN and Al-NCO is also observed

(not shown here) as seen on the γ-Al_2O_3 surface (Figure VI-3(b) and VI-4(b)). Blocking of the surface by TEDA causes strong attenuation of Al-NCO formation due to lack of Al^{3+} site availability.

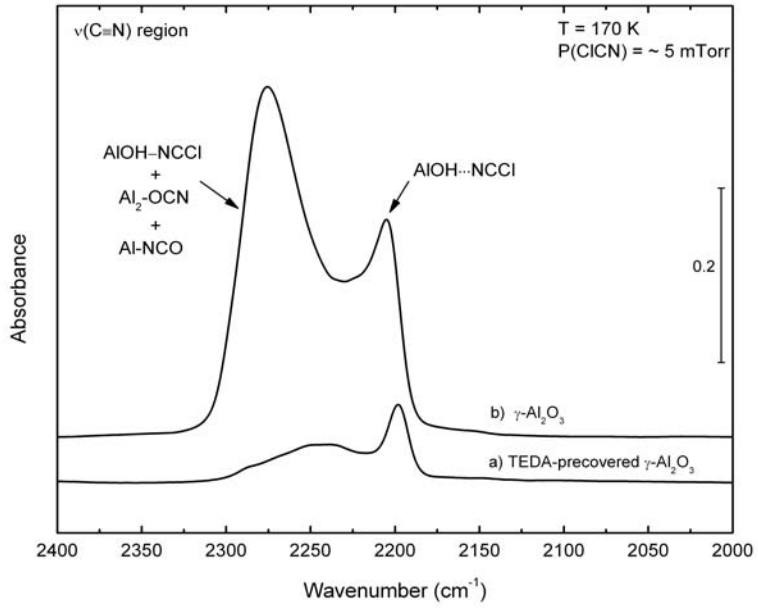

Figure VI-6. FTIR spectra for ClCN adsorption at 170 K at a ClCN equilibrium pressure of ~ 5 mTorr in the ν(C≡N) region: (a) on the TEDA-precovered γ-Al_2O_3 surface; (b) on the γ-Al_2O_3 surface preheated at 950 K.

The spectroscopic evaluation of the interaction of TEDA and ClCN is made by carefully looking for changes in the IR spectra of ClCN and TEDA during adsorption of ClCN. In Figure VI-7 and VI-8 respectively, the spectral regions corresponding to ν(C≡N) for ClCN and ν(C-H) and δ(C-N) for TEDA are shown as the coverage of ClCN is increased at 170 K. No new spectral features are observed upon ClCN adsorption on the TEDA precovered γ-Al_2O_3 surface in both the TEDA and ClCN spectral regions. Minor frequency shifts compared to measurements on pure γ-Al_2O_3 are only observed in the ν(C≡N) region, which might be caused by the effect of the pre-adsorbed TEDA species. No spectral shift in the TEDA vibrational modes is observed in the TEDA spectral region upon ClCN adsorption (Figure VI-8). Moreover, as the pressure of ClCN increases, TEDA molecules are displaced from the surface with the loss of their absorbance, as

seen in Figure VI-8. These results indicate that ClCN molecules do not undergo direct chemical interactions with the exposed nitrogen atoms of pre-adsorbed TEDA species but effectively compete with TEDA for surface active sites on γ-Al_2O_3.

To summarize the experimental observations, ClCN is observed to adsorb non-dissociatively on both Al^{3+} sites and on Al-OH sites and dissociatively on Al-O-Al sites producing Al_2-OCN species at 110 K. The Al-OH···NCCl species desorb and react above 170 K to produce Al-NCO species and HCl. Above ~310 K, Al-CN species are also produced. The most reactive Al-OH species are those of higher frequency (most basic) in the ~ 3780 cm^{-1} region.

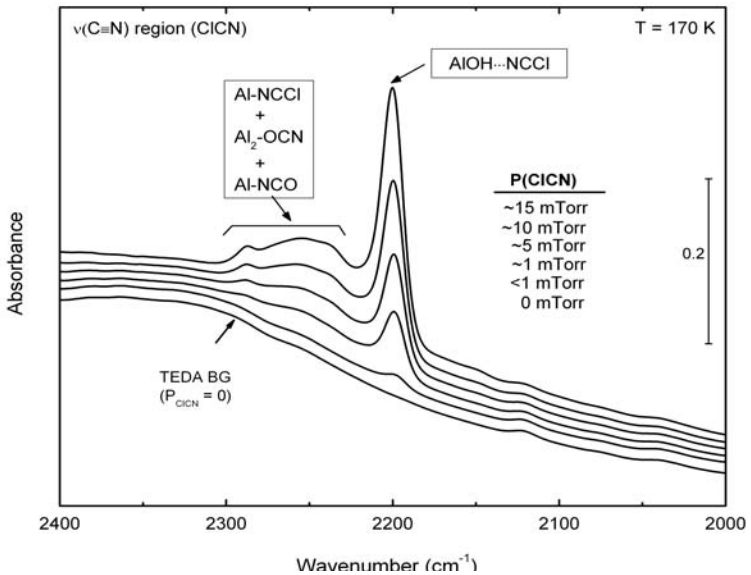

Figure VI-7. FTIR spectra of the TEDA-precovered Al_2O_3 surface in the ν(C≡N) region upon ClCN adsorption.

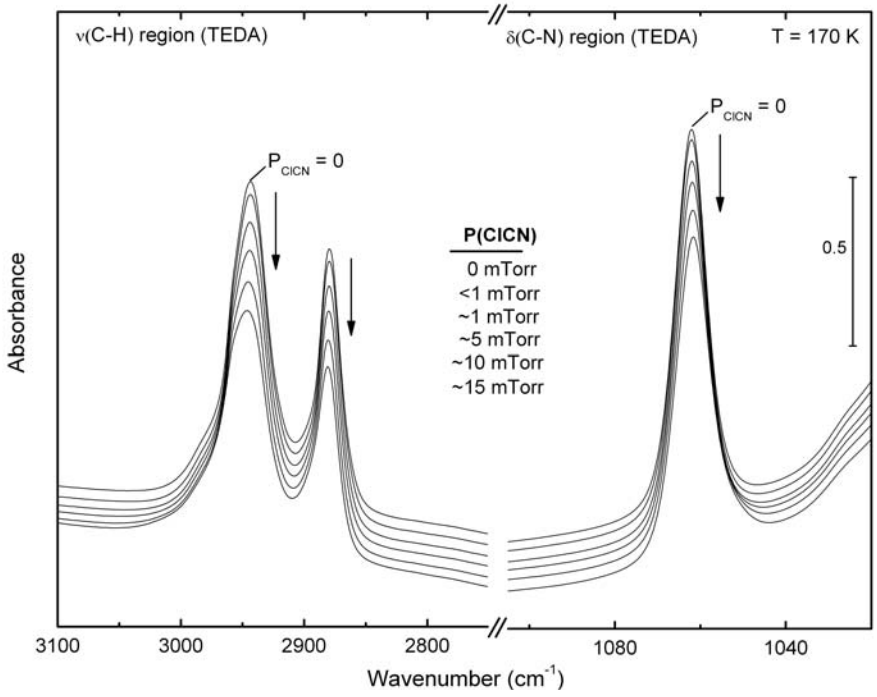

Figure VI-8. FTIR spectra of the TEDA-precovered Al_2O_3 surface in the ν(C-H) and δ(C-N) frequency regions for TEDA upon ClCN adsorption.

VI.5 Discussion

VI.5.A ClCN Adsorption and Reaction on Clean γ-Al_2O_3 Surfaces

Thermally activated diffusion, adsorption, and decomposition of ClCN on a partially dehydroxylated γ-Al_2O_3 surface have been demonstrated in the present work. At higher temperature above ~ 110 K, ClCN molecules in the condensed phase diffuse into the porous γ-Al_2O_3 structure and interact with the surface sites of the γ-Al_2O_3. Adsorbed ClCN is present up to ~ 300 K acting as a source of undecomposed ClCN molecules up to this temperature. During a temperature programmed desorption experiment, free sublimation of the condensed ClCN is detected first at ~ 145 K (not shown). Based on ClCN thermal desorption studies, extending to above 550 K, most of the ClCN adsorbed as an ice in these experiments diffuses into the γ-Al_2O_3 interior.

The adsorption of ClCN on the γ-Al_2O_3 surface takes place at Lewis acid Al^{3+}, Brønsted acid Al-OH, and Lewis base Al-O-Al sites. The theoretical results corresponding to adsorption of ClCN on the γ-Al_2O_3 (100) and (110) surface are given in Table 8 compared with experimental results, while representative configurations are depicted in Figure VI-9. It is found that NCCl can bind on the Lewis Al^{3+} sites in a normal configuration with energies in the range 7.5-13.3 kcal/mol on the (100) surface and up to 29.2 kcal/mol on the (110) surface. It might be expected that the ClCN molecule is capable of binding to the surface via a chlorine atom as well as via a nitrogen atom. But, we noted that the binding of ClCN to Lewis acid sites via the chlorine atom shows only weak physisorbed states identified with binding energies less than 2.4 kcal/mol. The binding energies of Al-OH···NCCl are relatively small with values in the range 4.6 – 5.7 kcal/mol. This is consistent with ClCN desorption from these Al-OH sites in the lower temperature region, 170 K – 290 K. The adsorption of ClCN on the Al-OH groups via the chlorine atom is not energetically favorable either. On the dehydroxylated γ-Al_2O_3 surface there is a large quantity of Lewis base sites, where the ClCN adsorption is expected as well. The dissociative adsorption of ClCN takes place on these sites forming Cl(a) and CN(a) species adsorbed at nearby Al and O surface sites respectively. The Al_2-OCN species thus produced from the dissociative adsorption exhibits several stable configurations with binding energies up to ~ 35.1 kcal/mol.

However, it has been reported that when the molecules containing a CN moiety such as HCN and CH_3CN are adsorbed on metal oxide surfaces followed by activation thermally or photochemically, isocyanate (M-NCO) is produced.[117,125,139] In our work, the formation of Al-NCO species is also found at very low temperature by the reaction of ClCN with Al-OH groups on the surface. Here, two possible mechanisms for the Al-NCO formation can be proposed. In

the second heating stage (170 K – 290 K), desorbing ClCN molecules from Al-OH sites react with Al-OH to produce Al-NCO consuming isolated Al-OH groups. In this temperature region, the reaction takes places with the most basic Al-OH groups with a vibrational frequency in the ~ 3780 cm^{-1} region. Then in the higher temperature stage (310 K – 500 K), where the Al-OH···NCCl species have largely disappeared, the ClCN molecules adsorbed at Al^{3+} sites contribute to Al-NCO production by reacting with neighboring Al-OH groups. In such cases it is observed that there is a significant interaction between C atom in the ClCN and the O atom in the Al-OH group in our theoretical analyses (not shown). In addition, one of Al-NCO-Al bridged configurations exhibits its theoretical ν(C≡N) frequency in the experimental range for a species with the highest binding energy, ~ 57.5 kcal/mol (see Table 8 and Figure VI-10). Therefore, the contribution of η^2(N,O)-NCO bonding where bonding takes place at both Al^{3+} surface sites involving both O and N atoms is postulated. The adsorption configuration and decomposition products calculated are shown in Figure VI-9. A graphical representation of the theoretical and experimental vibrational frequencies found in this investigation (listed in Table 8) is shown in Figure VI-10.

Table 8. Calculated Equilibrium Distances, Adsorption Energies and Vibrational Frequencies for ClCN and NCO Adsorbed on (100) and (110) Surfaces of γ-Al_2O_3 Surface.[a]

System/ Surface	Bonding Surface Sites	d(Al...X)[b]	E_{ads} or ΔE[c]	ν(C-N) calc.	ν(C-N) exp.
a) Al-NCCl Adsorption					
(100)	Al_V(II)	2.142	7.5	2261	
	Al_V(I)	2.173	8.5	2250	
	Al_V(III)*	2.075	13.3	2268	2287
(110)	Al_{III}(I)*	1.965	29.2	2292	
	Al_{IV}(II)	2.049	14.3	2275	
	Al_{IV}(III)	2.095	7.7	2259	
b) Al-Cl + O-CN					
(100)	Al_V(I), μ_3-O*	2.151	9.6[c]	2248	
(110)	Al_{III}(I), μ_2-O*	2.087	35.1[c]	2259	2271
	Al_{IV}(II), μ_2-O	2.125	22.0[c]	2223	

(Table 8, Continued)

c) Al-NCO Adsorption					
(100)	Al_V(II)	1.916	26.4	2202 (1343)	2245 (1342)
	Al_V(I)	1.856	33.6	2241 (1359)	
	Al_V(III)*	1.886	34.3	2208 (1345)	
	Al_V(I),Al_V(II)[d]	2.036, 2.118	21.0	2151 (1235)	
(110)	Al_{III}(I)*	1.778	56.4	2292 (1395)	
	Al_{IV}(II)	1.859	25.1	2179 (1361)	
	Al_{IV}(III)	1.855	29.7	2200 (1365)	
	Al_{IV}(II),Al_{IV}(II)[d]	2.098, 2.013	31.5	2194 (1357)	
	Al_{III}(I),Al_{IV}(II) [d]	1.873, 2.020	57.5	2238 (1279)	
d) OH…NCCl Adsorption					
(100)	μ_1-Al_V(II)		5.3	2221	2204
	μ_1-Al_V(III)*		5.6	2221	
(110)	μ_1-Al_{III}(I)		4.5	2217	
	μ_1-Al_{IV}(III)		5.7	2226	
	μ_2-Al_{IV}(III)*		5.2	2222	
e) Al-CN					
(100)	Al_V(I)	1.971	32.7	2178	2190
	Al_V(II)	2.032	24.0	2134	
	Al_V(III)	1.988	33.9	2166	
(110)	Al_{IV}(III)	2.002	25.2	2114	
	Al_{IV}(II)	1.975	29.3	2104	
	Al_{III}(I)	1.932	52.8	2191	

[a] Bond distances are given in Angstroms, adsorption energies in kcal/mol and vibrational frequencies in cm^{-1}. Structures indicated with an * are represented in Figures VI-9. [b] X stands for N in the case of ClCN or NCO adsorption with the N atom oriented towards the surface, and for Cl in the case of Al-Cl +O-CN adsorption or TEDA-ClCN structures.
[c] The reported values represent the energy difference relative to the total energy of the slab and the isolated, undissociated molecule. [d] These represent bridged η^2(N,O)-NCO configurations where bonding takes place at both Al^{3+} surface sites involving both O and N atoms.

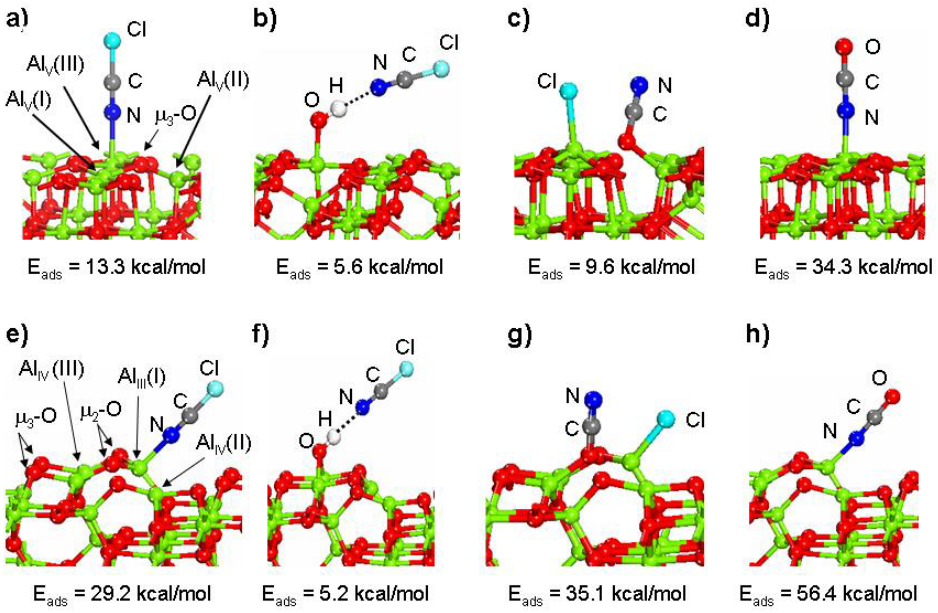

Figure VI-9. Representative adsorption configurations of NCCl molecule on (100) (panels a-c) and (110) (panels d-e) on γ-Al_2O_3 surface. Panels (a, e) and (b, f) correspond to adsorptions configurations at Al^{3+} and Al-OH sites. In configurations (c, g) we indicate the structures corresponding to a dissociated ClCN molecule on the surface with formation of adsorbed Cl and CN systems. The Al-NCO configurations are shown in (d, h).

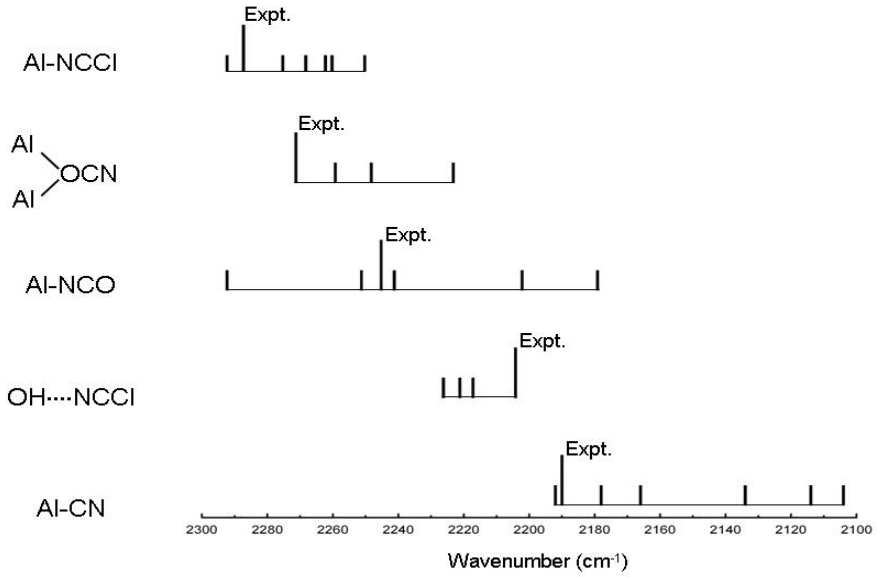

Figure VI-10. Theoretical and experimental frequencies observed for ClCN interaction with γ-Al_2O_3. The frequency values are from Table 8

VI.5.B ClCN Adsorption on TEDA-precovered γ-Al_2O_3 Surfaces

In our previous studies it has been demonstrated that triethylenediamine (TEDA) adsorbs on unsaturated aluminum atom sites (Lewis acid Al^{3+} sites), with adsorption energies in the range of 13.8 – 40.0 kcal/mol. TEDA also binds to Al-OH Brønsted acid sites by formation of OH···N hydrogen bonds, which are weaker than found for the TEDA bonding to Al^{3+} sites, exhibiting energies in the range 16.4 – 18.3 kcal/mol. Due to repulsive interaction between TEDA molecules at high coverage, TEDA desorption energies of ~ 3.7 kcal/mol were experimentally observed.[87] Upon chemical interaction of the Al^{3+} sites with the nitrogen atom of a TEDA molecule, a shift of ~ -4 cm^{-1} from the gas phase frequencies in the δ(C-N) mode was observed.[81]

Since the surface sites are pre-occupied by TEDA, most of the species formed on clean Al_2O_3 surfaces are absent on the TEDA functionalized γ-Al_2O_3 surface, as seen in Figure VI-6. As the ClCN pressure increases, displacement of TEDA molecules from the surface, where the ClCN binding energy is competitive with the TEDA binding energy, is also observed, as shown in Figure VI-8.

If the exposed amine group in TEDA is directly involved in bonding with ClCN, the formation of $(TEDA\cdots CN)^+$ species would be expected, as described in Figure VI-1. According to our theoretical calculation the ν(C≡N) frequency should be ~ 2384 cm^{-1} and the δ(C-N) mode in TEDA should be ~ 1558 cm^{-1}. These two modes are shifted by ~ +168 cm^{-1} and ~ -6 cm^{-1} from the TEDA and ClCN gas phase frequencies respectively in such an ionic (TEDA···CN) complex. Neither of these shifted modes is experimentally observed when ClCN and TEDA are adsorbed together indicating this complex does not form on the surface.

The interactions between TEDA and ClCN molecules in the gas phase have been investigated theoretically, and a pictorial view of the most stable adsorption configurations of the

TEDA-ClCN and TEDA-CN complexes are shown in Figure VI-12. The interaction between TEDA and ClCN is very weak with binding energy of ~ 5.3 kcal/mol, whereas higher bonding energy (28.6 kcal/mol) is calculated in the TEDA and CN system with CN bonding to the N atom of TEDA. The most stable configuration involves a CN radical oriented parallel to one of the TEDA faces, interacting with H atoms with a binding energy of ~ 32.5 kcal/mol.

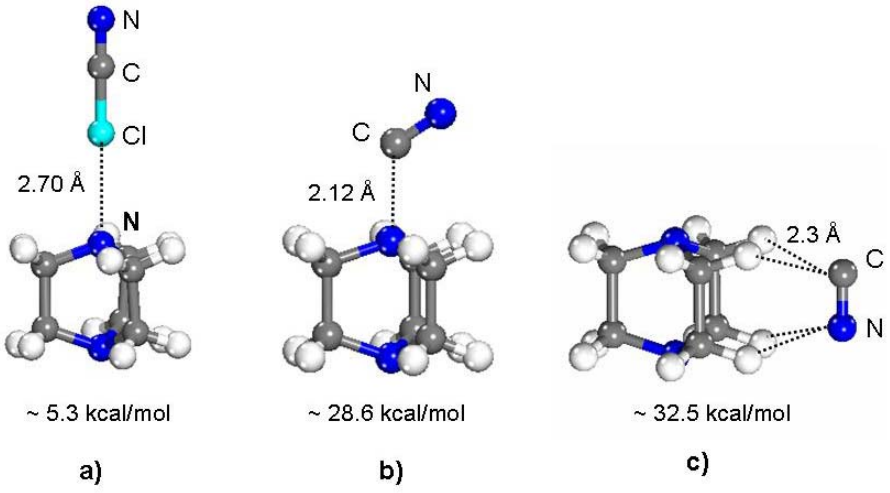

Figure VI-11. Pictorial view of the gas phase (a) TEDA-ClCN and (b, c) TEDA-CN complexes with binding energy values with respect to isolated TEDA and ClCN molecules.

However, both direct interactions between these molecular systems as well as the interaction with the surface will contribute in determining the final equilibrium state on surface. The properties of the TEDA-ClCN system is further analyzed on the γ-Al_2O_3 surface and coadsorption states are represented in Figure VI-12 while the corresponding energetic and selective geometric parameters are detailed in Table 9. In such cases the TEDA molecule is adsorbed at one of the most stable sites on either (100) or (110) γ-Al_2O_3 and binding configurations of ClCN either on-top of the TEDA molecule or directly to the surface are considered. The direct binding energies between TEDA and ClCN (or CN) through the exposed nitrogen atom in TEDA (Figure VI-12 a, c, e, and g) are calculated to be reduced to 3.0 kcal/mol

(~ 5.3 kcal/mol in gas phase) in the TEDA-ClCN case and 25.3 kcal/mol (~ 28.6 kcal/mol in gas phase) in the TEDA-CN case on surfaces where TEDA is adsorbed. The energy values are still lower than those values (7.5 – 29.2 kcal/mol for ClCN adsorption and 24.3 ~ 53.2 kcal/mol in the CN adsorption case) on clean γ-Al_2O_3. Moreover, in all cases where CN binds directly to the vacant surface sites near an adsorbed TEDA molecule, the CN binding energy increases into the range of 40.2 – 71.6 kcal/mol. In TEDA-NC coadsorption case, where nitrogen of CN binds to surface, it is also calculated that NC likely adsorbs to surface near a TEDA molecules with higher adsorption energies compared to those on clean surfaces. Thus the theoretical calculations suggest that TEDA will enhance the adsorption energy of CN on γ-Al_2O_3 by an indirect attractive interaction. These theoretical results indicate that the direct bonding of ClCN molecules to the exposed amine moiety of a TEDA molecule is unlikely on energetic grounds and ClCN binds preferentially to the γ-Al_2O_3 surface sites unoccupied by TEDA molecules.

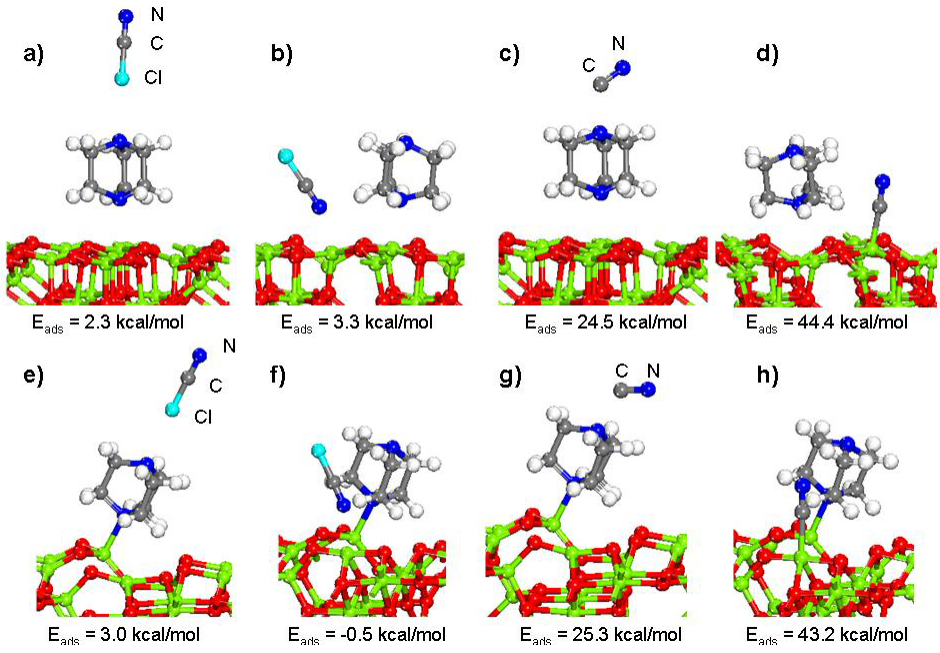

Figure VI-12. Representative adsorption configurations of ClCN (panels a, e) and CN (panels c, g) molecules adsorbed on top of an adsorbed TEDA molecule. Panels (b, f) and (d, h) indicate coadsorption structures of TEDA-ClCN and respectively TEDA-CN systems. Panels in the upper row correspond to the (100) surface while those in the second row to the (110) surface.

Table 9. Calculated Equilibrium Distances, Adsorption Energies and Selective C-N Stretching Frequencies for ClCN or CN Species when Coadsorbed with a TEDA Molecule on (100) and (110) Surfaces of γ-Al_2O_3 Surface.

System/ Surface	Bonding Sites	d(Al-X)[a]	d(N…Y)[b]	E_{ads}	ν(C-N)
(a) TEDA…NCCl Coadsorption					
(100)	$T(Al_V(III))$-NCCl (top)*		2.807	2.3	2186
	$T(Al_V(III))$, NCCl($Al_V(I)$)	2.218		2.4	
	$T(Al_V(III))$, NCCl($Al_V(II)$)	2.451		2.3	
	$T(Al_V(III))$, NCCl($Al_V(I)$, far)	2.084		9.7	2265
	$T(Al_V(I))$, NCCl($Al_V(III)$)	2.195		3.3	
	$T(Al_V(I))$, NCCl($Al_V(II)$)	2.194		4.5	
	$T(Al_V(II))$, NCCl($Al_V(III)$)	2.137		7.5	2245
(110)	$T(Al_{III}(I))$-NCCl(top)*	2.792		3.0	2188
	$T(Al_{III}(I))$, NCCl($Al_{IV}(III)$)	2.469		1.0	
	$T(Al_{III}(I))$, NCCl($Al_{IV}(II)$)	2.236		-0.5	
	$T(Al_{IV}(II))$, NCCl($Al_{III}(I)$)	1.986		16.9	2256
(b) TEDA…CN Coadsorption					
(100)	$T(Al_V(III))$-CN (top)*		2.089	24.5	2011
	$T(Al_V(III))$, CN ($Al_V(I)$)	2.046		44.4 (32.7)[c]	2143
	$T(Al_V(III))$, CN ($Al_V(II)$)	2.071		40.9 (24.0)[c]	2129
	$T(Al_V(III))$, CN ($Al_V(III)$)	2.016		47.4 (33.9)[c]	2161
	$T(Al_V(III))$, NC ($Al_V(I)$)	1.936		43.1 (33.7)[c]	2091
	$T(Al_V(III))$, NC ($Al_V(II)$)	1.952		39.4 (25.4)[c]	2080
	$T(Al_V(III))$, NC ($Al_V(III)$)	1.914		45.6 (34.8)[c]	2085
(110)	$T(Al_{III}(I))$-CN(top)*		2.073	25.3	2016
	$T(Al_{III}(I))$, CN(Al_{IV}(III)	2.041		40.2 (25.2)[c]	2134
	$T(Al_{III}(I))$, CN($Al_{IV}(II)$)	2.047		43.2 (29.3)[c]	2143
	$T(Al_{IV}(II))$, CN($Al_{III}(I)$)	2.000		71.6 (52.8)[c]	2170

(Table 9, Continued)

$T(Al_{III}(I))$, $NC(Al_{IV}(III)$	1.942	37.8 (25.6)[c]	2087
$T(Al_{III}(I))$, $NC(Al_{IV}(II))$	1.936	40.1 (31.1)[c]	2095
$T(Al_{IV}(II))$, $NC(Al_{III}(I))$	1.885	69.6 (52.8)[c]	2100

[a] d(Al-N) represents the distance between the N atom of either ClCN or the C atom in CN molecules to the surface Al atom involved in bonding. [b] d(N…X) represents the separation between N atom of TEDA and NCCl or CN systems, respectively, cases in which Y stands for Cl atom in ClCN molecule, for C atom in the CN radical. [c] The values in parentheses correspond to binding energy of CN on the surface in the absence of TEDA. Configurations indicated by * are represented in Figure VI-12.

VI.6 Summary

The adsorption of ClCN on TEDA-precovered γ-Al_2O_3 surface has been studied using transmission FTIR spectroscopy. It is demonstrated that there is no direct binding of ClCN to the exposed amine group on TEDA pre-adsorbed on γ-Al_2O_3. Instead the TEDA molecule effectively competes with ClCN for binding sites on the γ-Al_2O_3 surface.

In addition, the adsorption behavior of ClCN on the γ-Al_2O_3 surface has been studied and the sequence of the processes of diffusion, adsorption, desorption and decomposition of ClCN molecules is observed on the γ-Al_2O_3 surface upon heating. Isocyanate (Al-NCO) is produced due to the interaction of ClCN with Al-OH groups on the surface, and evidence for cyanate (Al_2-OCN) and cyanide (Al-CN) products is found.

VI.7 Acknowledgement

We acknowledge with thanks the support of this work by The Army Research Office, and discussion with Dr. Alex Balboa of Aberdeen Proving Ground. A grant of computer time at the Army Research Laboratory is also gratefully acknowledged.

PART III. FTIR Spectroscopic Study of Surface Diffusion

VII. Diffusion of 2-Chloroethyl-ethyl Sulfide through Powdered γ-Al_2O_3*

VII.1 Abstract

A new method to study the diffusion properties of molecules into porous materials using transmission IR spectroscopy is employed. A measurement of the diffusion of the 2-chloroethylethyl sulfide (2-CEES) molecule into two types of γ-Al_2O_3 powder is performed, showing that the diffusion rate into sub-nanometer crystallite particle size γ-Al_2O_3 powders (subnano-Al_2O_3) is higher than that into the larger crystallite particle size powder. It is shown that a surface diffusion mechanism can be used to model the diffusion process giving good agreement with the experimental results, where $D_{subnano\text{-}Al_2O_3}$ is ~ 5 times larger than $D_{multinano\text{-}Al_2O_3}$ at 170 K for the 2-CEES molecule.

---

* Reproduced with permission from S. Kim, O. Byl, J.-C. Liu, J. K. Johnson, J. T. Yates, Jr. "Spectroscopic Measurement of Diffusion Kinetics Through Subnanometer and Larger Al_2O_3 Particles By a New Method – The Interaction of 2-chloroethylethyl sulfide with γ-Al_2O_3", Journal of Physical Chemistry B 110, 9204 (2006).

VII.2 Introduction

We introduce in this paper a new experimental method to measure the rate of diffusion of an adsorbable molecule into a packed bed of adsorbent particles. We specifically address the diffusion of the 2-chloroethylethyl sulfide (2-CEES) molecule into packed beds of two types of γ-Al_2O_3 powder which are of sub-nanometer crystallite particle size (subnano-Al_2O_3) and much larger crystallite particle size (multinano-Al_2O_3). The 2-CEES molecule is a simulant for mustard blister agents having both a sulfur functional group and a chlorine functional group.[140,141]

The reaction kinetics of the mustard molecule (2,2′-dichloroethyl sulfide) with nanosize MgO was studied in liquid phase using magic angle spinning NMR (MAS NMR).[142] It was reported that the reaction rate is governed by physical properties of the liquid phase such as liquid surface tension, viscosity, and vapor pressure as well as the reactivity with the MgO surface.

The pulsed field gradient nuclear magnetic resonance method (PFG NMR) has been used to investigate the self-diffusion of organic molecules into nano-scale porous materials.[143,144] The diffusivity could be explained by either of two models: the Knudsen diffusion model and the surface diffusion model. It was concluded that the surface diffusion mechanism is the dominant diffusion control process in the nano-scale pore region, and our results reported below confirm this concept.

Partially hydroxylated Al_2O_3 contains a distribution of isolated hydroxyl groups which are capable of hydrogen bonding to adsorbed molecules.[34,41,74] The formation of hydrogen bonds leads to the loss of the characteristic isolated Al-OH vibrational modes and the formation of associated Al-OH species of lower frequency.[83,145,146] Transmission IR spectroscopy through a packed bed of Al_2O_3 therefore allows one to witness the diffusion of a molecule into the bed

using the isolated Al-OH groups as sensors of the progress of the molecule through the packed bed.

We show that the sub-nanometer size Al_2O_3 particles are more active in promoting the diffusion of the 2-CEES molecules than the larger particle size Al_2O_3. The relative rate of disappearance of isolated Al-OH groups occurs at lower temperatures for the subnano-Al_2O_3 particles than for the multinano-Al_2O_3 particles, and the concomitant formation of associated Al-OH groups occurs also at lower temperatures for the sub-nanometer size particles. In addition, comparison of subnano-Al_2O_3 and multinano-Al_2O_3 particles in competitive diffusion studies of 2-CEES at constant temperature shows that the subnano-Al_2O_3 exhibits a higher rate of diffusion.

VII.3 Experimental

The equipment used to study the diffusion of an adsorbent molecule into a high surface area solid powder consists of a vacuum IR cell[69,70] and a FTIR spectrometer. The cell has two KBr windows for transmission of an IR beam allowing it to pass through the powder held in a supporting W-grid. The base pressure of the vacuum cell is maintained at ~ 1.0×10^{-8} Torr with a turbo-molecular pump.[81] A gas doser is directed toward the sample where, at cryogenic temperature, the incident molecules condense as an ice on the outer geometric surface of the solid powder. The cryogenically cooled manipulator, which holds the powdered sample on the supporting grid within the cell, is movable up and down to observe the spectrum of two different powdered samples, supported one above the other together on the grid. Two different kinds of Al_2O_3 powder sample are pressed into the same W-grid (thickness = 0.005 cm) with a pressure of 70,000 psi. This arrangement allows the diffusion properties of a particular molecule in the two Al_2O_3 samples to be directly compared under exactly the same experimental conditions. The W-grid is suspended between Ni clamps which are connected to Cu leads originating from the

manipulator's reentrant Dewar. A type-K thermocouple is welded to the top of the grid.[39] The temperature as measured by the thermocouple and temperature controller is achieved by resistive heating of the W-grid and the powdered samples via the Cu leads using a temperature control program.[69] The resolution of the temperature is 0.1 K in the range of 83 K – 1400 K. The lower temperature is obtained by cooling the manipulator with liquid N_2.

Powdered γ-Al_2O_3 was obtained from Nanoscale Materials, Inc., Manhattan, KS, and the comparison of the major physical characteristics of two kinds of γ-Al_2O_3 particles is shown in Table 10.

Table 10. Typical properties of two kins of Al_2O_3 powder.

	Multinano-Al_2O_3	Subnano-Al_2O_3
-BET Surface Area (m^2/g)	328	692
-BET Surface Area (our measurement)	392 (354) [a]	777 (463) [a]
-Pore Volume (mL/g)	0.237	1.03
-Pore Volume (our measurement)	0.312 (0.282) [a]	1.35 (0.408) [a]
-Minimum Crystallite Diameter (nm)[b]	2–3	< 1

[a] compressed with 70,000 psi.
[b] The Al_2O_3 crystallite sizes were measured by transmission electron microscopy (private communication, Dr. Olga Koper, Nanoscale Materials, Manhattan, KS).

The γ-Al_2O_3 with crystallite diameters < 1 nm is called subnano-Al_2O_3, and γ-Al_2O_3 with crystallite diameters between 2~3 nm is called multinano-Al_2O_3 in this work. The BET surface area and the pore volume of subnano-Al_2O_3 are higher than of the multinano-Al_2O_3. Even after powder compression the subnano-particles still have a higher surface area (463 m^2/g) and pore

volume (0.408 mL/g) compared to multinano-Al_2O_3 (354 m^2/g, 0.282 mL/g). The Al_2O_3 powder pressed into the W-grid (after removing the excess with a blade) weighs 3.65 ± 0.14 mg for subnano-Al_2O_3 and 3.40 ± 0.10 mg for multinano-Al_2O_3. Optical microscope images of the W-grid with the pressed Al_2O_3 powder are shown Figure VII-1. The filling of the 0.2 mm x 0.2 mm square windows in the grid is > 98 %.

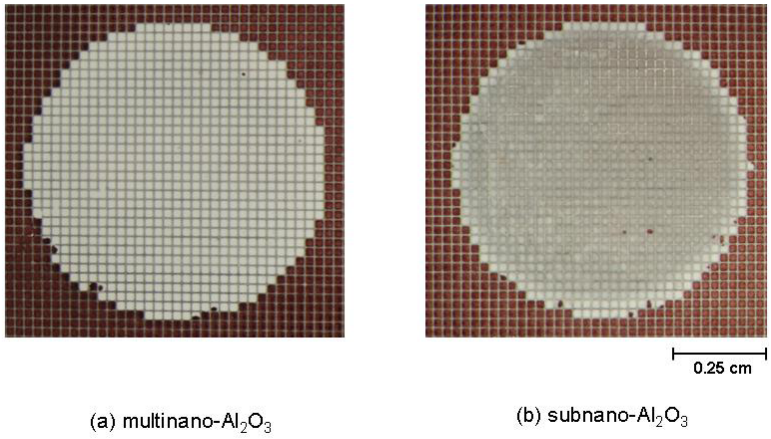

Figure VII-1. Image of γ-Al_2O_3 powder pressed into W-grid with a pressure of 70,000 psi for (a) multinano-Al_2O_3 and (b) subnano-Al_2O_3.

After annealing the two alumina samples (800 K, in vacuum) to produce the isolated Al-OH groups, 2-CEES (g) (supplied as a liquid from Aldrich) is introduced to the Al_2O_3 samples at 126 K to form a condensed film of 2-CEES on their front and back geometrical outer surfaces. All the spectra of 2-CEES on both of the Al_2O_3 surfaces, following a momentarily programmed increase in temperature, are taken after cooling to 126 K which is below the 2-CEES freezing temperature. For the isothermal diffusion experiment at 170 K, after the formation of the 2-CEES ice film on the outer geometric surface at 126 K, the sample is annealed at 165 K briefly before heating to 170 K. The change of absorbance in the ν(OH) region is measured using difference spectra referenced to the initial spectrum at 126 K.

The FTIR spectra are collected with a Bruker TENSOR 27 FT-IR spectrometer by the transmission method. The spectrometer and the optic enclosures are purged continuously with H_2O and CO_2 free air. Each spectrum is obtained by averaging 64 interferograms at 2 cm^{-1} resolution.

VII.4 Results

VII.4.A VII-4A. Behavior of Isolated Al-OH Groups during 2-CEES Diffusion into the Al_2O_3 Interior

Figure VII-2 shows the absorbance behavior of the isolated Al-OH groups as 2-CEES is caused to diffuse into the interior of the compressed powder samples by raising the temperature. Up to 175 K, the inward diffusion process occurs from the 2-CEES layer which is crystalline ice-like, as judged by the IR spectra (to be discussed later) and by a temperature programmed desorption (TPD) experiment (not shown here). The onset of the 2-CEES ice desorption from the outer surface of Al_2O_3 occurs at ~ 175 K in the TPD measurement. Above 175 K, 2-CEES inward diffusion continues and the diffusion process is accompanied by a small amount of desorption from the ice-overlayer. It may be seen that the relative rate of entry of 2-CEES into the interior is greater for subnano-Al_2O_3 than for multinano-Al_2O_3 throughout the experiment. The isolated Al-OH group with its frequency at 3760 cm^{-1} for multinano-Al_2O_3 and at 3740 cm^{-1} for subnano-Al_2O_3 is monitored in each case, and the absorbance of these species decreases upon heating due to the hydrogen bonding. The absorbance changes of ν(OH) are normalized to the change after heating at 240 K for multinano-Al_2O_3 and to 210 K for subnano-Al_2O_3, the temperatures where 2-CEES binding to Al-OH groups is maximized, respectively. Above this temperature in each case the isolated Al-OH groups are restored as a result of extensive desorption of the chemisorbed 2-CEES from the Al-OH trap sites.[83,84]

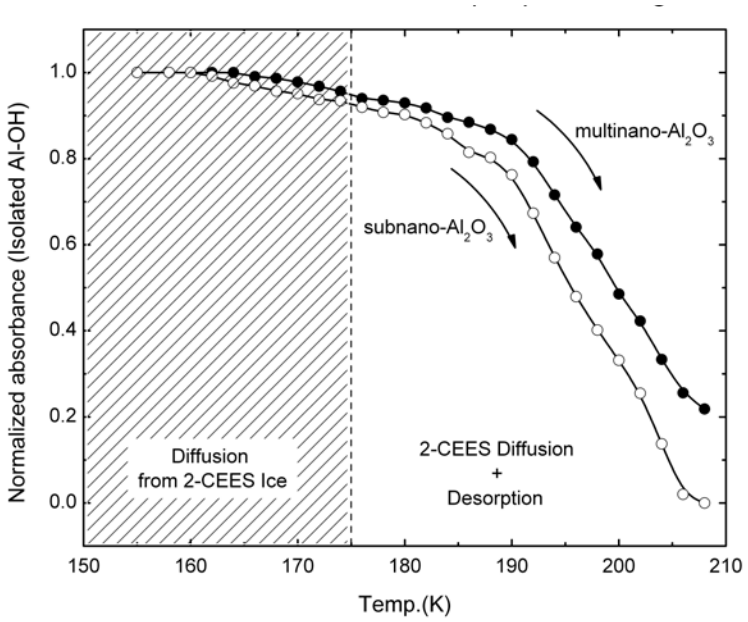

Figure VII-2. Loss of the normalized absorbance of isolated Al-OH groups at ~ 3760 cm^{-1} for multinano-Al_2O_3 (filled circles) and at ~ 3740 cm^{-1} for subnano-Al_2O_3 (open circles) upon increasing the temperature. All the FTIR spectra are measured at 126 K. The absorbance change is normalized by that obtained at higher temperature where 2-CEES binding to Al-OH groups is maximized at 240 K for multinano-Al_2O_3 and at 210 K for subnano-Al_2O_3 respectively.

In order to constantly maintain an outer layer of crystalline ice-like 2-CEES during the diffusion process, a second type of diffusion experiment was carried out isothermally at 170 K, where the presence of crystalline ice-like 2-CEES at the outer geometrical boundary of the powdered Al_2O_3 bed was verified by its IR spectrum throughout the experiment. In a similar fashion to the temperature dependence experiment in Figure VII-2, the absorbance change of ν(OH) is normalized to that after heating at 240 K for multinano-Al_2O_3 and 210 K for subnano-Al_2O_3 (the FTIR spectra during diffusion at 170 K will be shown in Figures VII-4 and VII-5).

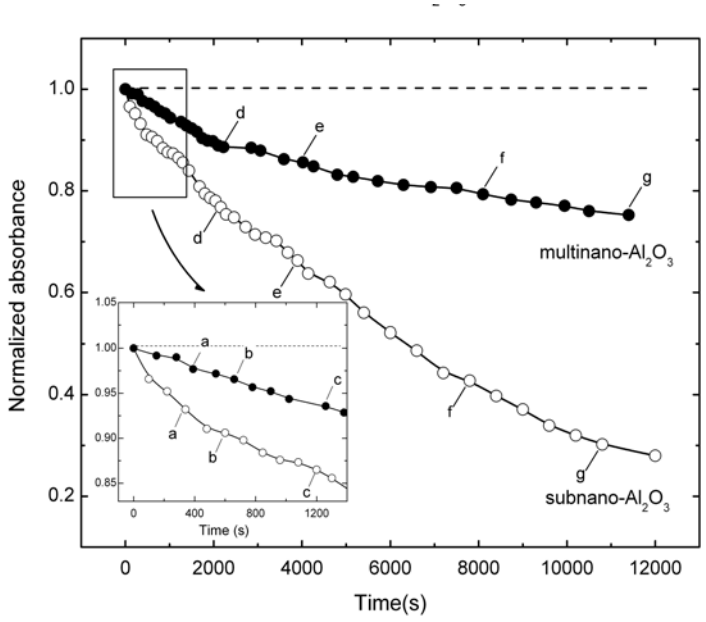

Figure VII-3. Plot of the loss of the normalized absorbance of isolated Al-OH at ~ 3760 cm^{-1} for multinano-Al_2O_3 (filled circles) and at ~ 3740 cm^{-1} for subnano-Al_2O_3 (open circles) as a function of heating time at 170 K. A magnified image in the region for 0 s – 1400 s is shown in the lower inset. The absorbance change is normalized by the change obtained after heating the sample at 240 K for multinano-Al_2O_3 and at 210 K for subnano-Al_2O_3. The data points noted as a – g on the multinano-Al_2O_3 curve correspond to those at 390 s, 660 s, 1260 s, 2220 s, 4020 s, 8100 s, and 11400 s, and similarly on the subnano-Al_2O_3 curve correspond to 340 s, 600 s, 1200 s, 2160 s, 3900 s, 7800 s, and 10800 s. FTIR spectra for these diffusion times are given in Figures VII-4 and VII-5.

The results of this experiment are shown in Figure VII-3, comparing the two types of Al_2O_3. Again it is observed that the subnano-Al_2O_3 exhibits a more rapid relative rate of loss of isolated Al-OH groups, compared to multinano-Al_2O_3. After 1000 s, the fraction of the isolated Al-OH groups consumed on the subnano-Al_2O_3 by hydrogen bonding to 2-CEES is almost twice that observed for the multinano-Al_2O_3. By the end of the experiment at 170 K, when 12000 s of diffusion has occurred, the subnano-Al_2O_3 has, in a relative way, experienced about three times the consumption Al-OH groups compared to the multinano-Al_2O_3 sample, using the normalized ν(OH) absorbance for this kinetic comparison.

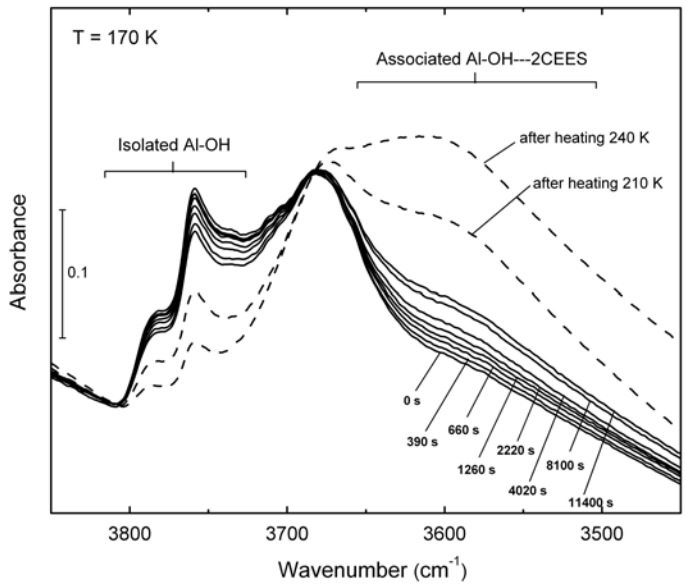

Figure VII-4. FTIR spectra of 2-CEES on the multinano-Al_2O_3 at 170 K with increasing time in the ν(OH) region. The formation of the 2-CEES ice film is carried out at 126 K.

Figure VII-4 shows the infrared spectrum of multinano-Al_2O_3 during the diffusion of 2-CEES into the interior of the compressed powder at 170 K. Two sharp IR features at ~ 3780 cm^{-1} and ~ 3760 cm^{-1} due to isolated Al-OH groups are observed to disappear monotonically, while a broad associated-OH band near 3600 cm^{-1} forms. The broad band is due to hydrogen bonding of the isolated Al-OH groups to the 2-CEES molecule, and this process has been reported previously using another γ- Al_2O_3 material.[83,84] Figure VII-4 also shows the enhanced loss of isolated Al-OH species from the surface after heating to 210 K and 240 K respectively, where the formation of associated OH groups and the loss of the isolated OH groups has been maximized.

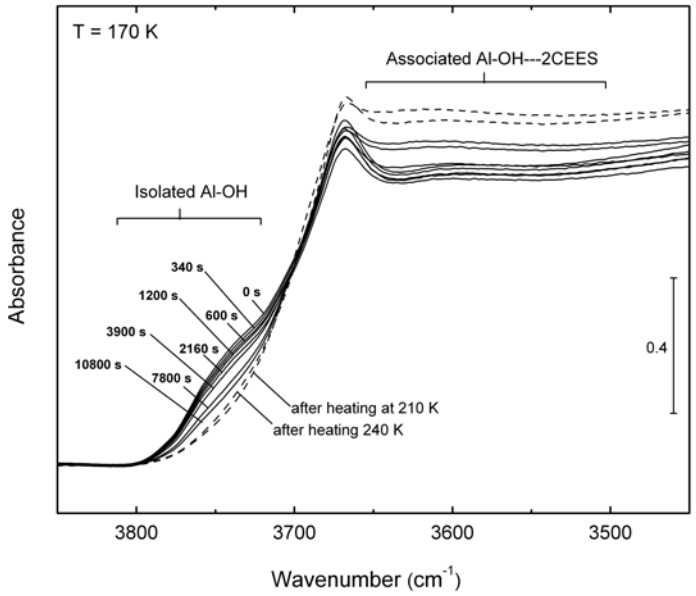

Figure VII-5. FTIR spectra of 2-CEES on the subnano-Al_2O_3 at 170 K with increasing time in the ν(OH) region. The formation of the 2-CEES ice film is carried out at 126 K.

Figure VII-5 shows the spectral behavior of the isolated Al-OH groups for the subnano-Al_2O_3 sample. In this case, the integrated absorbance in the 3800 - 3700 cm^{-1} region due to isolated Al-OH species is approximately the same as in the multinano-Al_2O_3 case compared to subnano-Al_2O_3 case (note vertical scale change from Figure VII-4 to Figure VII-5), and the two Al-OH species observed on the multinano-Al_2O_3 material are not resolved. But in the difference spectra obtained during diffusion (not shown here) one sees clearly that two kinds of Al-OH species are present at ~ 3790 cm^{-1} and ~ 3740 cm^{-1}. Here, too, the normalized absorbance of these two groups decreases as 2-CEES diffusion occurs into the interior. A broad band, centered near 3600 cm^{-1}, is observed to form as 2-CEES hydrogen bonds to the isolated Al-OH groups. Figure VII-5 also shows that the maximized 2-CEES binding to Al-OH is observed at 210 K, followed by partial recovery of the absorbance of isolated Al-OH groups upon heating to 240 K.

VII.4.B Spectroscopic Changes in 2-CEES IR Spectra during Diffusion into Al_2O_3

The IR transmission spectrum through the 2-CEES/Al_2O_3 sample is quite informative about the state of the 2-CEES during the diffusion experiment. When 2-CEES is deposited at 126 K, we observe in the C-H stretching region a total of 7 broad features as seen in Figure VII-6a. The breadth of the IR features is consistent with the presence of an amorphous 2-CEES ice, produced by condensation at the low temperature. Upon heating to 170 K, the spectrum exhibits sharpened bands as seen in Figure VII-6b, and 11 major features become resolved. This is due to the conversion of amorphous ice 2-CEES to a crystalline ice of 2-CEES.[147] We have confirmed this amorphous-to-crystalline ice transformation by observing the same spectral change from amorphous- to ice-2-CEES for a bulk condensed sample of 2-CEES in the absence of Al_2O_3. Finally after extensive diffusion of 2-CEES into the Al_2O_3 at 240 K, and its chemisorption on interior sites, the broadened spectrum, shown in Figure VII-6c is produced.

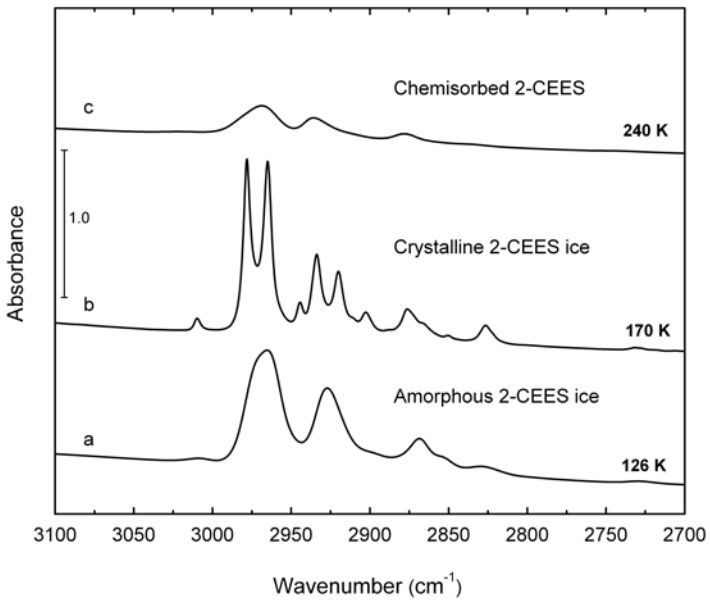

Figure VII-6. FTIR spectra of 2-CEES on multinano-Al_2O_3 in the ν(C-H) region: (a) in the amorphous condensed phase at 126 K; (b) in the crystalline condensed phase at 170 K; (c) in the chemisorbed phase at 240 K.

It is noted that the IR spectrum in the C-H stretching region of the fully-hydrogen bonded adsorbed 2-CEES closely resembles that of the amorphous 2-CEES at 126 K, indicating that crystalline ordering of 2-CEES molecules is responsible for the sharp spectrum (Figure VII-6b) and that the molecular 2-CEES disordering in the amorphous ice and in the adsorbed layer breaks the crystalline order of the ice.

We employ the observation of the ice-2-CEES spectrum to confirm in the isothermal diffusion measurements at 170 K that the crystalline ice 2-CEES layer is present as a source of diffusing 2-CEES *throughout the experiment*. Thus, in Figure VII-7, the C-H region displays the 11 major IR bands indicative of the presence of crystalline ice 2-CEES on the multinano-Al_2O_3 sample; in Figure VII-8, on the subnano-Al_2O_3 sample, we also observe the presence 11 bands indicative of the presence of crystalline ice-2-CEES throughout the entire isothermal diffusion measurements.

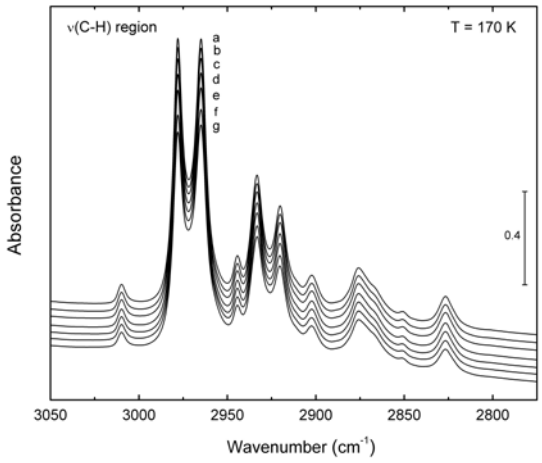

Figure VII-7. FTIR spectra of 2-CEES on multinano-Al_2O_3 in the ν(C-H) region at 170 K with increasing time. Heating time = 390 s, 660 s, 1260 s, 2220 s, 4020 s, 8100 s, and 11400 s, which correspond to the points labeled a to g in Figure VII-3.

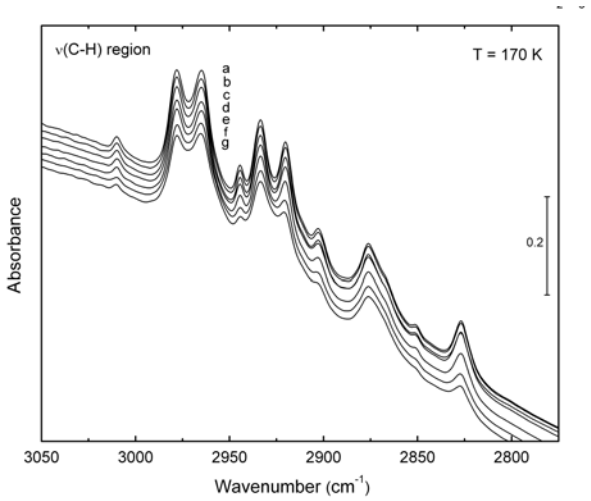

Figure VII-8. FTIR spectra of 2-CEES on subnano-Al_2O_3 in the ν(C-H) region at 170 K with increasing time. Heating time = 340 s, 600 s, 1200 s, 2160 s, 3900 s, 7800 s, and 10800 s, which correspond to the points labeled a to g in Figure VII-3.

VII.5 Discussion

VII.5.A Summary of the Experiments

Experiments similar to that shown in Figure VII-2 have been reported previously for another γ-Al_2O_3 sample.[83,84] The spectral behavior of the Al-OH features in the previous work for 2-CEES diffusion is essentially identical to that observed for multinano-Al_2O_3 shown in this work. The subnano-Al_2O_3 differs in its hydroxyl IR spectrum due to the different morphology and method of preparation of this very high area material. Judging from the integrated absorbance of the isolated Al-OH groups between 3810 cm^{-1} and 3700 cm^{-1}, the two Al_2O_3 materials contain approximately the same number of isolated Al-OH groups per unit mass. It is clear from our diffusion measurements, using Al-OH groups as sensors for the arrival of the 2-CEES molecule, shown in Figures VII-2 and VII-3, that the rate of entry of 2-CEES into the interior of the powdered Al_2O_3 is faster for the subnano-Al_2O_3 than for the multinano-Al_2O_3

material. The Al-OH absorbance change measurements (using Al-OH groups as sensors of 2-CEES arrival and trapping) are indicative of the fractional entry of 2-CEES into the powder interior. In addition to Al-OH groups, other types of adsorption sites (such as Lewis acid sites) may also be active for 2-CEES bonding and trapping.[83,84]

The application of these and other γ-Al_2O_3 preparations for sorption processes will involve other molecules at temperatures above the cryogenic temperatures used here. We have employed such low temperatures to slow down the diffusion process so that it may be conveniently observed in the laboratory, allowing a comparison of molecular diffusion through subnano- and multinano- particle size sorbents

VII.5.B Modeling Diffusion into Al_2O_3 powders

Porous materials are characterized by pore volume, pore size distribution, pore topology, pore morphology, surface area, surface chemistry, properties of the material, etc. These factors, apart from the properties of the adsorbing fluids, determine the adsorption and diffusion properties of fluids into the materials.

The diffusion of 2-CEES into γ-Al_2O_3 causes the formation of a 2-CEES adsorption complex at the isolated hydroxyl groups and at other types of adsorption sites.[83,84] We call all these sites trapping sites (T-sites) in this paper. Such trapping sites play an important role in the diffusion and adsorption process of 2-CEES into γ-Al_2O_3. We consider the effect of T-sites in controlling the surface diffusion,[50] as shown schematically in Figure VII-9. Here T-sites are located distance δ from each other, and the activation energy for diffusion, E_d, is determined at the cross-over point between the T-sites.

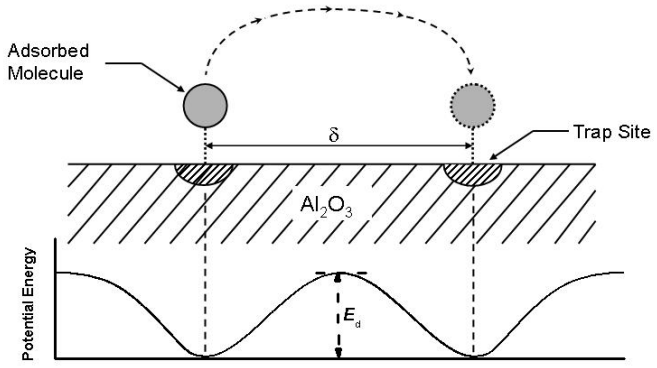

Figure VII-9. Schematic illustration for surface diffusion model.

The diffusivity for surface diffusion has the following form,

$$D_s = \frac{\delta^2}{6\tau} \qquad \text{(VII-1)}$$

where δ = distance between adjacent sites (m), and τ = average time that a site is occupied between jumps (s). τ is given by,

$$\tau = \tau_0 \exp\left(\frac{E_d}{RT}\right) \qquad \text{(VII-2)}$$

where E_d = diffusion activation energy (J mol^{-1}), R = universal gas constant (J mol^{-1} K^{-1}), T = temperature (K), and $\tau_0 = \frac{\delta}{V_T}$ (s), in which V_T is the thermal velocity of the adsorbate molecule (m s^{-1}). Combining equations (VII-1) and (VII-2), we have,

$$D_s = \frac{1}{6} V_T \delta \exp\left(-\frac{E_d}{RT}\right) \qquad \text{(VII-3)}$$

If we assume a uniform distribution of the T-sites, we have,

$$\delta \propto \frac{1}{\sqrt{C_{T-sites}}} \qquad \text{(VII-4)}$$

where, $C_{T\text{-}sites}$ = concentration of the T-sites (mol m^{-2}).

The diffusivity ratio is given by,

$$\frac{D_{s,subnano}}{D_{s,multinano}} = \sqrt{\frac{C_{T-sites,multinano}}{C_{T-sites,subnano}}} \exp\left(-\frac{\left(E_{d,subnano} - E_{d,multinano}\right)}{RT}\right) \qquad \text{(VII-5)}$$

If we assume, for both multinano-Al_2O_3 and subnano-Al_2O_3,

$$\frac{E_a}{E_d} = Q \qquad \text{(VII-6)}$$

where, E_a = desorption activation energy (J mol^{-1}), E_d = diffusion activation energy (J mol^{-1}), and Q = constant. The value of Q depends on the surface roughness, the adsorbate size and the number of bonds made with the substrate. Q is about 2 to 10 for simple molecules on metal surfaces;[57] for 2-CEES diffusion into γ-Al_2O_3, we assume Q = 4 to 8 in our analysis.

We can estimate the diffusion activation energy from the desorption activation energy, E_a. The later can be calculated from the results of thermal desorption experiments.[148,149] For first-order desorption, the Redhead equation is,

$$\frac{E_a}{RT_p} = \ln\left(\frac{\nu_1 T_p}{\beta}\right) - \ln\left(\frac{E_a}{RT_p}\right) \qquad \text{(VII-7)}$$

where β = heating rate (K s^{-1}), ν_1 = reaction rate constant (s^{-1}), E_a = desorption activation energy (J mol^{-1}), and T_p = the temperature at which the desorption rate is a maximum (K).

From the experiments we have normalized the absorbance of isolated Al-OH vs. temperature for 2-CEES diffusion into the γ-alumina (see Figure VII-2). At low temperatures, the adsorption amount increases with an increase of temperature. The isolated Al-OH groups are consumed and associated Al-OH groups are formed in this process. At some higher temperature, T_d, the competition between diffusion into the material and desorption out of the material reaches a balance and the amount of the isolated/associated Al-OH groups reaches a

minimum/maximum. From the experiments, T_d is 240 K and 210 K for multinano-Al_2O_3 and subnano-Al_2O_3, respectively.

To estimate the desorption activation energy, we need T_p, the temperature at which the desorption rate is a maximum. Generally, T_p is smaller than T_d. If we assume that

$$T_{p,multinano} - T_{p,subnano} = T_{d,multinano} - T_{d,subnano} \qquad \text{(VII-8)}$$

and the desorption activation energy is independent of the coverage, we can estimate the desorption activation energy from equation (VII-7) as a function of ν_1. Then we can calculate the diffusion activation energy, E_d, as a function of Q from equation (VII-6). The diffusivity ratio can be obtained from equation (VII-5) if we know the T-site concentrations, $C_{T\text{-}sites}$. We have estimated from the integrated absorbance ratio for the isolated OH group on the two types of Al_2O_3 that,

$$\frac{N_{T-sites,subnano}}{N_{T-sites,multinano}} = \frac{S_{subnano} C_{T-sites,subnano}}{S_{multinano} C_{T-sites,multinano}} \approx 1 \qquad \text{(VII-9)}$$

where, $N_{T\text{-}sites}$ = amount of effective T-sites per gram alumina (mol g^{-1}), S = specific surface area (m^2 g^{-1}), and $C_{T\text{-}sites}$ = concentration of the effective T-sites (mol m^{-2}). So,

$$C_{T-sites,multinano} = \frac{S_{subnano}}{S_{multinano}} C_{T-sites,subnano} \approx 1.3 \cdot C_{T-sites,subnano}$$

The diffusivity ratios for 2-CEES in subnano-Al_2O_3 and multinano-Al_2O_3 are shown in Figure VII-10 for several values of ν_1, ranging from 10^{11} to 10^{15} s^{-1}, and for Q = 4 and 8. These ranges of ν_1 and Q were chosen to represent typical values. For the parameters given above, the diffusion coefficient of 2-CEES in subnano-Al_2O_3 is about 2 to 6 times larger than the diffusion coefficient in multinano-Al_2O_3 at 170 K as shown in Figure VII-10. As seen above, the effect of the chemical binding properties of T-sites as well as surface area and pore volume contributes to the diffusivity into γ-Al_2O_3 sample. Since here the difference of the diffusion activation energy

on two γ-Al_2O_3 powder sample is chosen from the experimental value, T_d, probably it is also affected by the surface morphology property. The comparison of the ν(OH) modes in Figure VII-4 and Figure VII-5 shows that more Lewis acid sites are exposed on multinano-Al_2O_3 than on subnano-Al_2O_3, and these sites are also adsorption sites for 2-CEES.[148,149] This might be another reason for the lower diffusivity on multinano-Al_2O_3.

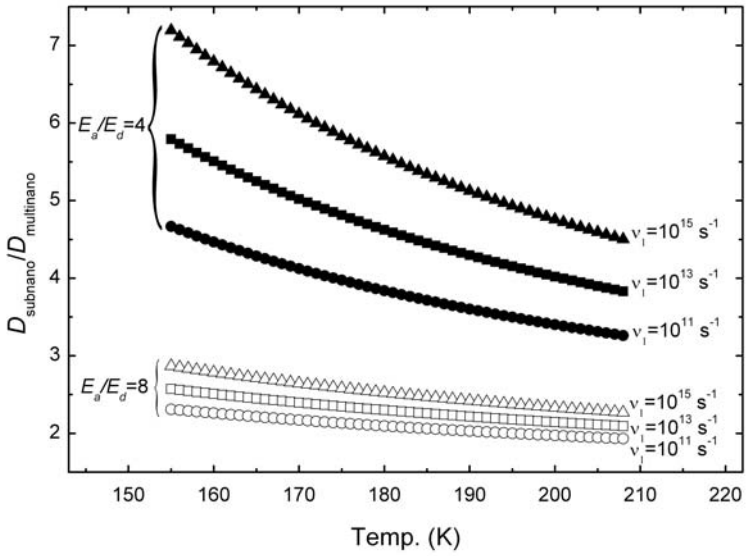

Figure VII-10. Ratio of the diffusion coefficient for 2-CEES on multinano-Al_2O_3 and subnano-Al_2O_3 modeled by the surface diffusion mechanism.

A fit to the data in Figure VII-3 can be made by modeling the data with Fick's Second Law to obtain an independent measure of the ratio of diffusion coefficients for the two γ-Al_2O_3 powders. The ratio of diffusion coefficients computed from a regression fit can be used as a check on the validity of the analysis presented above. Accordingly, we have modeled the diffusion of 2-CEES into the γ-Al_2O_3 membrane of thickness, l, with Fick's Second Law in one dimension,

$$\frac{\partial C(x,t)}{\partial t} = D\frac{\partial^2 C(x,t)}{\partial^2 x} \qquad \text{(VII-10)}$$

with the following boundary and initial conditions,

$$\begin{cases} C(x,t) = C_0, & x = 0, t \geq 0 \\ C(x,t) = C_0, & x = l, t \geq 0 \\ C(x,t) = 0, & 0 < x < l, t = 0 \end{cases} \qquad \text{(VII-11)}$$

The solution to equation (VII-10) is:[22]

$$\frac{C(x,t)}{C_0} = 1 - \frac{4}{\pi}\sum_{n=0}^{\infty}\frac{(-1)^n}{2n+1}\exp\left\{-D(2n+1)^2\pi^2 t/l^2\right\}\cos\frac{(2n+1)\pi x}{l} \qquad \text{(VII-12)}$$

The total amount of 2-CEES which enters the γ-Al_2O_3 at time t is:[150]

$$M_t = \int_0^l C(x,t)dx = M_\infty \times \left(1 - \sum_{n=0}^{\infty}\frac{8}{(2n+1)^2\pi^2}\exp\left\{-D(2n+1)^2\pi^2 t/l^2\right\}\right) \qquad \text{(VII-13)}$$

where, M_∞ = total diffusion amount at infinite time (mol g^{-1}), given by,

$$M_\infty = M_{t\to\infty} \approx \rho V_{pore} \qquad \text{(VII-14)}$$

in which, ρ = density of 2-CEES (mol m^{-3}), and V_{pore} = pore volume of the γ-Al_2O_3 (m^3 g^{-1}).

Experimental results in Figure VII-3 are normalized by the adsorption amount at 210 K and 240 K for subnano-Al_2O_3 and multinano-Al_2O_3, respectively. We assume that at these temperatures 2-CEES forms a monolayer on the internal surface of the γ-Al_2O_3.

To compare with experimental results, equation (VII-13) can be rewritten as:

$$1 - \frac{M_t}{M_N} = 1 - \frac{\rho V_{pore}}{M_N} \times \left(1 - \sum_{n=0}^{\infty}\frac{8}{(2n+1)^2\pi^2}\exp\left\{-D(2n+1)^2\pi^2 t/l^2\right\}\right) \qquad \text{(VII-15)}$$

where, M_N = adsorption amount at 210 K or 240 K for subnano-Al_2O_3 or multinano-Al_2O_3 (mol g^{-1}). In addition,

$$M_N = S/(N_0 A) \qquad \text{(VII-16)}$$

where, A = surface area of one 2-CEES molecule, ($\approx 4 \times 10^{-19}$ m^2) and N_0 = Avogadro's constant.

We have regressed D/l^2 in equation (VII-15) using the experimental data of Figure VII-3 for 2-CEES diffusion into subnano-Al_2O_3 and multinano-Al_2O_3. The normalized amount of adsorbed 2-CEES at 170 K from both regression and experiments are shown in Figure VII-11.

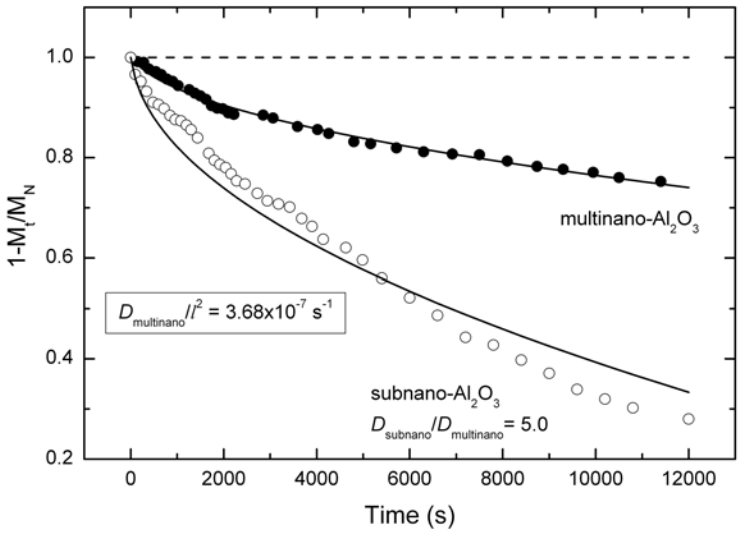

Figure VII-11. Normalized diffusion amount of 2-CEES into multinano-Al_2O_3 and subnano-Al_2O_3 at 170 K. Symbols are experimental results and solid lines are the best fit to the experimental data. $D_{multinano}/l^2$=3.68×10^{-7} s^{-1}. Here l = thickness of the pressed powder sample.

Regressed results fit very well with the experiments for multinano-Al_2O_3 and fairly well with the subnano-Al_2O_3. A ratio of $D_{s,subnano}/D_{s,multinano} \approx 5$ was found from the regressed diffusion coefficients at 170 K. This value is in remarkably good agreement with the range of values computed in the previous analysis.

Since the practical temperature for application of these aluminas for adsorption is near 300 K, it is of interest to calculate the diffusivity ratio at the higher temperature. Using equation (VII-5) and assuming $C_{T-sites,multinano} \approx 1.3 \cdot C_{T-sites,subnano}$ and the observation that $D_{s,subnano}/D_{s,multinano} \approx 5$ at 170 K, we estimate that the ratio $D_{s,subnano}/D_{s,multinano} \approx 2.6$ at 300 K.

VII.6 Summary

The diffusion of the 2-chloroethylethyl sulfide (2-CEES) molecule into two types of γ-Al_2O_3 powders was studied using transmission FTIR spectroscopy, probing the kinetic behavior of isolated Al-OH sites as hydrogen bonding occurs at these trap sites. The temperature dependence and isothermal diffusion experiments show that the diffusion of the 2-CEES molecule into the sub-nanometer crystallite size (< 1 nm) Al_2O_3 powder is more rapid than in the multi-nanometer (2–3 nm) crystallite size Al_2O_3. A surface diffusion model indicates that the diffusion coefficient, D, on the subnano-Al_2O_3 is ~5 times larger than on multinano-Al_2O_3 for the 2-CEES molecule at 170 K.

VII.7 Acknowledgement

We acknowledge with thanks the support of this work by The Army Research Office, and discussion with Dr. Alex Balboa of Aberdeen Proving Ground. We also thank Dr. Olga Koper and Professor Kenneth Klabunde for providing the two well-characterized γ-Al_2O_3 samples studied here.

VIII. Diffusion of CO through Oxide Shells in Pt@CoO Nanoparticles*

VIII.1 Abstract

FTIR spectroscopy has been used to monitor the transport of CO to the Pt cores of Pt@CoO nanoparticles forming CO/Pt species. It was found that external Pt sites are not present on the outer surfaces of the ~ 10 nm diameter nanostructures and that CO transports to Pt adsorption sites by an activated surface diffusion process through the CoO shells surrounding ~ 2 nm diameter Pt cores. The CO transport process is not due to gas phase transport below 300 K. The weakly bound adsorbed CO/CoO species responsible for transport was directly observed at ~ 2147 cm^{-1} during transport through the CoO shells.

---

* Reproduced with permission from S. Kim, Y. Yin, A. P. Alivisatos, G. A. Somorjai, J. T. Yates, Jr. "IR Spectroscopic Observation of Molecular Transport through Pt@CoO Yolk-Shell Nanostructures", Journal of the American Chemical Society, in press, Copyright 2007 American Chemical Society.

VIII.2 Introduction

Recently a Pt@CoO yolk-shell nanostructure, where platinum nanocrystals of several nanometer size are encapsulated in hollow nanostructures of cobalt oxide or cobalt sulfide, was synthesized at the University of California-Berkeley by Yadong Yin *et al*.[64] It was reported that the Pt@CoO yolk-shell exhibits catalytic activity for the ethylene hydrogenation reaction. Since the catalytic activity of platinum is much higher than cobalt or cobalt oxide in this reaction, the reactants and products were postulated to diffuse in and out through the CoO shells to reach the platinum core. This phenomenon was explained by the postulate that small molecules can penetrate through grain boundaries in the polycrystalline CoO shells to reach the internal Pt surface. The observation of the catalytic reaction is not completely definitive for the diffusion process to the interior of Pt@CoO nanostructures, since traces of surface Pt deposited on the outside of the CoO shell or within pores in the CoO shell could also cause ethylene hydrogenation. Electron microscopy indicated that most of the Pt is encased by the CoO shell, but this measurement is not able to definitively detect atomic-size deposits of Pt deposited elsewhere.

An infrared spectroscopic technique, developed previously in the Pittsburgh laboratory for studies of organic molecule diffusion through the pore structure of high area oxide powders, samples surface diffusion over a macroscopic length scale (~ 10^5 nm).[151] We have applied this same technique to monitor the diffusion of the CO molecule through the ~ 5 nm thick shells of CoO, observing the arrival of the CO molecules at the internal Pt surface. The measurements are sufficiently sensitive to detect the weakly-adsorbed CO molecules diffusing over CoO sites, indicating that the CO transport through the CoO shell is via a weakly-bound CO molecule rather than by a gas-phase process through the internal pore structure of the shell. Thus, in this

investigation the infrared spectroscopic method for the direct observation of molecular diffusion through high area material has been extended downward in length scale by ~ 4 orders of magnitude.

VIII.3 Experimental Methods

The experimental methods to measure the molecular diffusion in this work are described in detail in reference.[151] A nanocrystalline powder is pressed into a tungsten grid (0.002″ thickness) using a hydraulic press.[39,40] The grid is tightly stretched and clamped into Ni cooling bars which are bolted onto Cu electrical leads originating from a reentrant Dewar, which serves as a manipulator. A type-K thermocouple is welded to the top of the tungsten grid.[69,70] The temperature as measured by the thermocouple is achieved by resistive heating via the Cu leads using an electronic temperature control program, which heats the sample at a rate of 0.6 Ks^{-1}. The sample temperature can be controlled in the range of 83 K – 1500 K when liquid nitrogen is used as a refrigerant with a resolution of 0.1 K in these experiments.

The manipulator which holds the powdered sample on the grid is movable up and down allowing the measurement of the spectrum of two samples supported one above the other together on the grid. This arrangement allows the properties of CoO shells and Pt@CoO samples to be directly compared under exactly the same experimental conditions.

The synthetic production of these CoO and Pt@CoO nanocrystals is described in reference.[64] After preparation, the average diameter of the outer CoO shell and the inner Pt yolk in the Pt@CoO nanocrystal were confirmed by Transmission Electron Microscopy (TEM) to be 8 – 12 nm and 2 – 3 nm respectively.

Gases are introduced into the IR cell through a gas line in which a Baratron capacitance manometer (0 – 100 Torr) is used for pressure measurement. The base pressure as measured by a

Bayard-Alpert type ionization gauge is ~ 1.0×10^{-8} Torr. To eliminate possible impurity effects from traces of metal carbonyls, the CO storage bulb is immersed in *l*-N_2 when gas is withdrawn.

The infrared spectra are recorded with a Bruker TENSOR 27 FT-IR spectrometer, using a *l*-N_2 cooled MCT detector. Noise levels in the base line of the acquired spectra are in the 3 x 10^{-4} absorbance range. The spectrometer and the enclosed IR cell are purged continuously by dry air from which CO_2 and H_2O have been removed. Each spectrum is obtained by averaging 1024 interferograms at 2 cm^{-1} resolution. The background spectrum taken through the empty grid region is subtracted to eliminate the effect of any gas phase contribution as well as other small effects in the infrared cell.

VIII.4 Results and Discussion

The CoO shells surrounding the Pt cores of the Pt@CoO nanostructures are synthesized from $Co_2(CO)_8$.[64] As shown in Figure VIII-1(a) and Figure VIII-1(c), carbonyl stretching modes are observed in the CoO shells without Pt as well as in Pt@CoO in the as-received material. The mode at 2340 cm^{-1} is assigned as CO_2(a) and may be due to exposure of each sample to the atmosphere. The vibrational feature at ~ 2185 cm^{-1} is assigned as CO bound to Co^{3+} on the CoO shell for both the CoO and Pt@CoO.[152,153]

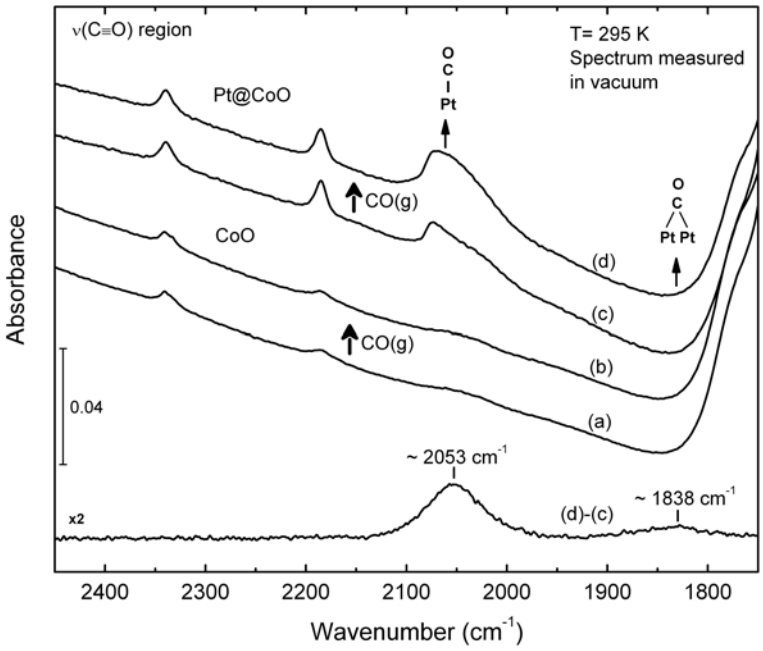

Figure VIII-1. FTIR spectra for CO adsorption (~ 100 Torr) in the ν(C≡O) region at 295 K on CoO: (a) before adsorption, and (b) after adsorption, followed by evacuation, and on Pt@CoO: (c) before adsorption, and (d) after adsorption, followed by evacuation.

We note from the literature that during the decarbonylation of $Co_2(CO)_8$, infrared features in the 2070 cm^{-1} and 2030 cm^{-1} region are observed [154-156] indicating that the CO modes observed in the 2050 cm^{-1} region may be due to subcarbonyl species produced during the decomposition of $Co_2(CO)_8$ at elevated temperature in the nanostructure synthesis. Upon heating to 600 K, the vibrational features in the 2050 cm^{-1} region disappear, and only the 2185 cm^{-1} feature remains for the material as received (not shown here).

Spectra VIII-1(b) and VIII-1(d) are observed after treatment of both samples with CO(g) at 100 Torr and 295 K. By obtaining the difference spectrum (d) – (c), the spectral developments due to CO adsorption on Pt@CoO may be observed as shown in the lower portion of Figure VIII-1. Features at ~ 2053 cm^{-1} and at ~ 1838 cm^{-1} are observed to develop, and these are assigned as the characteristic terminally-bound CO and bridge-bound CO on Pt.[157-159] This experiment therefore shows that at 295 K, CO can transport through the CoO shell to find Pt

adsorption sites on the Pt core of the nanostructure. These spectral features do not develop on the CoO shells which do not contain Pt, as seen in spectra (a) and (b) of Figure VIII-1. It is noteworthy to point out, as will be shown in detail later, that the CO/Pt modes do not develop at 120 K due to the limited mobility of CO through the CoO shell at this low temperature. This observation indicates that Pt sites are not present on the outer surface of the CoO shells in Pt@CoO, since CO adsorption should occur on such sites at 120 K.

Figure VIII-2 shows the temperature dependence of the spectral developments as Pt@CoO is exposed to CO(g) at 2 Torr. Here, the sample under CO(g) is programmed upwards from 110 K at 0.6 Ks^{-1} and cooled back to 110 K for the spectral scan. The subtle changes in the spectra are best seen by difference spectra shown in Figure VIII-3 for Pt@CoO. Here, the temperature dependence of three carbonyl bands at ~ 2147 cm^{-1}, ~ 2050 cm^{-1} and ~ 1836 cm^{-1} may be observed. The latter two bands indicate the chemisorption of CO on the Pt cores of Pt@CoO.[157-159] The 2147 cm^{-1} band is due to a weakly-bound, mobile adsorbed CO species on the CoO sites surrounding the Pt cores. It becomes visible as CO diffusion into the interior of the CoO shells occurs. This assignment is confirmed in Figure VIII-4, where the 2147 cm^{-1} band is the only temperature-dependent feature observed for CoO shells without Pt when exposed to CO(g).

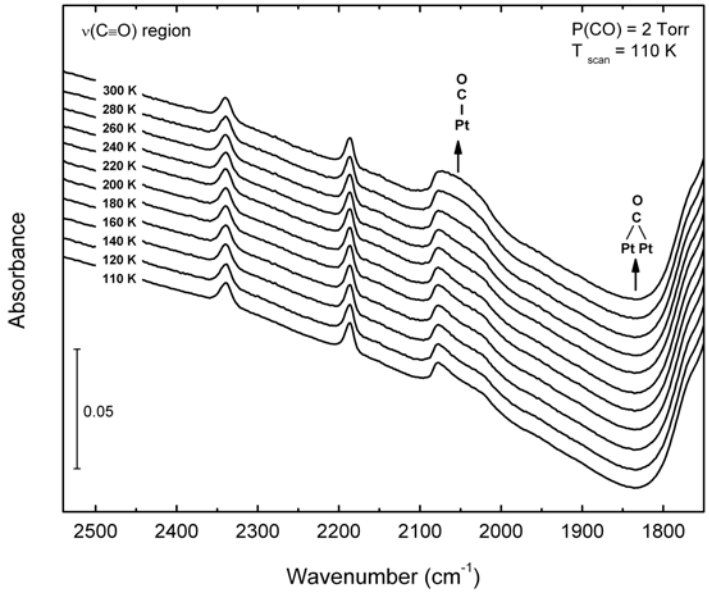

Figure VIII-2. FTIR spectra for CO transport through Pt@CoO at 110 K and after heating the sample (120 K – 300 K). All the spectra were taken at 110 K after cooling the sample, at an equilibrium CO pressure of 2 Torr.

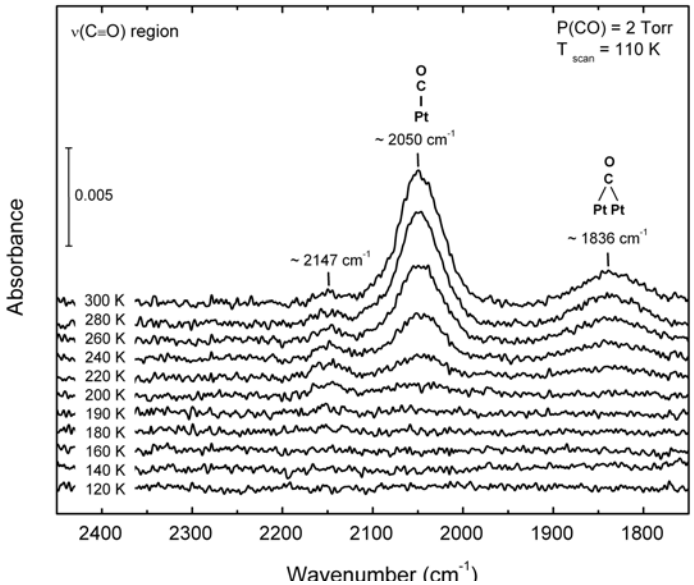

Figure VIII-3. The difference spectra for CO transport through Pt@CoO upon raising sample temperature (120 K – 300 K), which were obtained by subtracting the initial spectrum at 110 K which is shown as the lower spectrum in Figure VIII-2.

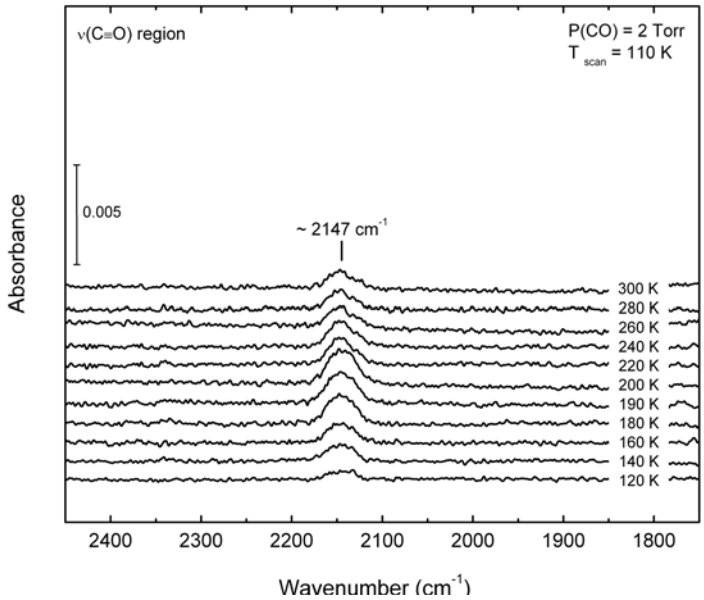

Figure VIII-4. The difference spectra for CO transport through CoO upon raising sample temperature (120 K – 300 K), which were obtained by subtracting the initial spectrum at 110 K.

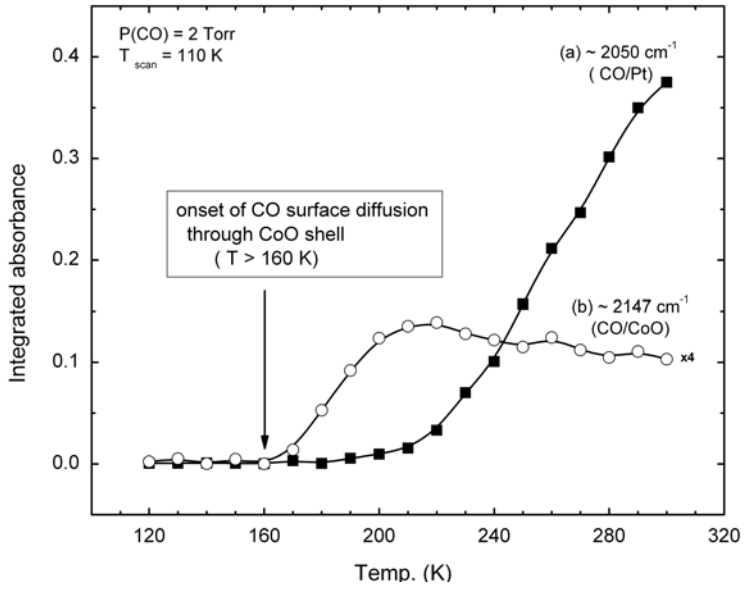

Figure VIII-5. Plot of the integrated absorbance of (a) the terminally-bound CO on Pt at ~ 2050 cm^{-1} and (b) the weakly-bound CO in the CoO shells ~ 2147 cm^{-1} as a function of temperature.

The temperature dependence of the kinetic processes at work in the transport of CO through the CoO shells to the internal Pt cores is shown in Figure VIII-5. At P(CO) = 2 Torr and at about 160 K, the integrated absorbance of adsorbed CO on CoO sites (~ 2147 cm^{-1}) intensifies and maximizes near 215 K. Concomitant with the penetration of adsorbed CO into the CoO shells, Figure VIII-5 shows that the ~ 2050 cm^{-1} band due to CO/Pt begins to intensify slightly also near 160 K, but that the rate of intensification becomes much greater above ~ 215 K, when the CO/CoO band has maximized its intensity. This behavior strongly suggests that weakly-bound CO, adsorbed on CoO sites within the shell structure surrounding the Pt clusters in Pt@CoO, kinetically feeds CO to the encapsulated Pt sites.

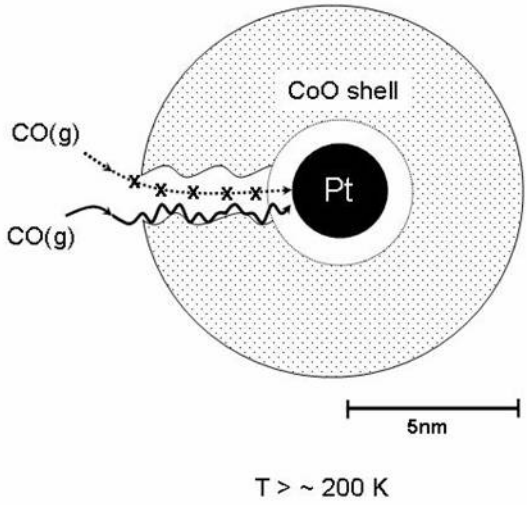

Figure VIII-6. Schematic picture of the CO diffusion through the CoO shells in Pt@CoO.

Figure VIII-6 shows a schematic view of the kinetic processes at work in supplying CO to Pt@CoO nanostructures. We observe the presence of a weakly-bound CO/CoO species (at ~ 2147 cm^{-1}) which are populated prior to arrival of CO molecules at the encapsulated Pt sites; these weakly-bound species mediate the transport of CO into the interior of the Pt@CoO nanoclusters. In Figure VIII-6, we schematically indicate that transport of CO(g) through the

CoO shell walls does not supply CO to the internal Pt sites. The lack of such gas phase transport (Knudsen transport) through the pore structure of the CoO shells is confirmed by the absence of evidence for CO/Pt species when the temperature is below ~ 200 K.

These results have implications in the use of encapsulated metal nanostructures for heterogeneous catalysis. Such nanostructures may well have anti-sintering properties which plague many conventional supported metal catalysts. However, using the Pt@CoO structures as an example, at lower temperatures in such catalysts it may be necessary to consider only adsorbed phases within the shell structure as the transport media for reactants and products moving to and fro to the internal catalytic site. More favorable rate processes involving gas phase transport may be lacking or limited. As the temperature of such nanostructure catalysts is raised, the sticking coefficient for the transporting phases within the pore structure of the shell will decrease and the rate of material transport may then reach that of gas phase transport through the pores.

VIII.5 Summary

The molecular transport of adsorbed CO molecules through the CoO shells in Pt@CoO nanostructures was observed using transmission FTIR spectroscopy, probing the development of characteristic IR modes of the adsorbed CO species on the Pt yolk. In addition, the FTIR observation of weakly-bound CO within the pore structure of the CoO shells indicates that the transport of CO occurs by the surface diffusion of the weakly adsorbed molecule below 300 K. The onset of the CO diffusion through the CoO shells in Pt@CoO occurs at ~ 160 K.

VIII.6 Acknowledgement

We acknowledge with thanks the support of the Department of Energy, Office of Basic Energy Sciences.

LIST OF PUBLICATIONS

1. Sunhee Kim, Oleg Byl, John T. Yates, Jr., *"The Adsorption of Triethylenediamine on Al_2O_3-I: A Vibrational Spectroscopic and Desorption Kinetic Study of Surface Bonding"*, J. Phys. Chem. B. *109* (2005) 3499.

2. Sunhee Kim, Oleg Byl, John T. Yates, Jr., *"The Adsorption of Triethylenediamine on Al_2O_3-II: Hydrogen Bonding to Al-OH Groups"* J. Phys. Chem. B. *109* (2005) 3507.

3. Sunhee Kim, Oleg Byl, John T. Yates, Jr., *"The Adsorption of Triethylenediamine on Al_2O_3-III: Bonding to Lewis Acid Al^{3+} Sites"* J. Phys. Chem. B. *109* (2005) 6331.

4. Sunhee Kim, Dan C. Sorescu, Oleg Byl, John T. Yates, Jr., *"The Perturbation of Adsorbed CO by Amine Derivatives Coadsorbed on the γ-Al_2O_3 Surface - FTIR and First Principles Studies"* J. Phys. Chem. B. *110* (2006) 4742.

5. Sunhee Kim, Oleg Byl, Jin-Chen Liu, J. Karl Johnson, John T. Yates, Jr., *"Spectroscopic Measurement of Diffusion Kinetics Through Subnanometer and Larger Al_2O_3 Particles By a New Method – The Interaction of 2-chloroethylethyl sulfide with γ-Al_2O_3"* J. Phys. Chem. B. *110* (2006) 9204.

6. Sunhee Kim, Dan C. Sorescu, John T. Yates, Jr., "*Infrared Spectroscopic Study of the Adsorption of HCN by γ-Al_2O_3 - Competition with Triethylenediamine for Adsorption Sites"* J. Phys. Chem. C. *111* (2007) 5416.

7. Sunhee Kim, Yadong Yin, A. Paul Alivisatos, Gabor A. Somorjai, John T. Yates, Jr., "*IR Spectroscopic Observation of Molecular Transport through Pt@CoO Yolk-Shell Nanostructures"* J. Am. Chem. Soc., *in press.*

8. Sunhee Kim, Dan C. Sorescu, John T. Yates, Jr., "*Infrared Spectroscopic Study of ClCN Adsorption on Clean and TEDA-precovered γ-Al_2O_3", submitted*.

BIBLIOGRAPHY

(1) Halpern, A. M.; Weiss, K. J. Am. Chem. Soc. ***1968****, 90, 6297.*

(2) Farkas, A.; Mills, G. A.; Erner, W. E.; B., M. J. J. Chem. Eng. Data. ***1959****, 4, 334.*

(3) Marzocchi, M. P.; Sbrana, G.; Zerbi, G. J. Am. Chem. Soc. ***1965****, 87, 1429.*

(4) Quagliano, J. V.; Banerjee, A. K.; Goedken, V. L.; Vallarino, L. M. J. Am. Chem. Soc. ***1970****, 92, 482.*

(5) Farkas, A.; Flynn, K. G. J. Am. Chem. Soc. ***1969****, 82, 642.*

(6) Listemann, M. L.; Savoca, A. C.; Wressell, A. L. J. Cell. Plastics ***1992****, 28, 360.*

(7) Silva, A. L.; Bordado, J. C. Catal. Rev. ***2004****, 46, 31.*

(8) Wren, J. C.; Long, W.; Moore, C. J.; Weaver, K. R. Nuclear Technology ***1999****, 125, 13.*

(9) Cho, W. J.; Chang, S. H. J. Korean Nuclear Soc. ***1984****, 16, 80.*

(10) The Radiochemistry of Nuclear Power Plants with Light Water Reactors Neeb, K.-H., Ed.; Walter de Gruyter: Berlin, New York, 1997.

(11) Chemistry and Physics of Carbon; A Series of Advances Thrower, P. A., Ed.; Marcel Dekker, Inc. : New York, 1965.

(12) Walk, R. D. "The History of Military Mask Filters ".

(13) Howard, J. Guidance for Filtration and Air-Cleaning Systems to Protect Building Environments from Airborne Chemical, Biological, or Radiological Attacks; NIOSH Publications Dissemination, 2003.

(14) Morrison, R. W. "Overview of Current Collective Protection Filtration Technology."

(15) Ecob, C. M.; Chements, A. J.; Flaherty, P.; Griffiths, J. G.; Nacapricha, D.; Taylor, C. G. The Science of the Total Environment ***1993****, 130/131, 419.*

*(16) Baker, J. A.; Poziomek, E. J. Carbon **1974**, 12, 45.*

*(17) Deitz, V. R.; Karwacki, C. J. Carbon **1994**, 32, 703.*

*(18) Deitz, V. R.; Karwacki, C. J. Carbon **1993**, 31, 237.*

*(19) Jonas, L. A. Carbon **1978**, 16, 115.*

*(20) Reucroft, P. J.; Chiou, C. T. Carbon **1977**, 15, 285.*

(21) Activated Carbon Surfaces in Environmental Remediation; Bandosz, T. J., Ed.; Elsevier, Ltd.: Amsterdam, San Diego, London, Oxford, 2006.

*(22) Pickett, J. L.; Naderi, M.; Chinn, M. J.; Brown, D. R. Separation Science and Technology **2002**, 37, 1079.*

*(23) Naderi, M.; Pickett, J. L.; Chinn, M. J.; Brown, D. R. J. Mater. Chem. **2002**, 12, 1086.*

*(24) Iu, K.-K.; Thomas, J. K., 71, 55. J. Photochem. Photobiol. A: Chem. **1993**, 71, 55.*

(25) Alumina Chemicals Science and Technology Handbook; Hart, L. D., Ed.; The American Ceramic Society, Inc.: Westerville, Ohio, 1990.

*(26) Kabalka, G. W.; Pagni, R. M. Tetrahedron **1997**, 53, 7999.*

(27) Applied Industrial Catalysis Leach, B. E., Ed.; Academic Press,: New York, 1984.

*(28) Murphy, C. J.; Jana, N. R. Adv. Mater. **2002**, 14, 80.*

*(29) Sander, M. S.; Prieto, A. L.; Gronsky, R.; Sands, T.; Stacy, A. M. Adv. Mater. **2002**, 19, 665.*

*(30) Joo, J.; Park, K. T.; Kim, B. H.; Kim, M. S.; Lee, S. Y.; Jeong, C. K.; Lee, J. K.; Park, D. H.; Yi, W. K.; Lee, G. H.; Ryn, K. S. Synthetic Metals **2003**, 7-9, 135.*

*(31) Santos, P. S.; Santos, H. S.; Toledo, S. P. Materials Research **2000**, 3, 104.*

*(32) Krokidis, X.; Raybaud, P.; Gobichon, A.-E.; Rebours, B.; Euzen, P.; Toulhoat, H. J. Phys. Chem. B. **2001**, 105, 5121.*

(33) Digne, M.; Sautet, P.; Raybaud, P.; Euzen, P.; Toulhoat, H. J. Catal. ***2002****, 211, 1.*

(34) Digne, M.; Sautet, P.; Raybaud, P.; Euzen, P.; Toulhoat, H. J. Catal. ***2004****, 216, 54.*

(35) John, C. S.; Alma, N. C. M.; Hays, G. R. Appl. Catal. ***1983****, 6, 341.*

(36) Lee, M. H.; Cheng, C. F.; Heine, V.; Klinowski, J. Chem. Phys. Lett. ***1997****, 265, 673.*

(37) Beaufils, J. P.; Barbaux, Y. J. Chim. Phys. ***1981****, 78, 347.*

(38) Nortier, P.; Fourre, P.; Mohammed Saad, A. B.; Saur, O.; Lavalley, J.-C. App. Catal. ***1990****, 61, 141.*

(39) Ballinger, T. H.; Wong, J. C. S.; Yates, J. T., Jr. Langmuir ***1992****, 8, 1676.*

(40) Ballinger, T. H.; Yates, J. T., Jr. Langmuir ***1991****, 7, 3041.*

(41) Knözinger, H.; Ratnasamy, P. Catal. Rev. Sci. Eng. ***1978****, 17, 31.*

(42) Peri, B. J. Phys. Chem. ***1965****, 69, 211.*

(43) Barteau, M. A. J. Vac. Sci. Technol. A, ***1993****, 11, 2162.*

(44) Stair, P. C. J. Am. Chem. Soc. ***1982****, 104, 4044.*

(45) Trueba, M.; Trasatti, S. P. Eur. J. Inorg. Chem. ***2005****, 2005, 3393.*

(46) Griffin, G. L.; Yates, J. T., Jr. J. Chem. Phys. ***1982****, 3751.*

(47) Zecchina, A.; Platero, E. E.; Areán, C. O. J. Catal. ***1987****, 107, 244.*

(48) Zaki, M. I.; Knözinger, H. Spectrochim. Acta ***1987****, 43A, 1455.*

(49) Zaki, M. I.; Knözinger, H. Mater. Chem. Phys. ***1987****, 17, 201.*

(50) Do, D. D. Absorption Analysis: Equilibria and Kinetics Imperial College Press: London, 1998; Vol. 2.

(51) Surfaces of Nanoparticles and Porous Materials Contescu, C. I.; Schwarz, J. A., Eds.; CRC Press: New York, 1999.

(52) Choi, J.-G.; Do, D. D.; Do, H. D. Ind. Eng. Chem. Res. ***2001****, 40, 4005.*

(53) Ruthven, D. M. Principles of Adsorption and Adsorption Processes

John Wiley & Sons, Inc. : New York, 1984.

(54) Crittenden, B.; Thomas, W. J. Adsorption Technology & Design Butterworth Heinemann Boston, 1998.

(55) Knudsen, M. Ann. Phys. (Leipzig) ***1909****, 28, 75.*

(56) DeBoer, J. H. The Dynamical Character of Adsorption Oxford University Press: London, 1968.

(57) Gomer, R. Field Emission and Field Ionization; American Institute of Physics: New York, 1993.

(58) Schneider, P.; Smith, J. M. AIChE J. ***1968****, 14, 886.*

(59) Reed, E. M.; Butt, J. B. J. Phys. Chem.

1971*, 75, 133.*

(60) Costa, E.; Calleja, G.; Domingo, F. AlChE J. ***1985****, 31, 982.*

(61) Skoulidas, A. I.; Sholl, D. S.; Johnson, J. K. J. Phys. Chem. ***2006****, 124, 054708.*

(62) Ash, R.; Barrer, R. M.; Pope, C. G.; . Proceedings of the Royal Society of London Series A. Mathematical and Physical Sciences ***1963****, 271, 1.*

(63) Kirkerndall, E. O.; Smigelskas, A. D. AIME TRANS. ***1947****, 171, 130.*

(64) Yin, Y.; Rioux, R. M.; Endonmez, C. K.; Hughes, S.; Somorjai, G. A.; Alivisatos, A. P. Science ***2004****, 304, 711.*

(65) Buriak, J. M. Science ***2004****, 304, 692.*

(66) Smith, R. Chemical Process Design And Integration John Wiley and Sons, Ltd., 2005.

(67) Poulopoulos, S. G.; Inglezakis, V. J. Adsorption, Ion Exchange and Catalysis: Design of Operations and Environmental Applications Elsevier: Oxford, 2006.

(68) Kanazawa, T. Catalysis Letters ***2006****, 108, 45.*

(69) Basu, P.; Ballinger, T. H.; Yates, J. T., Jr. Rev. Sci. Instrum. ***1988****, 59, 1321.*

(70) Yates, J. T., Jr. Experimental Innovations in Surface Science; Apring-Verlag: New York, 1998.

(71) Hall, C. R.; Sing, K. S. Chem. Br. ***1988****, 24, 670.*

(72) Rossin, J. A.; Morrison, R. W. Carbon ***1991****, 29, 887.*

(73) Cornelius, E. B.; Milliken, T. H.; Mills, G. A.; Oblad, A. G. J. Phys. Chem. ***1955****, 59, 809.*

(74) Peri, J. B.; Hannan, R. B. J. Phys. Chem. ***1960****, 64, 1526.*

(75) Weiss, G. S.; Parkes, A. S.; Nixon, D. R.; Hughes, R. E. J. Chem. Phys. ***1964****, 41, 3759.*

(76) Pimentel, G. C.; McClellan, A. L. The Hydrogen Bond; W. H. Freeman and Company: San Francisco, London, 1960.

(77) Wada, T.; Kishida, E.; Tomhe, Y.; Suga, H.; Seki, S.; Nitta, I. Bull. Chem. Soc. Jpn. ***1960****, 33, 1317.*

(78) Beebe, T. P.; Gelin, P.; Yates, J. T., Jr. Surface Science ***1984****, 148, 526.*

(79) Beebe, T. P.; Yates, J. T., Jr. Surface Science ***1985****, 159, 369.*

(80) Antoniewicz, P. R.; Cavanagh, R. R.; J. T. Yates, Jr. J. Chem. Phys ***1980****, 73, 3456.*

(81) Kim, S.; Byl, O.; Yates, J. T., Jr. J. Phys. Chem. B. ***2005****, 109, 3499.*

(82) Knözinger, H. In Surface Organometallic Chemistry: Molecular Approaches to Surface Catalysis; Kluwer: Boston, 1988.

(83) Mawhinney, D. B.; Rossin, J. A.; Gerhart, K.; Yates, J. T., Jr. Langmuir ***1999****, 15, 4789.*

(84) Mawhinney, D. B.; Rossin, J. A.; Gerhart, K.; Yates, J. T., Jr. Langmuir ***2000****, 16, 2237.*

(85) Jeffrey, G. A. An Introduction to Hydrogen Bonding;; Oxford University Press: New York, Oxford, 1997.

(86) *Jeffrey, G. A.; Mitra, J. J. Am. Chem. Soc.* ***1984****, 106, 5546.*

(87) *Kim, S.; Byl, O.; Yates, J. T., Jr. J. Phys. Chem. B.* ***2005****, 109, 3507.*

(88) *Ballinger, T. H.; Yates, J. T., Jr. J. Phys. Chem,* ***1991****, 95, 1694.*

(89) *Zaki, M. I.; Knozinger, H. J. Phys. Chem,* ***1986****, 90, 3176.*

(90) *Zaki, M. I.; Knozinger, H. J. Catal.* ***1989****, 119, 311.*

(91) *Kim, S.; Byl, O.; Yates, J. T., Jr. J. Phys. Chem. B.* ***2005****, 109, 6331.*

(92) *Frisch, M. J. Gaussian 03, Revision C.02; Gaussian, Inc.: Wallingford CT, 2004.*

(93) *Kresse, G.; Furthmüller, J. Comput. Mat. Sci.* ***1996****, 6, 15.*

(94) *Kresse, G.; Furthmüller, J. Phys. Rev.* ***1996****, B 54, 11169.*

(95) *Kresse, G.; Hafner, J. Phys. Rev.* ***1993****, B 48, 13115.*

(96) *Kresse, G.; Hafner, J. J. Phys. Cond. Matter* ***1994****, 6, 8245.*

(97) *Vanderbilt, D. Phys. Rev.* ***1990****, B 41, 7892.*

(98) *See VASP manual at http://cms.mpi.univie.ac.at/vasp/vasp/vasp.html.*

(99) *Perdew, J. P.; Chevary, J. A.; Vosko, S. H.; Jackson, K. A.; Pedersen, M. R.; Singh, D. J.; Fiolhais, C. Phys. Rev.* ***1992****, B 46, 6671.*

(100) *Monkhorst, H. J.; Pack, J. D. Phys. Rev.* ***1976****, B 13, 5188.*

(101) *Kresse, G.; Hafner, J. Phys. Rev.* ***1993****, B 47, 5988.*

(102) *Murnaghan, F. D. Proc. Natl. Acad. Sci. USA* ***1944****, 30, 244.*

(103) *Wilson, S. J. J. Solid. State Chem.* ***1979****, 30, 247.*

(104) *Ealet, B.; Elyakhlouffi, M. H.; Gillet, E.; Ricci, M. Thin Solid Films* ***1994****, 250, 92.*

(105) *Nortier, P.; Fourre, P.; Mohammed Saad, A. B.; Saur, O.; Lavalley, J. C. Appl. Catal.* ***1990****, 61.*

(106) Huber, K. P.; Herzberg, G. Molecular Spectra and Molecular Structure; VI.Constants of Diatomic Molecules Van Nonstrand: New York, 1979.

(107) Frisch, M. J. e. a. Gaussian 03, Revision C.02; Gaussian, Inc.: Wallingford CT, 2004.

*(108) Hadjiivanov, K.; Lamotte, J.; Lavalley, J.-C. Langmuir **1997**, 13, 3374.*

(109) Vibrational Spectroscopy of Trapped Species; Hallam, H. E., Ed.; Wiley:: London, 1973.

(110) Lide, D. R. Handbook of Chemistry and Physics, 84th ed.; CRC press: Florida, 2003.

(111) Antoniewicz, P. R.; Cavanagh, R. R.; Yates, J. T., Jr. J. Chem. Phys.

***1980**, 73, 3456.*

*(112) Buckingham, A. D. Proc. Roy. Soc. (London) **1958**, A248, 169.*

(113) Tipler, P. A. Physics, 2nd ed.; Worth Publishers: New York, 1982.

*(114) Kozirovski, Y.; Folman, M. Trans. Faraday Soc. **1964**, 60, 1532.*

*(115) Low, M. J. D.; Ramasubramanian, N.; Ramamurthy, P.; Deo, A. V. J. Phys. Chem. **1968**, 72, 2371.*

*(116) Morrow, B. A.; Cody, I. A. J. Chem. Soc. Faraday Trans. I **1975**, 71, 1021.*

*(117) Raskó, J.; Bánsági, T.; Solymosi, F. Phys. Chem. Chem. Phys. **2004**, 4, 3509.*

*(118) Szanyi, J.; Kwak, J. H.; Peden, C. H. F. J. Phys. Chem. B. **2005**, 109, 1481.*

(119) Mancuso, J.; McEachern, R. J. Journal of Molecular Graphics and Modelling

***1997**, 15, 82.*

(120) Hurley, M. M.; Wright, J. B.; Balboa, A.; Lushington, G. H. In IEEE Proceedings of the 2003 User Group Conference 2003; pp 55.

(121) We thank Professor Roger Miller for supplying HCN for our work.

*(122) Kim, S.; Sorescu, D. C.; Byl, O.; Yates, J. T., Jr. J. Phys. Chem. B. **2006**, 110, 4742.*

*(123) Pacansky, J.; Calder, G. V. J. Phys. Chem. **1972**, 76, 454.*

(124) Sexton, B. A.; Avery, N. R. Surf. Sci. ***1983****, 129, 21.*

(125) Raskó, J.; Kiss, J. Appl. Cat. A: General ***2006****, 298, 115.*

(126) Low, M. J. D.; Ramasubramanian, N.; Ramamurthy, P.; Deo, A. V. J. Phys. Chem. ***1968****, 72, 2371.*

(127) Morrow, B. A.; Cody, I. A. J. Chem. Soc. Faraday Trans. I ***1975****, 71, 1021.*

(128) Kozirovski, Y.; Folman, M. Trans. Faraday Soc. ***1964****, 60, 1532.*

(129) Rasko, J.; Bansagi, T.; Solymosi, F. Phys. Chem. Chem. Phys. ***2002****, 4, 3509.*

(130) Szanyi, J.; Kwak, J. H.; Peden, C. H. F. J. Phys. Chem. B ***2005****, 109, 1481.*

(131) Kim, S.; Sorescu, D. C.; Yates, J. T., Jr. J. Phys. Chem. C ***2007****, 111, 5416.*

(132) Bradforth, S. E.; Kim, E. H.; Arnold, D. W.; Neumark, D. M. J. Chem. Phys. ***1993****, 98, 800.*

(133) Handbook of Chemistry and Physics; 84th ed.; Lide, D. R., Ed.; CRC Press: Boca Raton, FL, 2003.

(134) Freitag, W. O.; Nixon, E. R. J. Chem. Phys ***1956****, 24, 109.*

(135) Kameoka, S.; Chafik, T.; Ukisu, Y.; Miyadera, T. Catal. Lett. ***1998****, 55, 211.*

(136) Kytökivi, A.; Lindblad, M. J. Chem. Soc. Faraday Trans. I ***1995****, 91, 941.*

(137) Peri, J. B. J. Phys. Chem, ***1966****, 70, 1482.*

(138) Peri, J. B. J. Phys. Chem, ***1966****, 70, 3168.*

(139) Zhuang, J.; Rusu, C. N.; Yates, J. T., Jr. J. Phys. Chem. B ***1999****, 103, 6957.*

(140) Yang, Y.-C.; Szafraniec, L. L.; Beaudry, W. T.; Davis, F. A. J. O. C., 55, 3664. J. Org. Chem. ***1990****, 55, 3664.*

(141) Yang, Y.-C.; Szafraniec, L. L.; Beaudry, W. T.; Ward, J. R. J. Org. Chem. ***1988****, 53, 3293.*

(142) Wagner, G. W.; Bartram, P. W.; Koper, O.; Klabunde, K. J. J. Phys. Chem. B. ***1999****, 103, 3225.*

(143) Valiullin, R.; Kortunov, P.; Kärger, J.; Timoshenko, V. J. Chem. Phys. ***2004****, 120, 11804.*

(144) Valiullin, R.; Kortunov, P.; Kärger, J.; Timoshenko, V. J. Phys. Chem. B. ***2005****, 109, 5746.*

(145) Basila, M. R.; Kantner, T. R.; Rhee, K. H. J. Phys. Chem. ***1964****, 68, 3197.*

(146) Popova, I.; Yates, J. T., Jr. Langmuir ***1997****, 13, 6169.*

(147) Zawadski, A.; Parsons, S. Acta Cryst. ***2004****, E60, o225.*

(148) Redhead, P. A. Vacuum ***1962****, 12, 203.*

(149) Yates, J. T., Jr Methods of Experimental Physics; Academic press: Orlando, 1985; Vol. 22.

(150) Crank, J. The Mathematics of Diffusion, 2 nd ed.; Oxford University Press: New York, 1980.

(151) Kim, S.; Byl, O.; Liu, J.-C.; Johnson, J. K.; Yates, J. T., Jr. J. Phys. Chem. B. ***2006****, 110, 9204.*

(152) Busca, G.; Guidetti, R.; Lorenzelli, V. J. Chem. Soc. Faraday Trans. I ***1990****, 86, 989.*

(153) Mergler, Y. J.; Aslst, A. v.; Delft, J. v.; Nieuwenhuys, B. E. J. Catal. ***1996****, 161, 310.*

(154) Bor, G. Spectrchim. Acta ***1963****, 19, 1209.*

(155) Kurhinen, M.; Pakkanen, T. A. Langmuir ***1998****, 14, 6907.*

(156) Suvanto, S.; Pakkanen, T. A.; Backman, L. Appl. Catal. A: General ***1999****, 177, 25.*

(157) Eischens, R. P.; Pliskin, W. A. Advan. Catal. ***1958****, 10, 1.*

(158) Garland, C. W.; Lord, R. C.; Troiano, P. F. J. Phys. Chem. ***1965****, 69, 1188.*

(159) Mihut, C.; Descorme, C.; Duprez, D.; Amiridis, M.D. J. Catal. **2002**, 212, 125.